Multiscale numerical study of tempered martensitic grade 91 (P) steel at high shear strain

Antony A. Youssef

Publication date

31-12-2023

Licence

Document Version
1

Citation for this work (HarvardUL)

Multiscale Numerical Study of Tempered Martensitic Grade 91 (P) Steel at High Shear Strain

Antony A. Youssef

Bernal Institute

Faculty of Science and Engineering

School of Engineering

University *of* Limerick

1. Primary Supervisor:

<div align="center">

Prof. Noel P. O'Dowd

School of Engineering

University *of* Limerick

Ireland

</div>

2. Second Supervisor:

<div align="center">

Prof. Seán Leen

Department of Mechanical and Biomedical Engineering

University *of* Galway

Ireland

</div>

Declaration

I herewith declare that I have produced this paper without the prohibited assistance of third parties and without making use of aids other than those specified; notions taken over directly or indirectly from other sources have been identified as such. This thesis has not previously been presented in an identical or similar form to any other Irish or foreign examination board.

The thesis work was conducted from 2021 to 2023 under the supervision of Prof. Noel P. O'Dowd and Prof. Seán Leen, at the University of Limerick. All the experimental work presented in this thesis, unless otherwise specified, is carried out by PhD Student Pavan Sreenivasa Rao, at the Bernal Institute, University of Limerick

Limerick, 2023

Examination Board

Internal Examiner: Dr Peter Tiernan

External Examiner: Dr Richard Barrett

Antony A. Youssef

Signature: Antony Youssef

Date: 21.08.2023

Abstract

Tempered martensitic steel Grade 91 with 9% wt. Cr and 1% wt. Mo (P91) has been developed to have high strength, good corrosion, and creep resistance at high temperatures, as well as good weldability. This alloy is mainly used for power plant components which face harsh operating conditions of stress and temperature.

Early failures have been reported in some P91 components. A multi-length scale study and model of P91 at a high deformation level will help understand the reasons behind these failures as well as create a computational lifetime prediction tool, based on creep damage calculations. A shear specimen has been designed, based on ASTM (B831–05), to achieve uniform shear strains (> 30%) while minimising out-of-plane deformation to allow for microstructure analysis using ex-situ electron backscattering diffraction (EBSD). This study is aimed at developing a multi-length scale finite element model, as shown in Figure 0.1, which can capture the deformation of P91. Here, the macro-scale deformation is modelled using an isotropic hardening J2 (von Mises) plasticity model while a crystal plasticity model is used for modelling the micro-scale deformation.

The FE model is validated at a range of strain levels, up to 30%, through EBSD, digital image correlation (DIC) and force-displacement measurements, carried out as a separate part of the project[1].
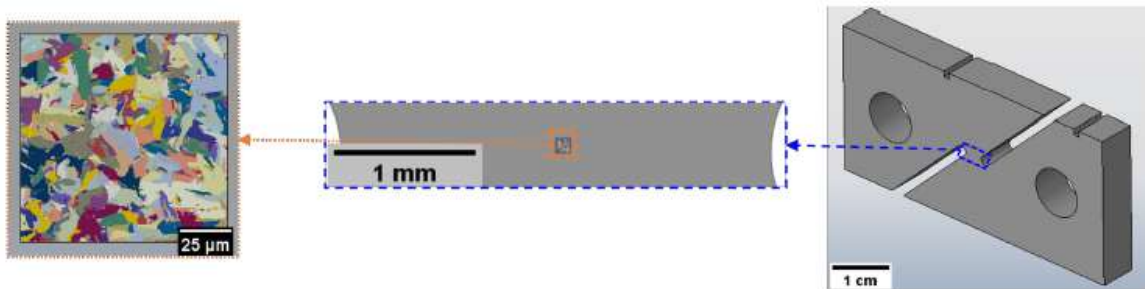
Figure 0.1: Multi-length scale FE model

---

[1] All the experimental work presented in this thesis, unless otherwise specified, is carried out by PhD Student Pavan Sreenivasa Rao, at the Bernal Institute, University of Limerick. This work has been presented at the 11th European Solid Mechanics Conference, Galway, Ireland.

Acknowledgements

Thank you!

Publications and Conferences Associated with this Research.

Pavan Sreenivasa Rao, Antony A. Youssef, Samaneh Isavand, Karthik Ramaswamy, Seán B Leen, Noel P O'Dowd. (2022, July 4-8). A multiscale experimental and numerical study of a martensitic steel at high shear strains [Conference presentation abstract]. The 11th European Solid Mechanics Conference, Galway, Ireland.

Table of contents

Nomenclature

Symbol	Description	Units
L_n	Length between Notches	mm
D_n	Diameter of Notches	mm
γ_t	True shear strain	radians
$\boldsymbol{\varepsilon}^{\mathrm{N}}$	Nominal strain matrix	—
$\boldsymbol{\varepsilon}^{\mathrm{L}}$	logarithmic shear strain matrix	—
$\mathbf{D}^p$	Plastic rate of deformation tensor	s^{-1}
$\mathbf{C_c}$	Crystal Coordinate System	—
$\mathbf{C_s}$	Specimen Coordinate System	—
R	Rotation Matrix	—
$\mathbf{m}^\alpha$	Slip Direction for Slip System ($\boldsymbol{\alpha}$)	—
$\mathbf{n}^\alpha$	Normal on Slip Plane for Slip System ($\boldsymbol{\alpha}$)	—
$\mathbf{F}$	deformation gradient	—
$\mathbf{F}^{\mathrm{e}}$	Elastic deformation gradient	—
$\mathbf{F}^{\mathrm{p}}$	Plastic deformation gradient	—
$\mathbf{S}$	Second Piola-Kirchoff stress	Pa
$\mathbf{E}^{\mathrm{e}}$	Elastic Green Tensor	—
$\mathbf{C}$	The Elastic Moduli	Pa
$\boldsymbol{\sigma}$	Cauchy stress tensor	Pa
S^α	The total slip resistance for the Slip System ($\boldsymbol{\alpha}$)	Pa
τ^α	The resolved shear stress for Slip System ($\boldsymbol{\alpha}$)	
F_o	Helmholtz free energy	J
$\dot{\gamma}_{\mathrm{o}}$	exponential constant in the flow rule	s^{-1}
β_{Lt}	Coefficient of Linear Thermal Expansion	K^{-1}
ν	Poission's Ratio	—
α_{m}	Geometry-Based Stress Concentration Factor	—
D_{ms}	Internal Pipe Diameter	mm
E_{ms}	Wall Thickness	mm
D_{c}	The Creep Damage Fraction	—

Abbreviations

Abbreviation	Description
ASME	American society of mechanical engineers
BCC	Body Centre Cubic
EBSD	Electron backscatter diffraction
FCC	Face Centre Cubic
FE	Finite Element
FGHAZ	Fine-Grained Heat Affected Zone
GUI	Graphical User Interface
HAZ	Heat Affected Zone
ICHAZ	Inter-Critical Heat Affected Zone
IPF	Inverse Pole Figure
LMP	Larson-Miller Parameter
MRFE	Multiresolution Finite Element
SEM	Scanning Electron Microscope
UMAT	User Material Subroutine (in Abaqus)

Chapter 1: Introduction

1.1 Motivation

Enhancing the efficiency of power generation systems will lead to decreasing emissions, and hence, reducing the environmental impact. For coal-fired boilers, an efficiency of 45% can be achieved if the operating pressure reaches 300 bar and the operating temperature is between 600 °C and 650 °C (Ehlers et al., 2006). This is an increase of 12% above the average efficiency of 33% (Office of Fossil Energy and Carbon Management, 2021). For pulverized coal power plants, an increase in the efficiency of 10% (from 37%, subcritical operation to 47% ultra-supercritical range) will reduce CO_2 emissions by 20%, as illustrated in Figure 1.1 (Abson & Rothwell, 2013).
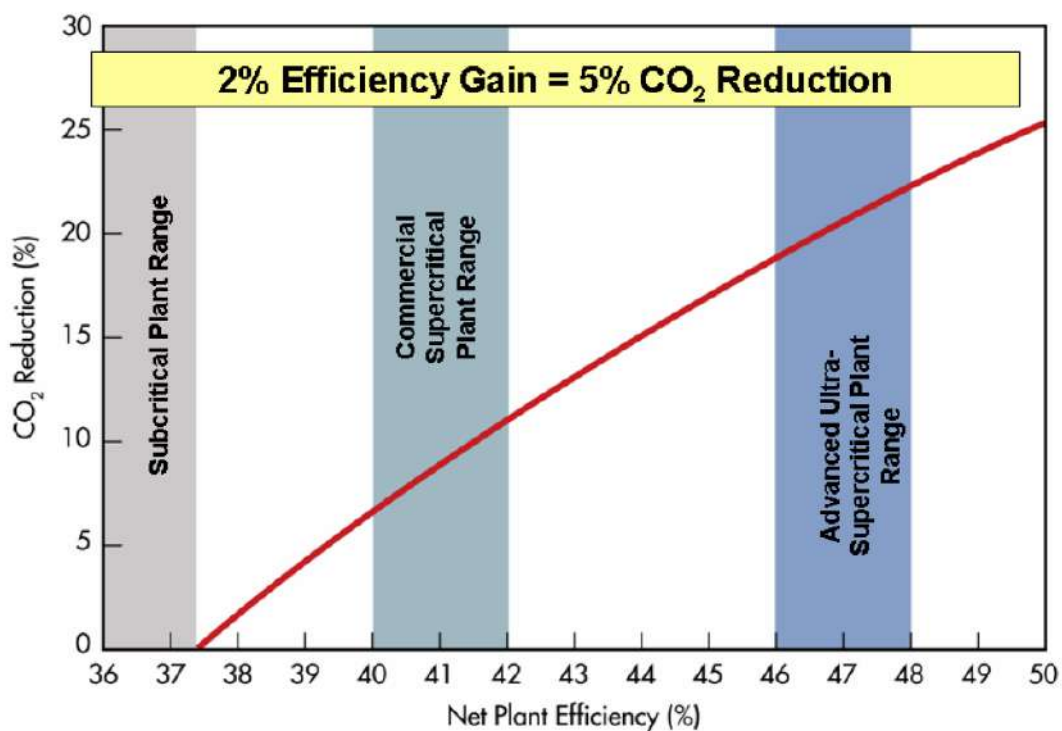
Figure 1.1: Pulverized coal power plant efficiency versus CO_2 emission reduction (Abson & Rothwell, 2013).

Grade 91 (9Cr-1Mo) alloy is a widely used steel alloy for current power generators, especially for steam piping and steam turbine blade materials. It has been developed to replace low alloy, high corrosion resistance steels such as 12% Cr steels, which have inferior creep resistance (Ehlers et al., 2006).

In this project, a shear specimen has been selected and optimized to allow further experimental validation of the finite element model at a significantly higher strain level. This project aims to extend the work of Meade (2020), which developed a finite element model for P91 steel and validated this model experimentally, using tensile and compact tension tests. The multiscale modelling of P91 steel at

high strain represents a crucial step towards accurately modelling and investigating the complex region of the Inter-Critical Heat Affected Zone (ICHAZ) and Fine-Grained Heat Affected Zone (FGHAZ).

1.2 Grade 91 (9Cr-1Mo) Steel

Grade 91 steel was originally developed for the sodium-cooled fast reactor steam generator under a programme initiated in the mid-1970s at Oak Ridge National Laboratory. This process reached its goal by the early 1980s through the modification of 9Cr-1Mo steel with additions of niobium (Nb), vanadium (V) and nitrogen (N). This steel has high creep strength compared to steel alloys in the range of 2.25Cr-1Mo to 12Cr-1Mo (Cabet et al., 2019). Currently, Grade 91 steel is used widely for pressure vessels and piping systems for fossil power plants, where steam temperatures go up to 600 °C. Grade 91 can be used for plate (ASME SA387/SA387M 91), seamless tube (ASME SA213/SA213M T91) and seamless pipe (ASME SA335/SA335M P91). The chemical composition is shown in Table 1.1. The development of 9Cr-1Mo steel over the past 60 years is illustrated in Figure 1.2.

The superior mechanical properties in terms of creep and tensile strength of Grade 91 steel at high temperature, is due to the modification of the steel microstructure. In general, the microstructure of Grade 91 steel is based on balancing the austenite and ferrite stabilisers, to produce 100% austenite at the austenitisation phase, and martensite-dominated microstructure during the normalising process (Song et al., 2019), either by air cooling or by quenching treatment following austenitisation. A small amount of δ-ferrite (<1%) may be present in some cases, especially in the 12%Cr steels (Klueh, 2004). The process to produce this high alloy steel-based martensite ferritic structure is achieved by quenching (rapidly cooling) the steel from the face centre cubic, FCC (austenite) form to the body centre tetragonal, BCT (martensite) dominated form. It is then transformed to the body centre cubic, BCC form (Grade 91 structure), when fully tempered (Cheng et al., 2020; Song et al., 2019). To enhance the toughness of this steel, reheating to an intermediate temperature is performed to decrease the dislocation density formed during quenching in the lath structure (Qadr & Hamad, 2019). The small additives of Nb, V and N lead to precipitate strengthening form fine MX carbonitrides, where M is for niobium or vanadium, and X is for nitrogen, carbon or a combination of both (Abe, 2014). The vanadium carbide contributes to the strengthening of steel, while the niobium carbides restrict grain growth, leading to a refined prior austenite grain size production during austenitization (Qadr & Hamad, 2019). Also, the $M_{23}C_6$ precipitates (M = Cr, Fe, Mo) contribute to the strength and toughness of the steel by retarding the sub-grain growth during the tempering process (Meade et al., 2018a).

Grade 91 steel faces several issues, especially type IV cracking (creep cracking which occurs in the parent material-heat affected zone (HAZ) interface due to creep resistance degradation) and high

corrosion rate in actual power plant conditions (for example, in fossil fuel-fired power plant, oxygen content is on the order of 1 vol%) than the corrosion rate in air (Ehlers et al., 2006). The intercritical fine grain zone in the HAZ formed during welding has lower creep strength compared to the parent material (Das et al., 2008). Grade 91 steel shows high corrosion resistance during operation in the air even at high temperatures. However, under conditions representative of actual power plant conditions, the corrosion rate of 9%Cr steel can be several magnitudes higher than the value in air, due to the oxygen concentration of order 1 vol% and the presence of water vapour of order 7-15 vol% (Ehlers et al., 2006). Corrosion is not examined in this thesis.

To enhance the development of Grade 91 steel, a multi-scale FE model will be developed to simulate seamless pipe material (ASME SA335/SA335M P91) at high strain. Although this work is based on studying parent material, it represents a crucial step towards computationally simulating the complex structure of welds and heat-affected zone (HAZ).

Table 1.1: Chemical Composition of Grade 91 steel (Abe, 2014).

		(Mass %)							
	Grade	C	Mn	P	S	Si	Ni	Cr	Mo
Seamless tube	SA213/SA213M T91	0.07–0.14	0.30–0.60	≤0.02	≤0.01	0.20–0.50	≤0.4	8.0–9.5	0.85–1.05
Seamless pipe	SA335/SA335M P91	0.08–0.12	0.30–0.60	≤0.02	≤0.01	0.20–0.50	≤0.40	8.00–9.50	0.85–1.05
Plate	SA387/SA387M 91	0.08–0.12	0.30–0.60	≤0.02	≤0.01	0.20–0.50	≤0.4	8.00–9.50	0.85–1.05
		0.06–0.15	0.25–0.66	≤0.025	≤0.012	0.18–0.56	≤0.43	7.90–9.60	0.80–1.10

	Grade	V	Nb	N	Al	Ti	Zr	Comments	
Seamless tube	SA213/SA213M T91	0.18–0.25	0.06–0.10	0.030–0.070	≤0.02	≤0.01	≤0.01	Heat/product analysis	
Seamless pipe	SA335/SA335M P91	0.18–0.25	0.06–0.10	0.030–0.070	≤0.02	≤0.01	≤0.01	Heat/product analysis	
Plate	SA387/SA387M 91	0.18–0.25	0.06–0.10	0.030–0.070	≤0.02	≤0.01	≤0.01	Heat analysis	
		0.16–0.27	0.05–0.11	0.025–0.080	≤0.02	≤0.01	≤0.01	Product analysis	

1.3 Aims and Objectives

The main aim of this work is to accurately model the deformation of P91 steel under high strain at multi-scale level and, to develop a computational lifetime prediction tool, based on creep damage calculations, using MATLAB App Designer.

The key objectives to achieve these aims are:

- Develop and optimize a shear specimen design for the scope of this research.
- Perform FE multi-scale simulation of P91 steel and compare with experimental data.
- Create a computational life estimation tool for P91 under operating pressure and temperature, using MATLAB App Designer.

1.4 Thesis Outline

Each chapter of this thesis describes a different aspect of this research, the following is a detailed description of the chapters.
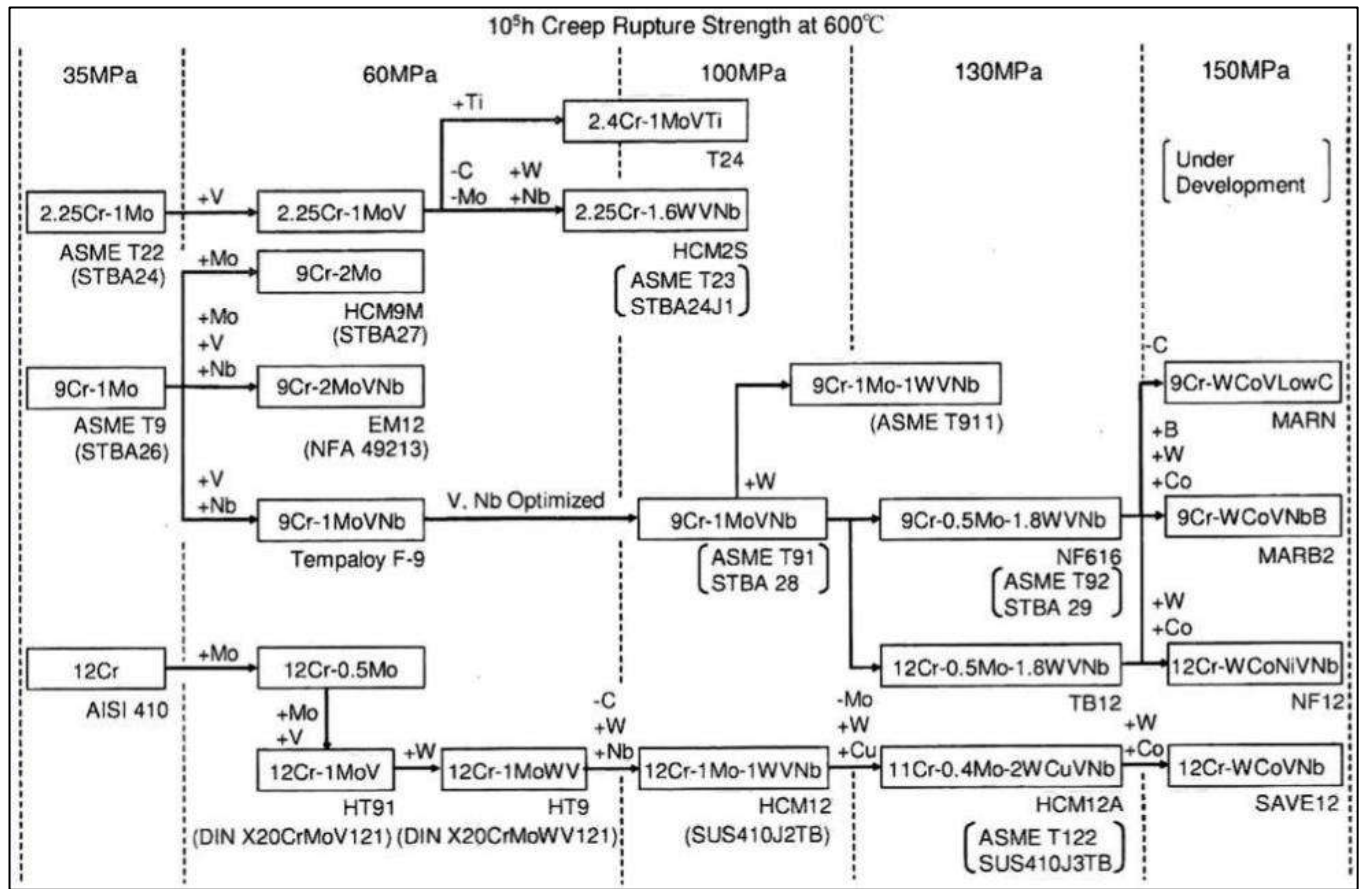
Figure 1.2: Chart illustrating the development of 9–12%Cr steels over past 60 years (Abson & Rothwell, 2013).

Chapter 2: is a literature review for most of the shear specimens which have been developed. This chapter will focus on the shear specimen designs, as developing and optimizing a shear specimen to achieve uniform shear strains (> 30%) while minimising out-of-plane deformation, is the main core of this research. This review describes the aim, design, and objective of every specimen development. The other aspects of this research will be reviewed at the beginning of their chapters.

Chapter 3: discusses the optimization of the shear specimen design. This design is required to fit the experimental setup. In this step, the outer dimensions of the specimen and dimensions of the gauge region are optimized, and the decision regarding the methodology to apply the load on the specimen is confirmed. This optimization process has been validated also via applying it to X100 steel.

Chapter 4: a multi-scale FE simulation of the proposed specimen has been completed and validated against experimental results for P91. The validation has been examined at three levels, the force-displacement level (macroscale), the strain over the gauge region (mesoscale) and the rotation of

a large set of crystals within the gauge region (microscale). The experimental validation has been through results from the Tinius Olsen mechanical test machine, digital image correlation (DIC), and electron backscatter diffraction (EBSD) respectively.

Chapter 5: A life prediction MATLAB app based on calculating the creep damage induced in steam pipes due to pressure has been developed following the approach in Harrison et al., 2016.

Chapter 2: Literature Review: Shear Specimen Selection

2.1 Introduction

This chapter is a review of shear test specimen designs which have been developed to date. This review aims to decide on the shear test design which is most suitable for the scope of this research, which is studying P91 steel at high shear strain. This study requires a shear test design which develops high uniform shear strain at the gauge region, low out-of-plane deformation, and unlikely occurrence of premature fractures at the end of the shear test. The importance of the shear test arises from the fact that this test could be used to validate the material deformation at high strain without the material reaching the failure phase.

2.2 Shear Test Designs

Numerous specimen designs are available for shear testing (Tarnopol'skii & Kintsis, 1981). Various techniques have been developed due to the features which accompany the pure shear test, which is the case of hydrostatic stress is zero and shear stress is dominant (Stojcevski et al., 2018; Tarnopol'skii & Kintsis, 1981).

Among the most popular pure shear techniques are the two-rail V-notch/Arcan test, the three-rail double shear, the double notch shear test, the Iosipescu shear test, the in-plane shear test, and the in-plane torsion test. The two-rail shear test is a modified Arcan test (Liu et al., 1997), with a V-notch geometry of 90° or 102.7°. The Arcan test has also been modified for combined loading cases (Taheri-Behrooz & Moghaddam, 2018, Ud Din et al., 2020). The three-rail double shear test eliminates the rotation of the shear zone in comparison with the two-rail technique (Yin et al., 2014b). In the two rail/Arcan test, two support rods can be used to eliminate the shear zone rotation. However, this specimen requires a large specimen size (Tarnopol'skii & Kintsis, 1981). The double-notch shear test uses the same instrumentation as used in the standard uniaxial tensile test. This specimen has two rectangular notches opposite each other near the centre of the specimen and compression is applied on the edges of the specimen while applying supports to prevent buckling and out-of-plane deformation (Dadras & McDowell, 1990, Shokrieh & Lessard, 1998). The Iosipescu specimen has two V-notches opposite each other at the centre, the specimen is placed in an instrument with a stationary base and a moveable arm to apply a pressure force to the specimen. Variations of the Iosipescu test are the Wyoming shear test, the Idaho shear test and Forest Products Laboratory (FPL) shear test which introduce two guide rods to constrain the fixture to move along the rods to prevent out-of-plane movement (Liu, 2000). The in-plane shear test also leads to rotation of the specimen, which can be solved using stiff clamping tools (Yin et al., 2014b). Several configurations for this test can be found in

(Gao et al., 2011; Peirs et al., 2012a; Reyes & Eriksson, 2009; Tarigopula et al., 2008; Yoshihara & Matsumoto, 2005). The twin bridge specimen, which is used in the in-plane torsion test, is composed of two concentric circular disks that are connected by symmetric shear bridges to prevent any unwanted moment. The load is applied as a moment on the two circular disks, where the strain is localized in the bridges between them (Gardner, 2013, Yin et al., 2012). This specimen in its current design is modified from the classical in-plane torsion test and the grooved in-plane torsion test (Tekkaya et al., 1982; Yin et al., 2015).

2.2.1 Two Rail V-Notch/ Arcan Test

The Two Rail specimen is a modified Arcan Test (Liu et al., 1997). As seen in Figure 2.1, the specimen is characterized by the V-notch geometry. The angle of the notches are V-notches of 90° or 102.7° (see Figure 2.2). A modified test is available to prevent horizontal motion (Figure 2.3). Also, an Arcan test can be used for combined loading cases (Figure 2.4), which combines normal and shear stress states; it also can be used for pure shear cases (Taheri-Behrooz & Moghaddam, 2018b; Ud Din et al., 2020b).

(a)   (b)
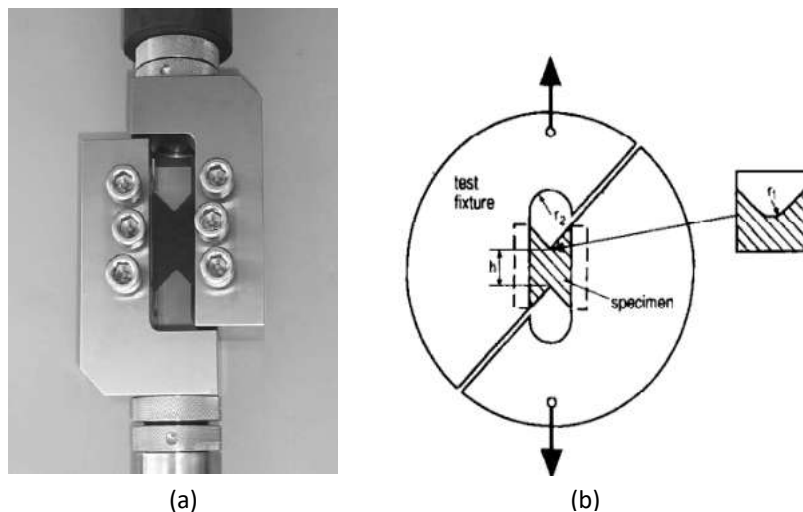
Figure 2.1: (a) The two-rail design and (b) Detail of the two-rail design (D. O. Adams et al., 2007; Turner & Burr, 1993).

2.2.2 Three Rail Double Shear Test

The three-rail double shear test (Figure 2.5), eliminates the rotation of the shear zone in comparison with the two-rail technique (Yin et al., 2014b). The three rails double shear test is recommended for studying the behaviour of thin sheet metals under large strains with high strain rates. The specimen has been optimised for dynamic loading to ensure the development of a pure shear state with uniform shear stress along the shear zone, as well as to avoid buckling and can be used to determine the viscoplastic behaviour of sheet metals (Hußnätter & Merklein, 2008; Rusinek & Klepaczko, 2001).

Figure 2.2: (a) The butterfly design for the Arcan test which is a modification of design (b) (El-Hajjar & Haj-Ali, 2004; Ud Din et al., 2020a).
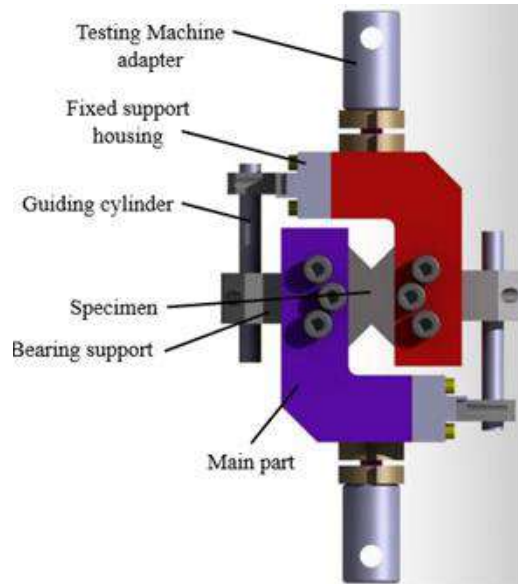
Figure 2.3: The modified V-notched rail shear test to prevent horizontal motion (Stamopoulos et al., 2020).

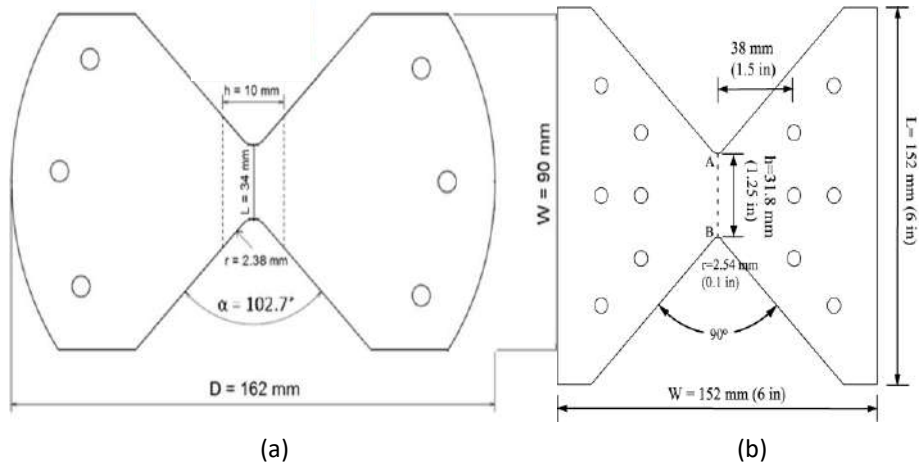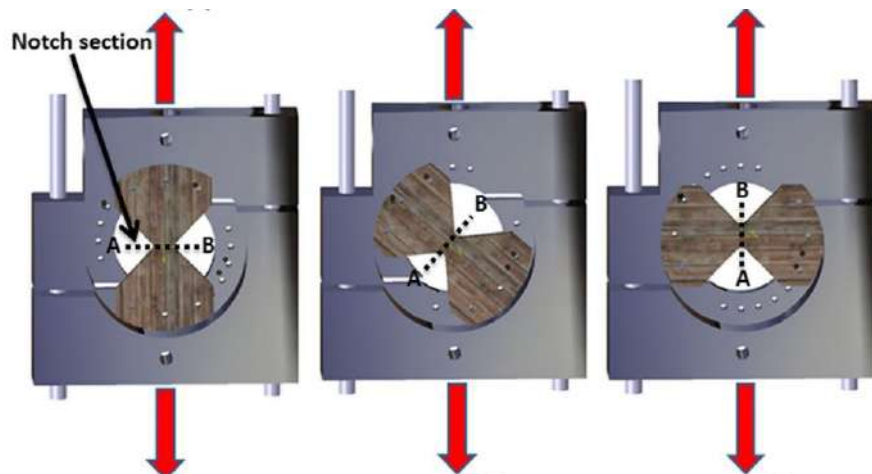**Figure 2.4:** The modification of the Arcan test to account for combined loading cases (Ud Din et al., 2020a).
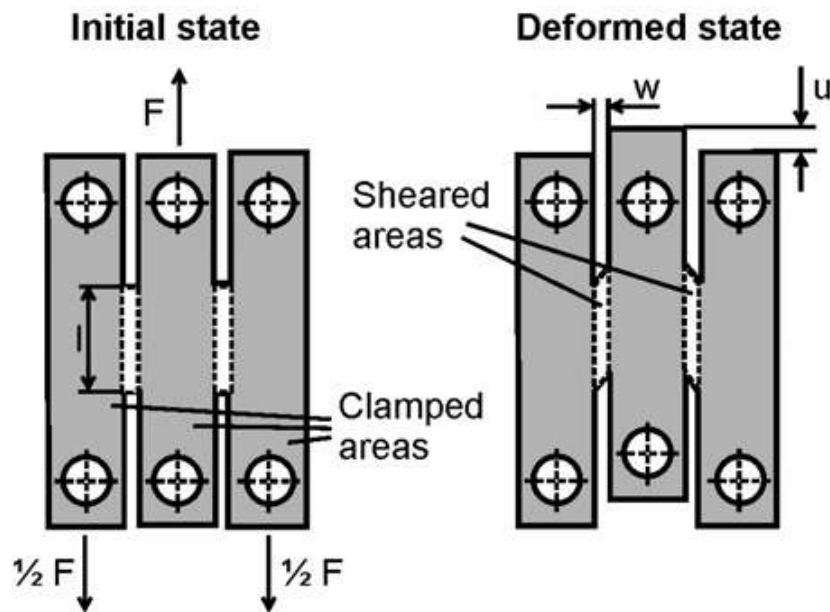
Figure 2.5: The three-rail double shear test (Hußnätter & Merklein, 2008).

2.2.3 Double Notch Shear Test

The double notch shear test (Figure 2.6), comprises two rectangular notches opposing each other. A tension load is applied to the edges of the specimen while applying supports to prevent buckling/out-of-plane deformation in the case of a compression load (Shokrieh & Lessard, 1998). Although the buckling problem has been solved using clamps, as shown in Figure 2.7; however, this may induce errors during dynamic experiments. Besides, the rectangular notches could lead to cracking issues at these edges rather than in the centre of the specimen (Peirs et al., 2012a). An optimization of this technique using eccentric circular notches has been developed to perform uniform shear stress within the shear zone while solving the buckling and cracking problems (Gardner, 2013).
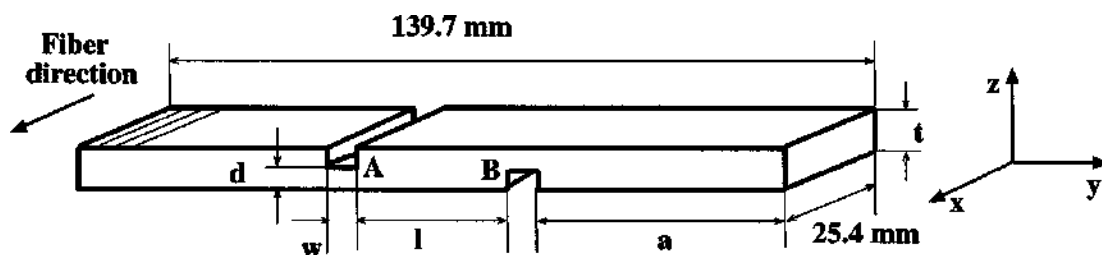
Figure 2.6: The Double Notch Shear Test (Shokrieh & Lessard, 1998).
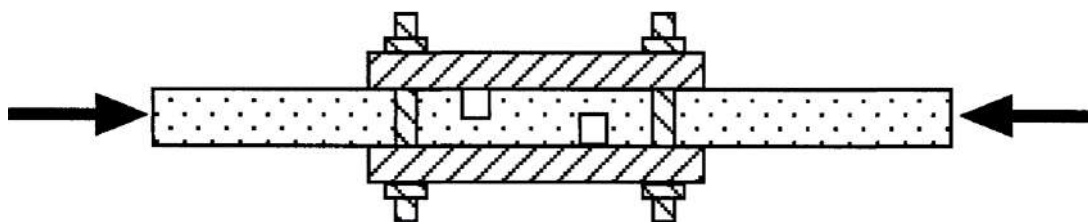
Figure 2.7: The Clamped Double Notch Shear Test to solve the buckling problem (Shokrieh & Lessard, 1998).

9

2.2.4   In-Plane Shear Test

The in-plane shear test, Figure 2.8, depends mainly on the shape of the notches. Rotation of the specimen is minimised by using stiff clamping tools. Several configurations for this test can be found in (Gao et al., 2011; Peirs et al., 2012b; Reyes & Eriksson, 2009; Yoshihara & Matsumoto, 2005). Although this technique is similar to the double notch specimen, it avoids cracking as the notches have round eccentric shapes (Gardner, 2013). Besides, this technique represents an advantage to studying the shear properties of anisotropic materials as the shear is along only one shear zone in comparison with the double shear test. However, specimen rotation could create premature failure in the material. So, this test should be carried out with precautions, to prevent the out-of-plane displacement for a very stiff tool which is indispensable to prevent specimen rotation.
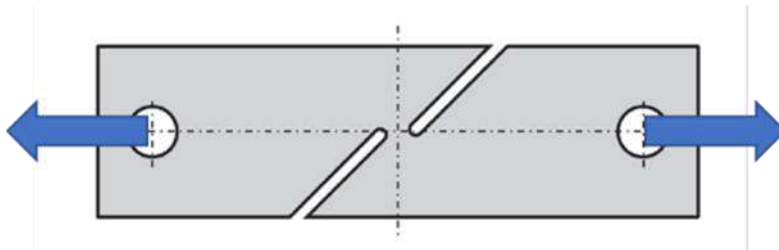
Figure 2.8: The In-Plane Shear Test according to ASTM B831–05 standard (Yin et al., 2014b).
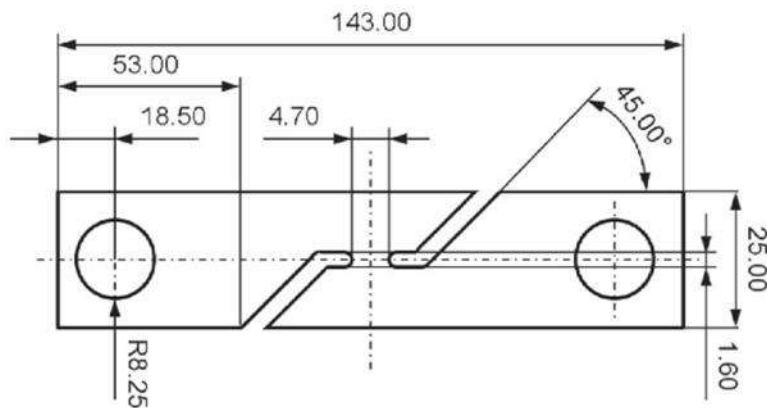
Figure 2.9: The In-Plane Shear Test modified from the ASTM B831–05 standard for applying cyclic loading (Yin et al., 2014b)

This test has been modified as in Figure 2.9 to allow for reversing the load as in cyclic loading (Yin et al., 2014b). Several alternative shapes and designs have been introduced e.g. in Bao & Wierzbicki, 2004, Figure 2.10, for pure shear and combined loading. These designs are appropriate for static loading but are not reliable for high strain rates as their dimensions are too large. That issue has been solved in the design of (Peirs et al., 2012), as illustrated in Figure 2.11. This specimen design minimises the effects of

mechanical waves propagated during the dynamic test (Peirs et al., 2012a). Also, a design was proposed by (Gao et al., 2011) for studying ductile fracture as shown in Figure 2.12.

Figure 2.10: The In-Plane shear test : (a) pure shear, and (b) combined shear/tension (Bao & Wierzbicki, 2004).

Figure 2.11: (a) The in-plane shear test as proposed by Peirs et al.(2012), (dimensions in mm) (b) specimen loaded using a Hopkinson bar (b) (Gardner, 2013).

Figure 2.12: The In-Plane Shear Test as proposed by (Gao et al., 2011), for studying ductile fracture.

2.2.5 Iosipescu Test

The Iosipescu test has two V-notches opposing each other at the centre and it is placed in an instrument with a stationary base and moveable arm to place a pressure force on the specimen as shown in Figure 2.14. The Iosipescu specimen is developed from the asymmetric four-point test, as shown in Figure

11

2.13. This specimen has faced several modifications as shown in Figure 2.14. The Wyoming shear test has been developed to the Idaho shear test through adding additional guide rods, which has been developed to the FPL test by including controlling blocks to prevent any twist or misalignment, which are particularly useful for studying orthotropic materials (Liu, 2000). The Iosipescu test has been primarily used for studying fibre-reinforced polymer composites (D. F. Adams & Walrath, 1987; Stojcevski et al., 2018).
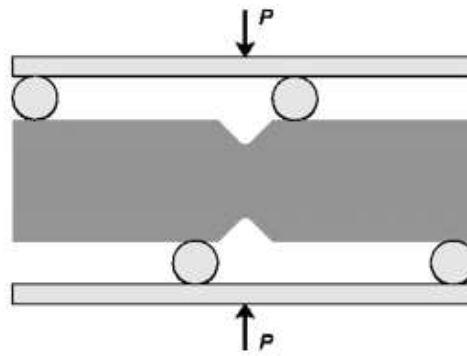
Figure 2.13: The Asymmetric Four-Point Bending (Melin, 2008).
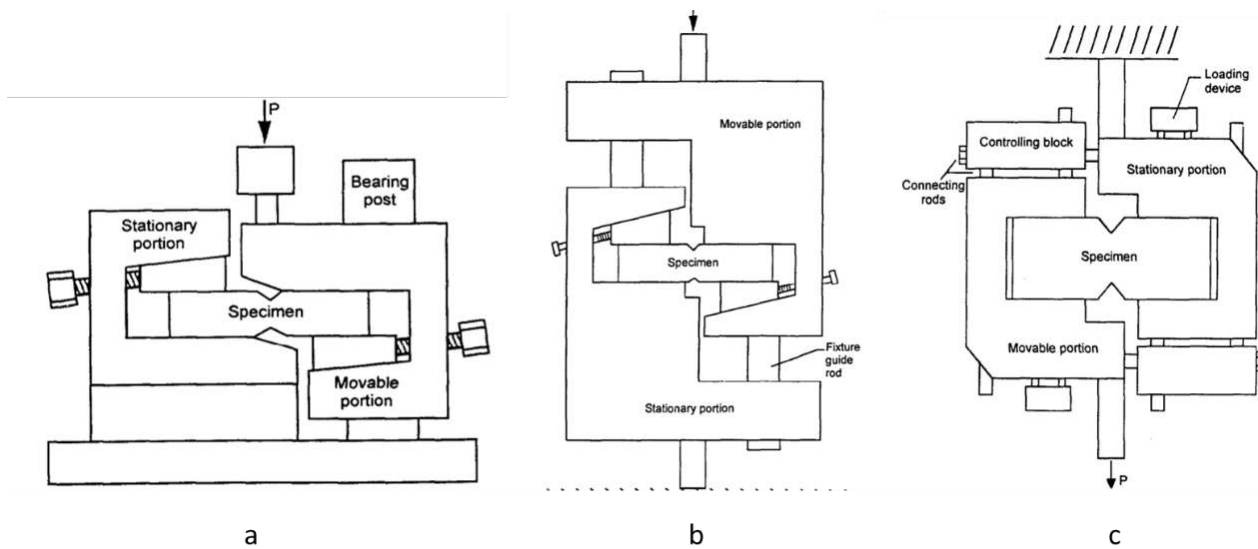
Figure 2.14: The Iosipescu test: (a) The Wyoming version, (b) the Idaho Version, and (c) the FPL Test (Liu, 2000).

2.2.6 In-Plane Torsion Test

The twin bridge specimen, which is used in the in-plane torsion test is composed of two concentric circular disks connected by symmetric shear bridges to prevent any unwanted moment. The load is applied as a moment on the two circular disks where the strain is localized in the bridges between them, as shown in Figure 2.15(a). This design is the result of several modifications of the classic in-plane torsion test, as shown in Figure 2.15(b), and Figure 2.15 (c). The twin bridge specimen could be designed for any number of shear bridges. However, the use of only two shear bridges allows anisotropic material behaviour to be studied without any averaging effects (Gardner, 2013).
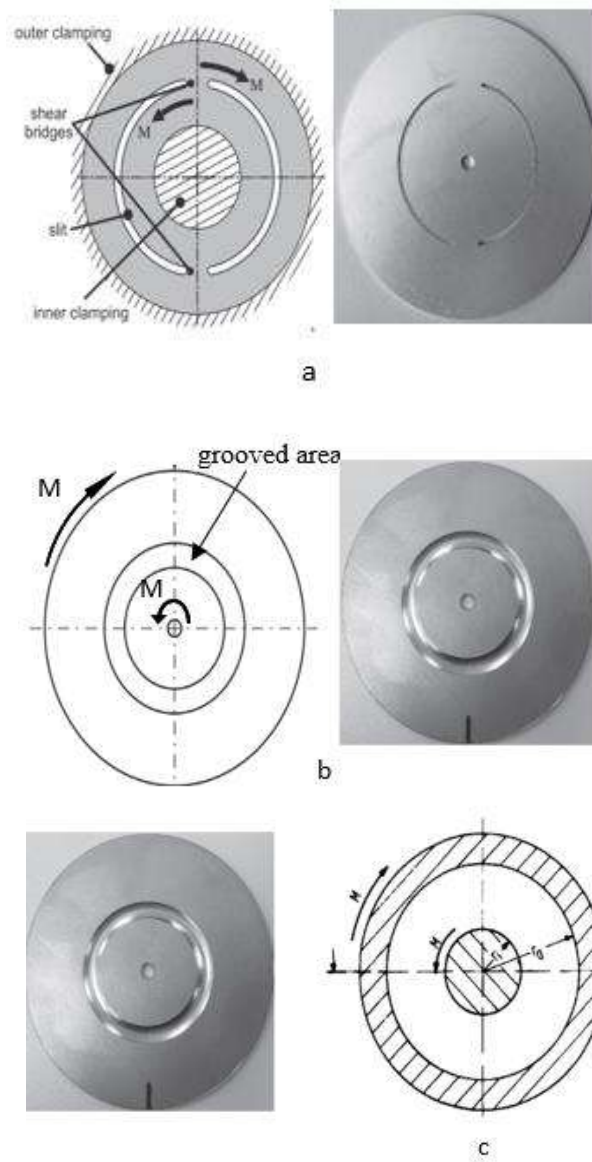
Figure 2.15: The In-Plane Torsion test: (a) Twin Bridge specimen (Yin et al., 2012, 2014a), (b) The grooved-In Plane torsion test (Yin et al., 2015), and (c) The classical in-plane torsion test (Tekkaya et al., 1982).

In this context, although the grooved specimen could prevent any incipient fracture, which could happen along the bridges for the twin bridge specimen, it is not suitable for studying material anisotropy as the measured torque will be an averaged value for the full circumference of the specimen and it is not suitable for studying shear fracture for high toughness steels. Also, machining of the groove is a very challenging process (Yin et al., 2015). Besides, one of the major drawbacks of the twin bridge specimen is the large zone of plastic deformation, which could be solved by mechanically weakening the bridges relative to the specimen to localize the plastic flow (Yin et al., 2012).

2.3   Conclusion

In this chapter, existing shear test designs have been reviewed, and a detailed description of the design of the shear specimens, the shear instruments, and the loading scheme has been provided. Based on this review, it has been decided that the in-plane shear test (Section 2.2.4) is the best fit for the scope of this research for several reasons:

a) The availability and simplicity of the test as it uses a standard tensile test instrument.

b) The suitability for high-strength materials.

c) The insignificant out-of-plane deformation as the shear strain is dominant in the gauge region.

d) The unlikelihood of premature failures as the stress will be delivered from the loading edges to the gauge region through rounded notches.

e) The applicability of specimen optimisation to achieve uniform shear strain at the gauge region.

f) The suitability of the test for static testing.

The standard ASTM shear test specimen (Figure 2.8) and the shear test specimen (Figure 2.11) are the best fit for the scope of this research. However, the standard ASTM test geometry has been selected as it has simple circular notches compared to the shear test specimen (Figure 2.11). This facilitates the manufacturing process.

The next chapter will be concerned with the specimen development and optimisation process. This process will focus on achieving several goals:

a) Optimise the gauge width and the radius of the circular notches to achieve local and uniform shear strain at the gauge region.

b) Ensure that the specimen fits the experimental setup.

c) Determine the diameter of the pins, which are used to apply the load at the edges of the specimen.

Chapter 3: Shear Specimen Design

3.1 Introduction

This chapter represents the design of a shear specimen for studying the deformation of steel Grade 91 (P) through studying and optimizing the shear specimen design proposed in ASTM B831–05 (Standard Test Method for Shear Testing of Aluminum Alloys), see Figure 3.1.
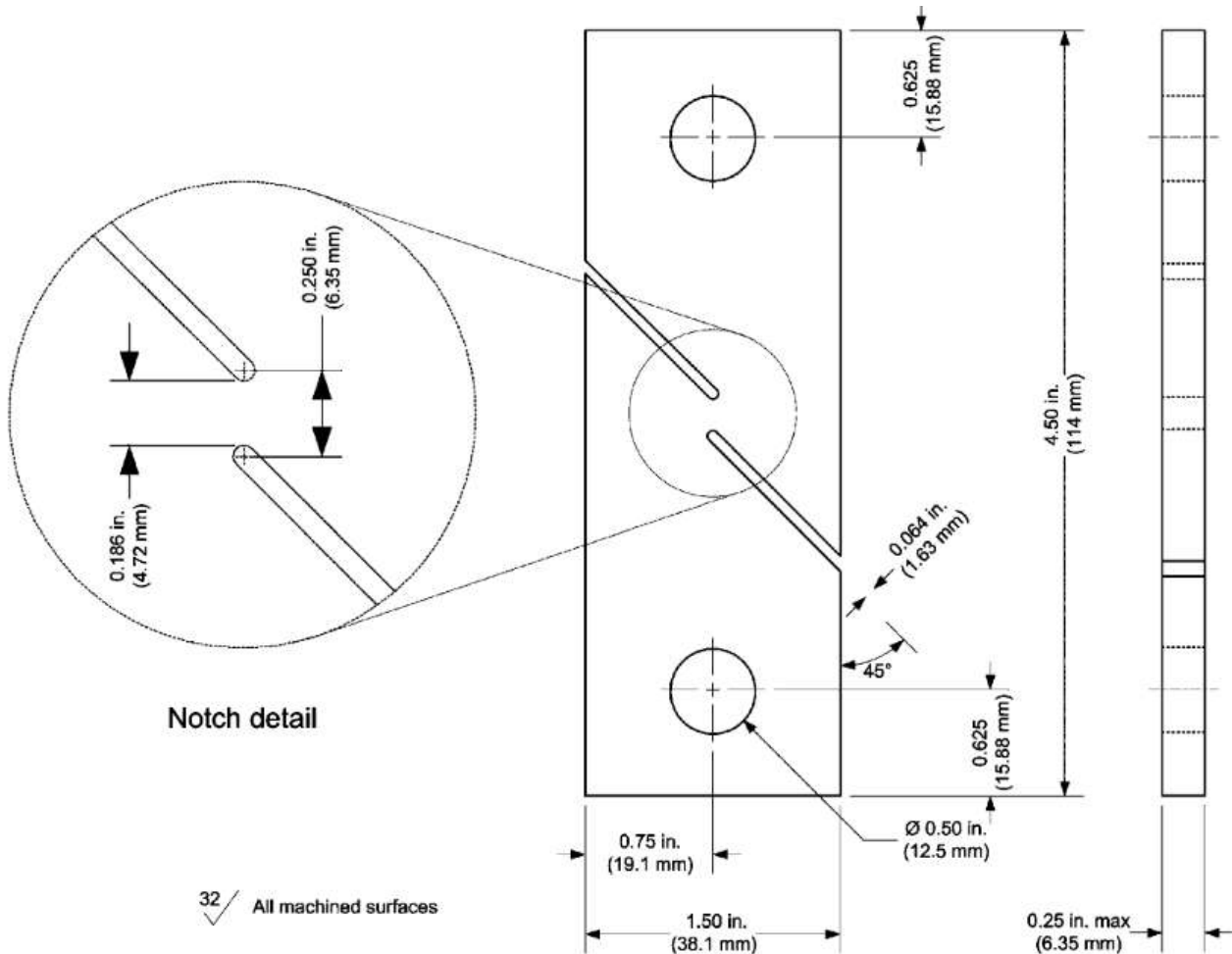
Figure 3.1: Specimen Design in ASTM B831-05, Standard Test Method for Shear Testing of Aluminium Alloys.

The design proposed in ASTM B831-05 has been modified to be suitable for the high shear strain study on Grade 91 (P) steel and has been tested also on X100 steel (a high alloy bainitic steel) as a further validation step. This design process has two main steps: global modification, and local modification at the notch (gauge) region. A finite element (FE) model based on isotropic von Mises plasticity in Abaqus has been used to carry out this design process. A detailed mesh sensitivity analysis will be presented at the end of this chapter, to ensure that the mesh density (sensitivity) has an insignificant effect on the proposed design. The true stress-strain curve for both steel alloys P91 and X100, obtained from tensile tests at room temperature (Meade et al., 2020b; Devaney, 2020), which

have been used to carry out this study, are presented in Figure 3.2. These data have been used for the isotropic von Mises plasticity FE model, which has been created in Abaqus.
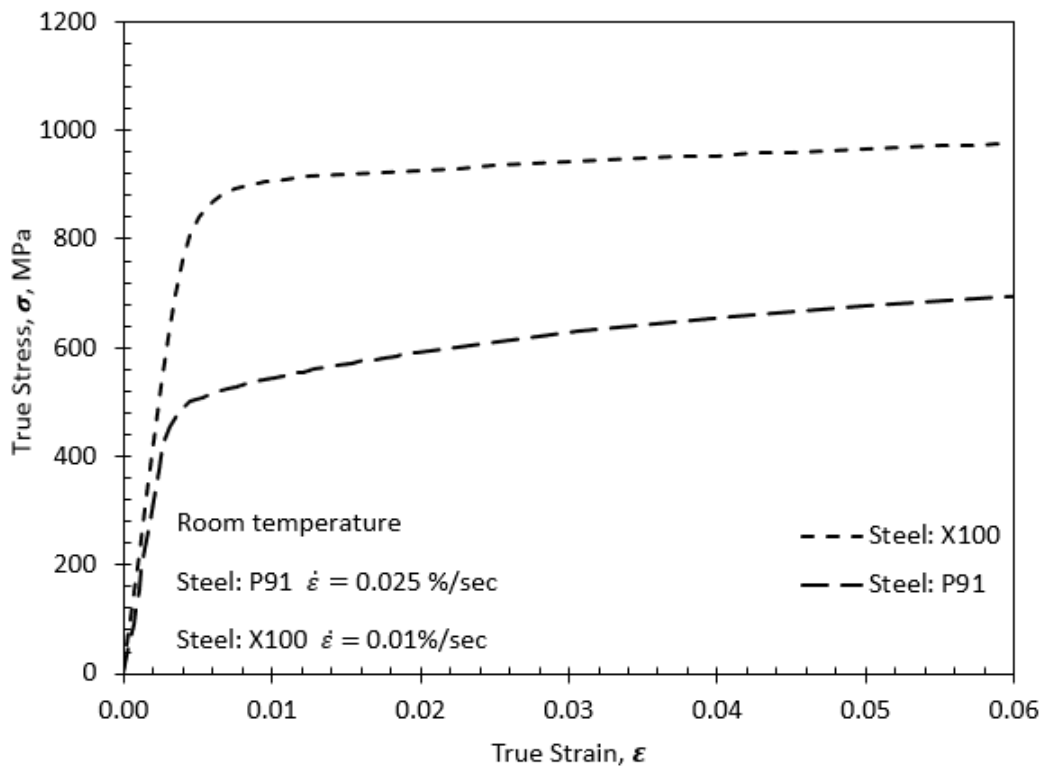
Figure 3.2: Stress-strain data for P91 and X100 from tensile tests at room temperature (Meade et al., 2020b; Devaney, 2020).

3.2 Modifying Shear Specimen's Global Dimensions

The modification of the global dimensions has been carried out to satisfy the following requirements:

a) The suitability for electron backscatter diffraction (EBSD) measurements, the specimen length should be less than 100 mm to fit in the SEM chamber.

b) The suitability for surface preparation (using manual method if needed), such as grinding.

c) Economical design to ensure enough samples for several experiments.

d) Insignificant effect on the notch region.

The ASTM B831-05 specimen, as shown in Figure 3.1, has dimensions of 114.0 mm × 38.1 mm × 6.35 mm. The modified specimen has dimensions of 50.0 mm × 25.0 mm × 6.0 mm. A comparison between both specimens is shown in Figure 3.3.

A study of strain at the gauge region will be carried out to ensure that the change in the specimen global dimensions from the ASTM B831-05 specimen has an insignificant effect on the specimen's gauge region. This study is carried out at specimen elongation of 0.58 mm for both designs. This displacement

results in a shear strain at the specimen's notch area of approximately 40%. The comparison for the predicted plastic strain contour plot has been presented in Figure 3.4 which shows a close similarity for the predictions between the two specimens (Figure 3.5).
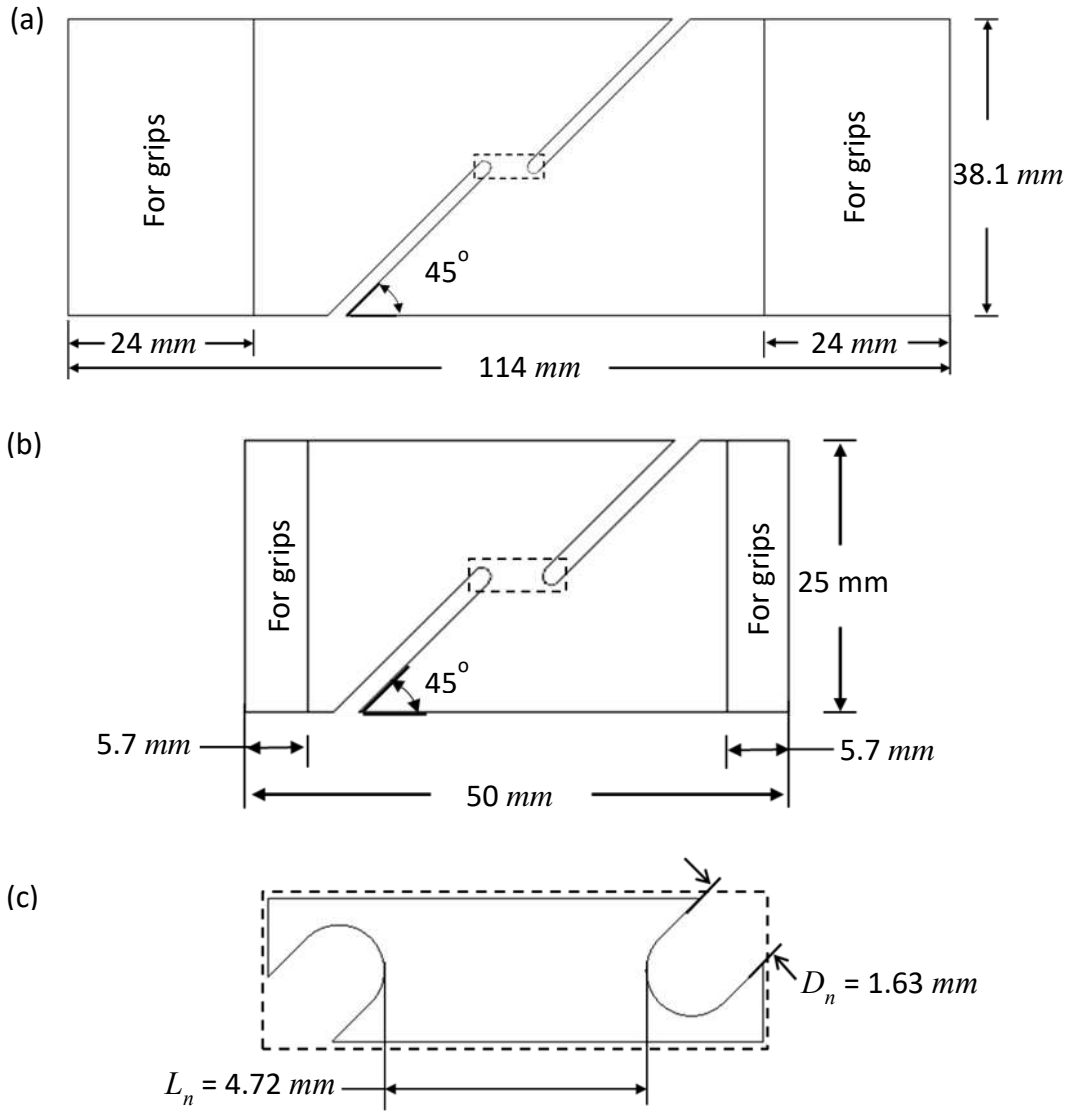
Figure 3.3: Comparing (a) the ASTM B831-05 specimen, (thickness 6.35 mm), (b) the specimen after global modification, (thickness 6.00 mm), and (c) the dimensions for the gauge region.

3.3 Modifying Shear Specimen's Local Dimensions (Notch Region)

The length of the specimen's notch region, L_n, (see Figure 3.6) is modified to ensure a uniform shear strain at the specimen's notch. The uniformity of the shear strain at the notch region is important to facilitate the experiment as well as the computational study of the shear deformation at the notch region. In this research, the specimen deformation at the notch region will be investigated using digital image correlation (DIC) from one side of the specimen, to measure the shear strain at the notch region and using electron backscatter diffraction (EBSD) from the other side, to measure deformation-induced

crystal reorientation. Having a uniform shear strain at the notch region will facilitate comparing the experimental results with the computational predictions, assuming that the identified area at the notch region is almost the same for both sides. Also, in the computational FE model, an element at the notch region will be discretised using the sub-model in Abaqus, to simulate the deformation-induced crystal reorientation. Thus, having a uniform shear strain at the notch region will overcome several challenges regarding this study.

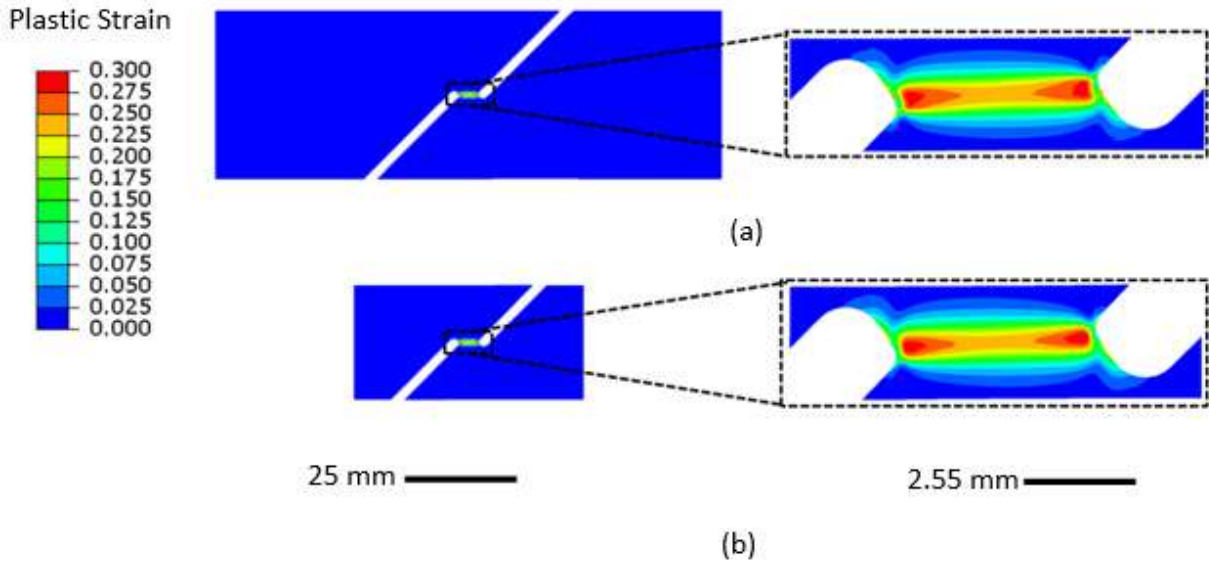**Figure 3.4:** Studying the predicted effect of global modifications for ASTM specimen on the specimen's notch region for P91. (a) ASTM B831-05 specimen, (thickness 6.35 mm), and (b) is specimen after global modification, (thickness 6.00 mm).
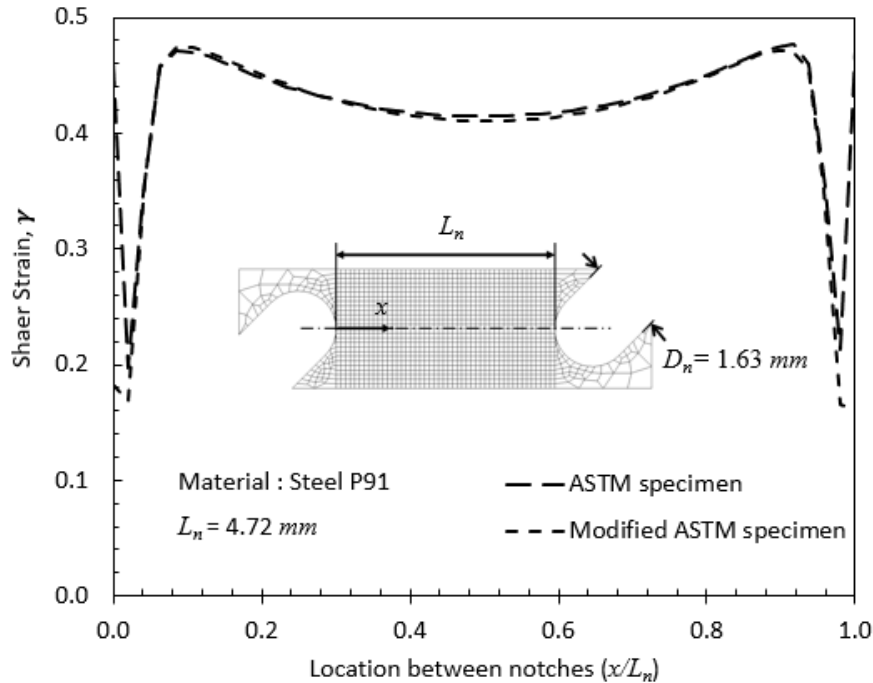
Figure 3.5: Predicted effect of global modifications for shear strain distribution at specimen's notch region.
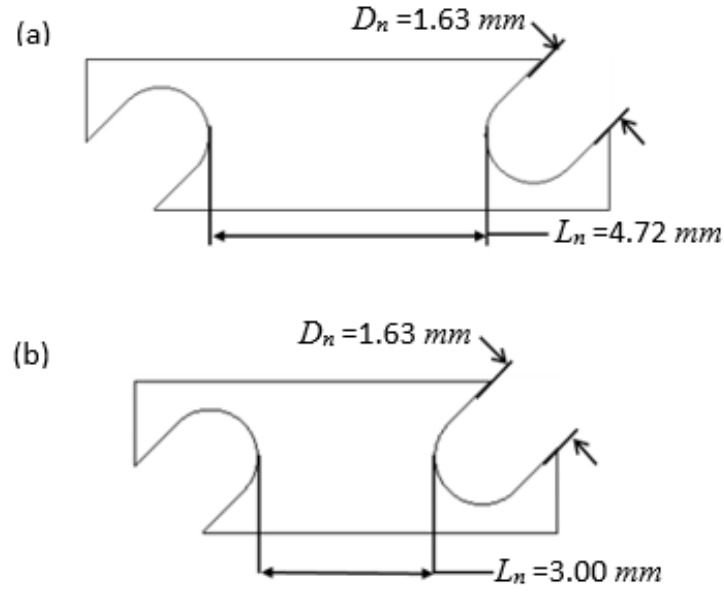
Figure 3.6: The modification to the notch region, (a) ASTM with Ln = 4.72 mm, (b) Ln = 3.00 mm.

Figure 3.7: Predicted effect of decreasing notch region length for using P91 specimen on shear strain distribution (a) ASTM specimen, and (b) specimen with modified notch region.

The plastic strain is found to be localised between the notches with low strain at the area around the notches, as shown in Figure 3.7 for steel P91, and in Figure 3.8 for steel X100. Decreasing L_n has enhanced the uniformity of shear strain distribution for P91 steel, as shown in Figure 3.7 and Figure 3.9, while it has an almost insignificant effect for X100 steel as shown in Figure 3.8 and Figure 3.10. The predicted difference in response of P91 and X100 to the decrease in L_n / D_n ratio, is due to the difference in stress-strain behaviour for both (Peirs et al., 2012b), as shown in Figure 3.2.

Finally, the shear strain has been normalized with respect to the true strain at 0.2% proof stress for both X100 (ε_y = 0.0065) and P91 (ε_y = 0.0053) and plotted versus the true strain of specimen

19

elongation divided by the length between the notches as shown in Figure 3.11. This figure will enable the identification of the specimen elongation needed to achieve the required shear strain at the notch region.
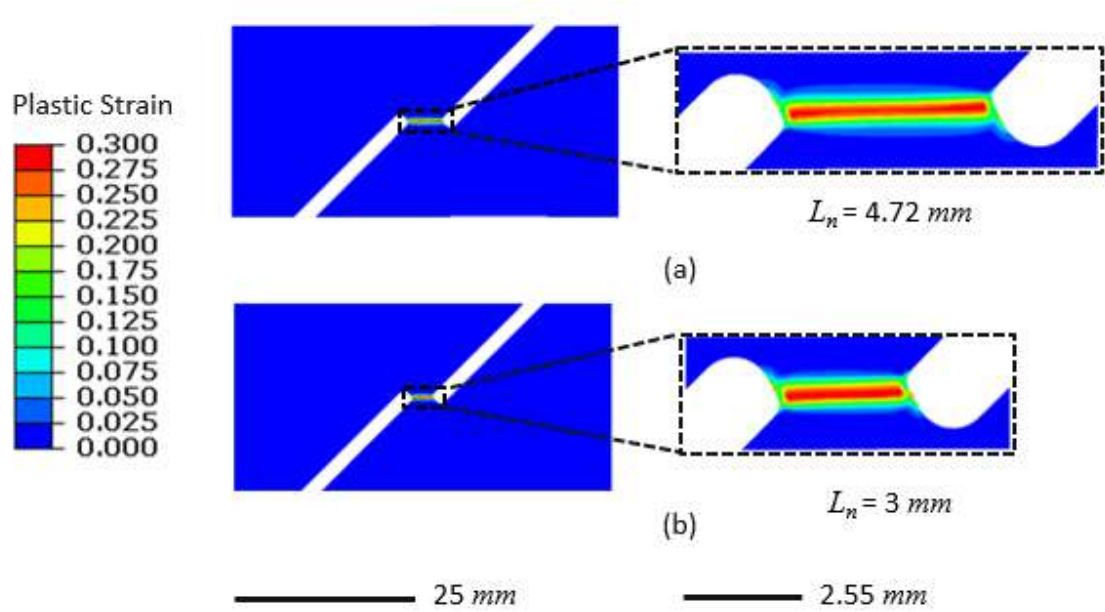
Figure 3.8: Predicted effect of decreasing notch region length for using X100 specimen on shear strain distribution (a) ASTM design, and (b) modified notch region.
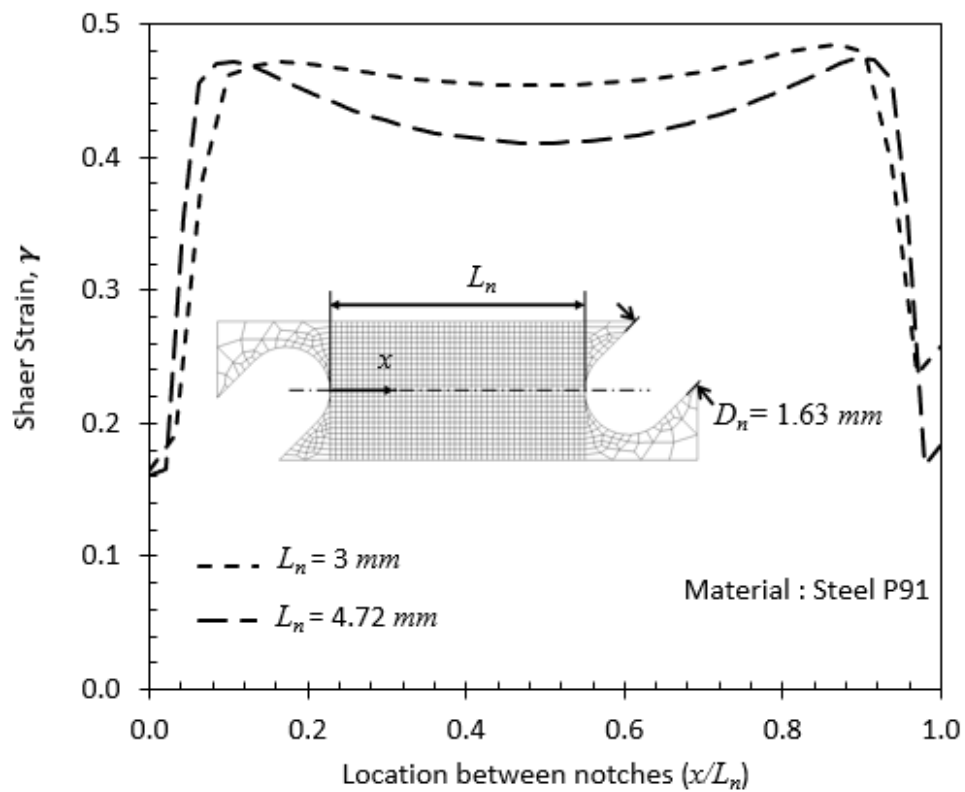
Figure 3.9: Predicted effect of modifying the notch region length for P91 specimen on shear strain distribution.

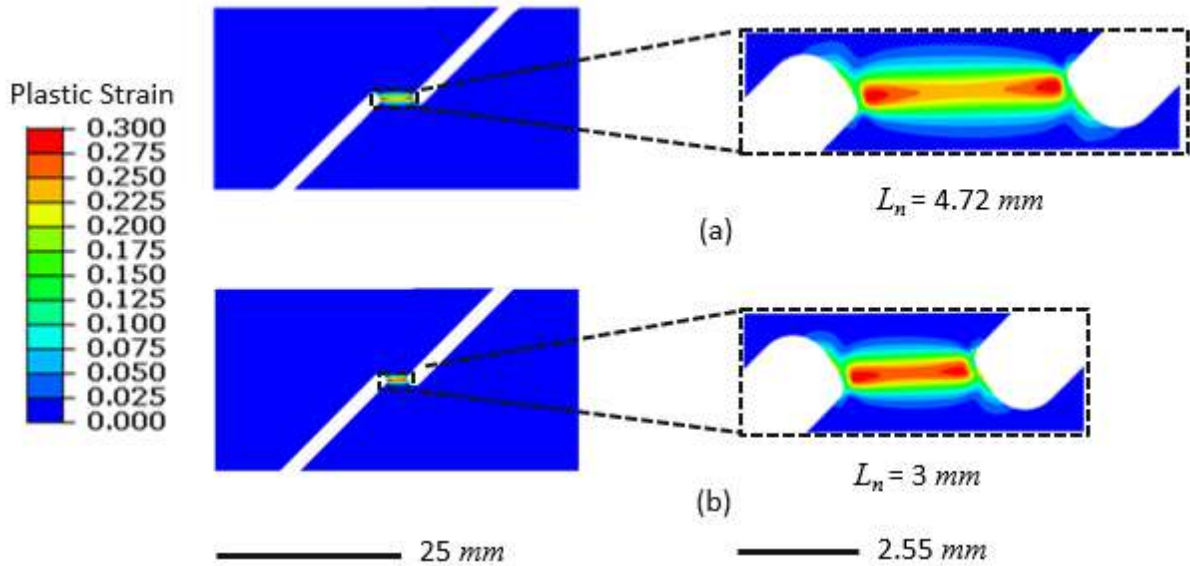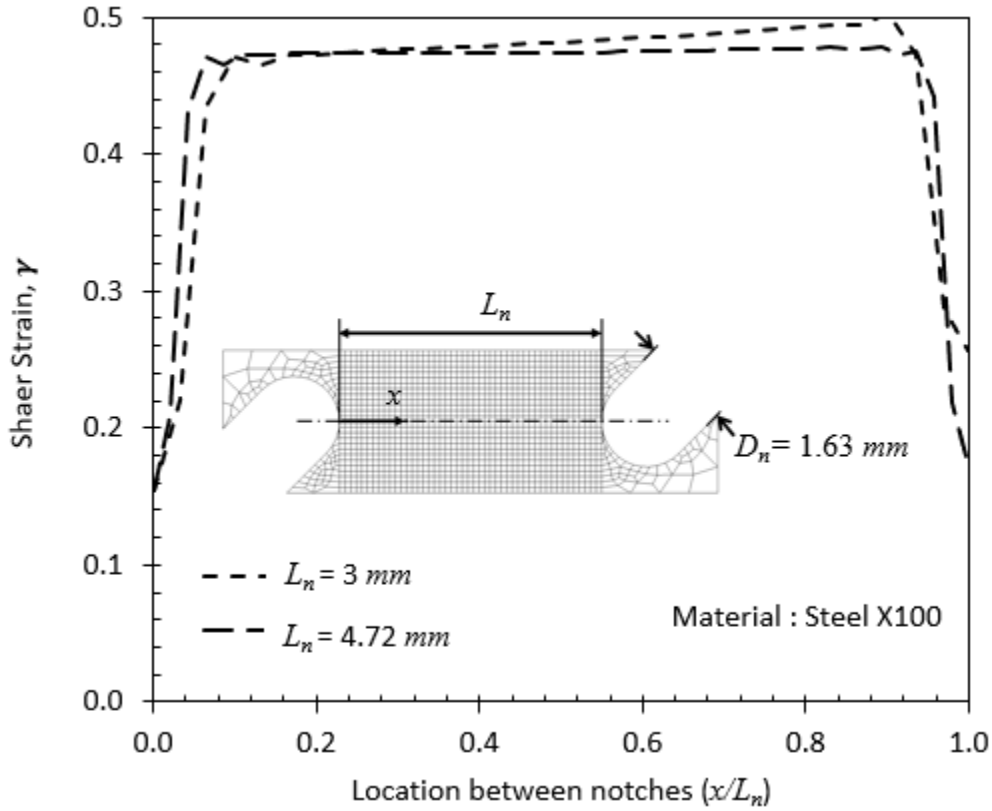**Figure 3.10:** Predicted effect of modifying the notch region length for X100 specimen on shear strain distribution.

3.4 Mesh Sensitivity Analysis

To ensure that the numerical results are mesh-independent during the current study a mesh sensitivity analysis has been performed. For this analysis[2], five cases have been used: very fine mesh, fine mesh, normal mesh, coarse mesh, and very coarse mesh as shown in Figure 3.12. This study has been performed on P91 steel. A finite element (FE) model based on isotropic von Mises plasticity in Abaqus, with piecewise-linear hardening (*PLASTIC in Abaqus), has been used to carry out the mesh sensitivity analysis. The data used are taken directly from Figure 3.2 for P91. The modulus is defined using the *ELASTIC keyword in Abaqus, with the value again taken from Figure 3.2.

Studying the mesh sensitivity has been done in two steps, the first step is concerned with studying the effect of mesh sensitivity on the local deformation using von Mises stress and plastic strain at the gauge region, and the second step is concerned with the global effect of mesh sensitivity on force–displacement results. Finally, the decision for the optimum mesh size has been made through the study of the run-time required by each case.

---

[2] This is following ('section 4.4 Mesh convergence', Abaqus online documentation: version 6.6-1), however 'normal mesh' does not refer to optimum or standard mesh.

The predicted effect of mesh size on the local deformation at the gauge region for the von Mises stress and the plastic strain are shown in Figure 3.13 and Figure 3.14, respectively. The study of those two figures shows that the fine mesh case and very fine mesh case have similar results for the von Mises stress and the plastic strain evolution profile at the gauge region. On the contrary, comparing the von Mises stress and plastic strain profile at the gauge region for the other three cases show an obvious divergence. Also, the contour plotting shows irregular changes in contour values close to the notch region for the other three cases, but it is a smooth contour at the notch region for the very fine mesh and fine mesh.

The results for the force-displacement simulations have been plotted in Figure 3.15, where a fixed displacement is applied to the loading pins, so the maximum load varies between the five models. These variations have been studied in Figure 3.16, where a figure illustrating the change in the maximum load versus the number of elements, as well as the run time (RT) which has been used for each simulation. From this analysis, it has been concluded that the fine mesh case is the optimum case to be used as it provides the lowest RT given that the value of the maximum load is very close to the case with a very finer mesh. The percentage difference between the maximum load for the very fine mesh and fine mesh is 0.4%. In addition, the study of the effect of mesh sensitivity on local deformation has shown that the results for the very fine mesh case and the fine mesh case are similar.
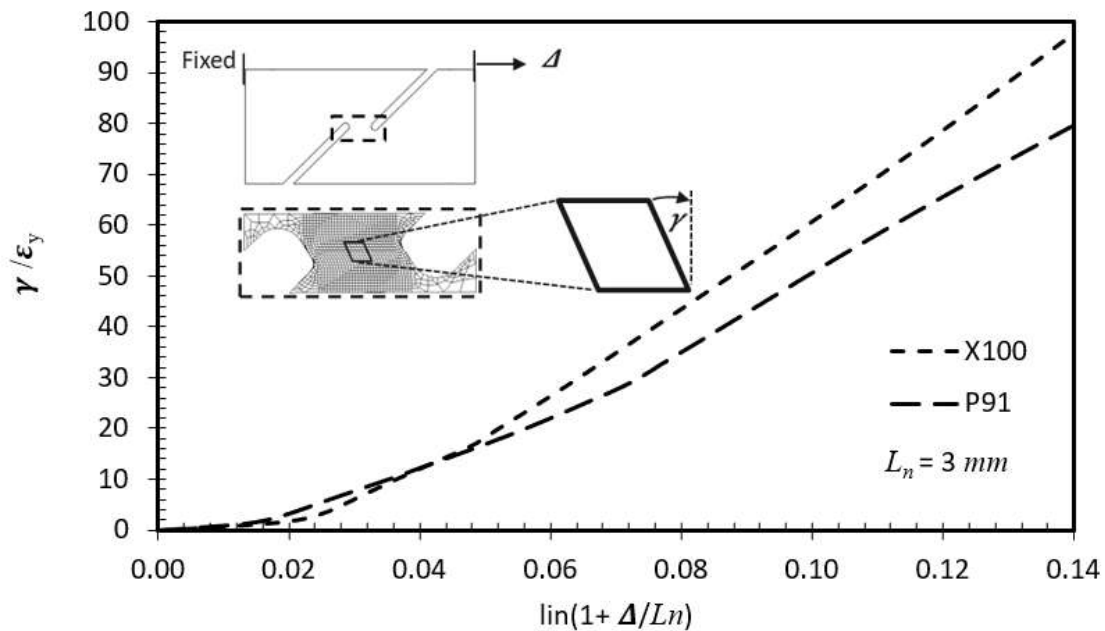
Figure 3.11: Relation between the shear strain (normalized by strain at 0.2% proof stress) and the normalised displacement, for P91 ($\varepsilon_y = 0.0053$) and X100 ($\varepsilon_y = 0.0065$).
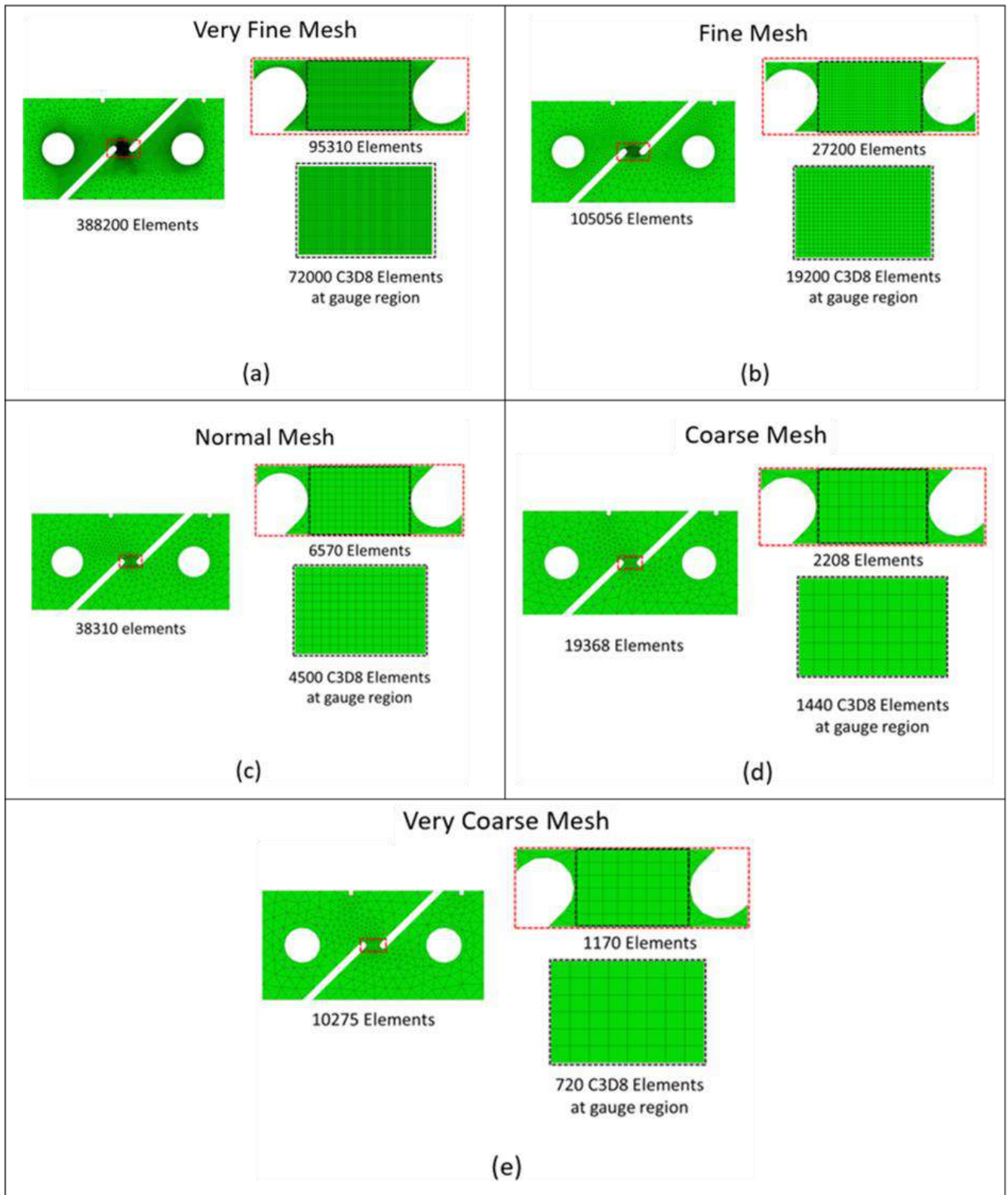
Figure 3.12: The five cases for studying the mesh sensitivity.
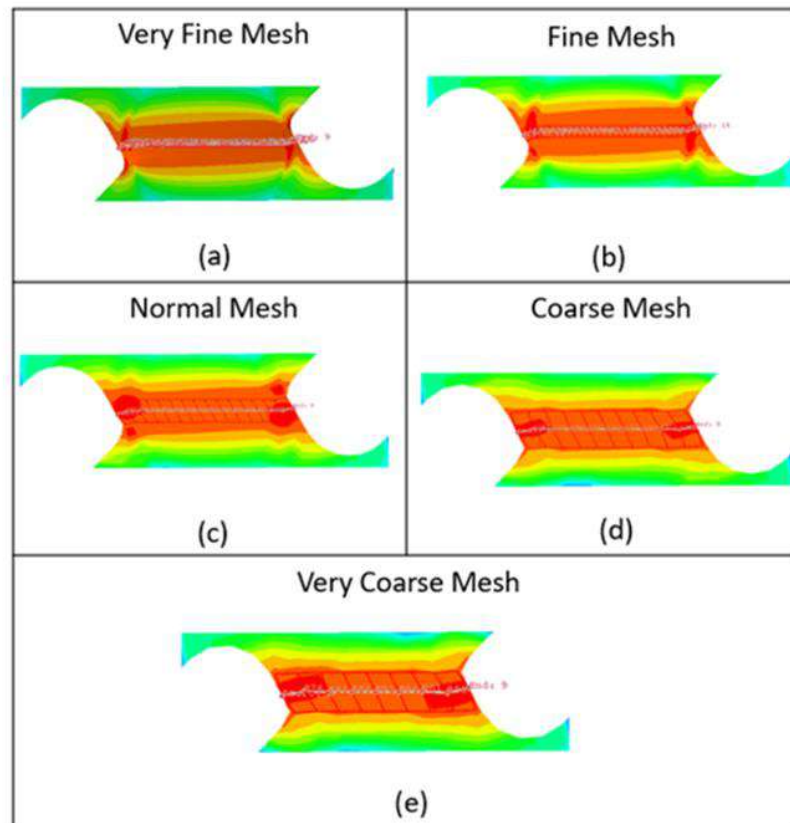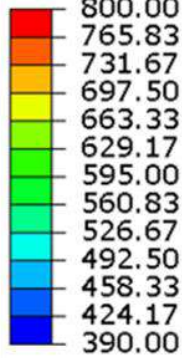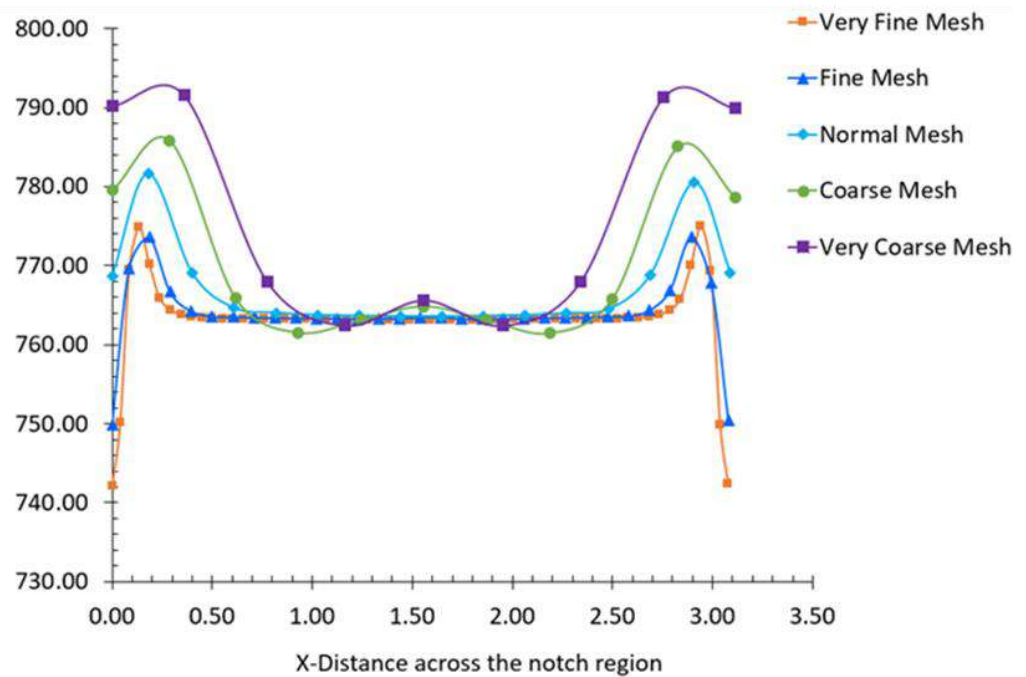
Figure 3.13: Studying the effect of mesh sensitivity on the evolution of von Mises Stress at the gauge region, (A) is the contour plotting for von Mises stress for the five cases, and (B) is a quantitative comparison between the profile of von Mises stress along the gauge region for the five cases.
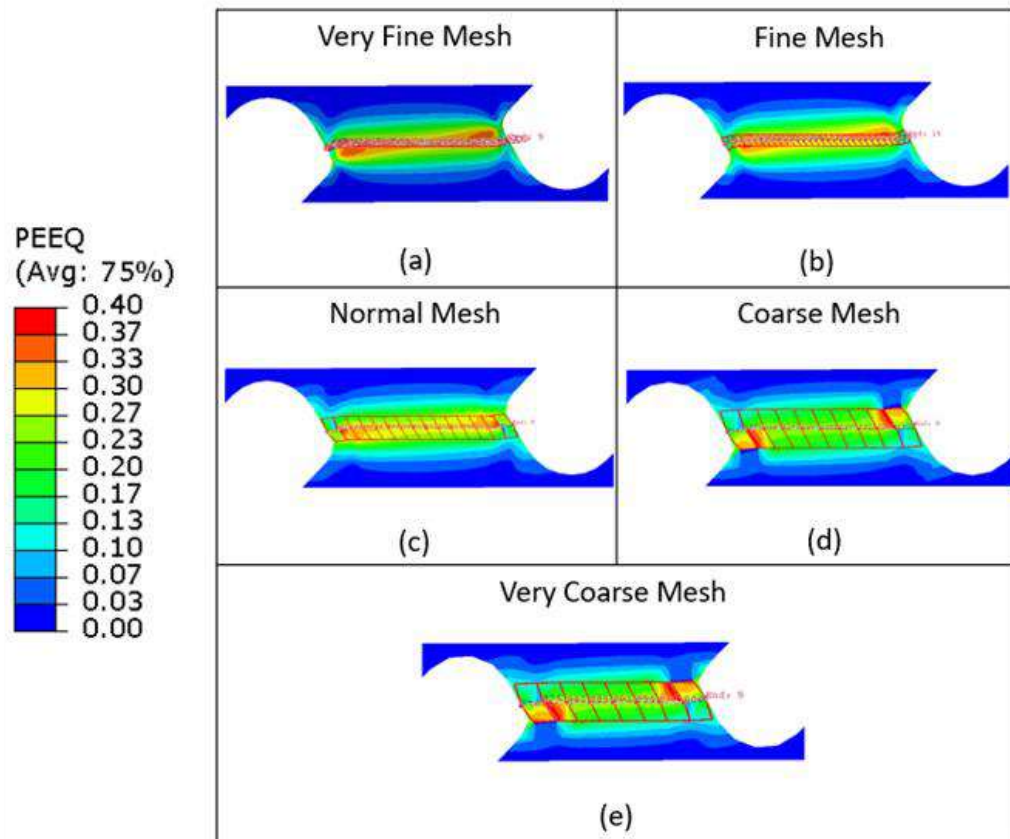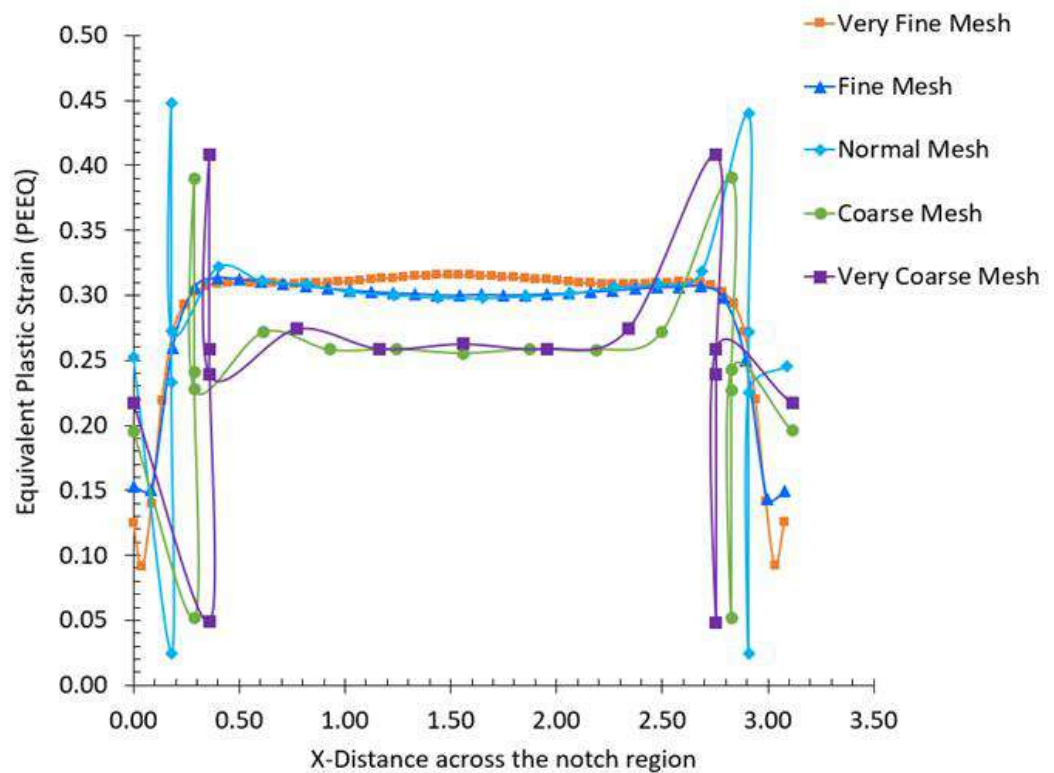
Figure 3.14: Studying the effect of mesh sensitivity on the evolution of von Mises Stress at the notch region,(A) is the contour plotting for plastic strain for the five cases, and (B) is a quantitative comparison between the profile of plastic strain along the gauge region for the five cases.
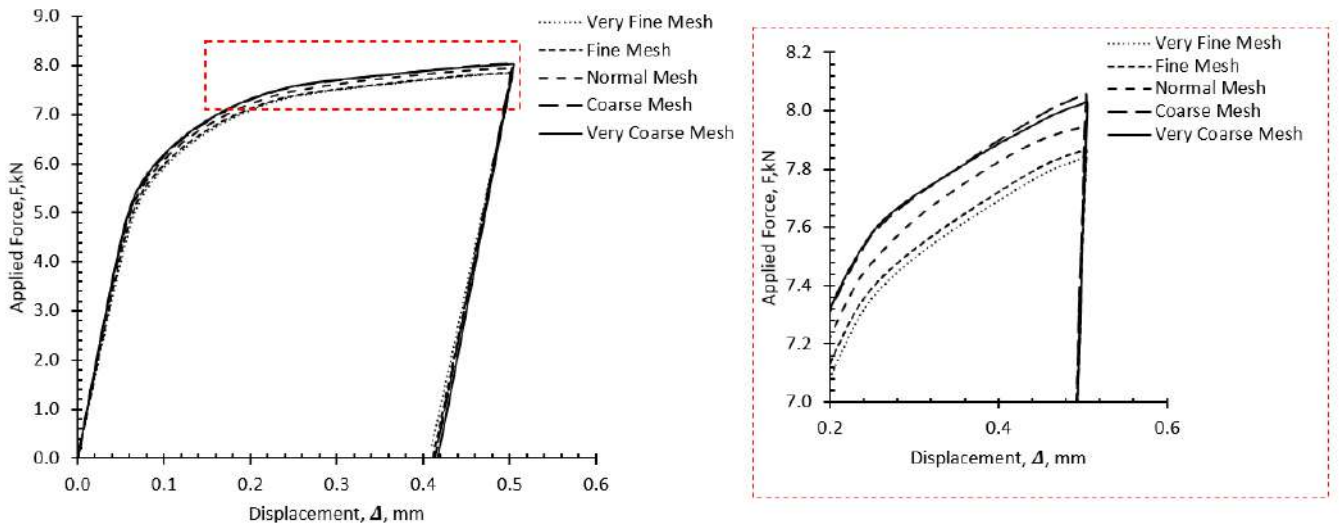
Figure 3.15: Studying the effect of meshing on the maximum force.
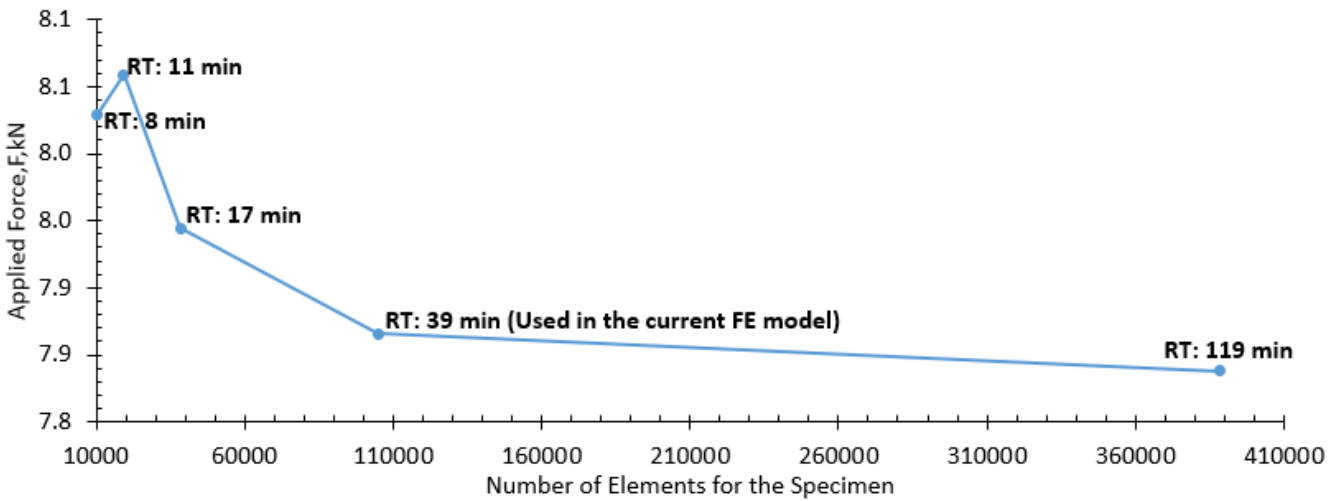
Figure 3.16: Comparison of the number of elements, maximum applied load, and time taken by each simulation.

3.5 Conclusion

In this chapter, the ASTM B831-05 standard specimen for shear strain testing has been modified. Two main modifications have been carried out to achieve this goal. The first is to modify the global dimensions, which have been modified from (114.00 mm × 38.10 mm × 6.35 mm), to (50.00 mm × 25.00 mm × 6.00 mm). The second modification is to modify the notch region dimensions; this has been modified, so the value of length between notches (L_n) changed from 4.72 mm to 3.00 mm. The second modification enhanced the uniformity of the strain distribution between the two notches for steel P91, while it had an insignificant effect for the case using steel X100.

The designed specimen has been manufactured and tested at the University of Limerick as part of the overall research programme. In the next chapter, a multi-scale FE simulation of the proposed specimen has been completed and validated against experimental results for P91.

Chapter 4: Multiscale Finite Element Modelling of P91

4.1 Introduction

The multi-scale or multiresolution finite element (MRFE) modelling of metallic materials has become popular since the development of the crystal plasticity theory as a methodology to computationally model plasticity induced in crystalline materials, thus introducing the micromechanics deformation in the continuum model (Asaro, 1983). The ability to study the deformation of the material on several scales from the macroscale deformation to the crystal-scale at adequate computational cost and good accuracy has opened the door for deep development in the scientific research concerning crystalline materials modelling (Asaro, 1983; Belytschko et al., 2014).

Modelling the microstructure evolution for the MRFE models has relied on the crystal plasticity theory described by Asaro (1983). This theory is based on the crystallographic slip as the mechanism for the plastic deformation of crystalline materials. The kinematic theory for elastic-plastic deformation, in which the inelastic deformation is based on the crystallographic slip, is based on the flow of the material through the crystalline lattice via dislocation motion for describing the inelastic deformation, while the lattice with the material embedded in it undergoes elastic stretch and rotation. This plastic flow is represented by the slipping rate, $\dot{\gamma}^{\alpha}$, of the slip system α. The stress to generate the crystallographic slip is the resolved shear stress, which is the component of the shear stress resolved in the slip plane and in the slip direction. The flow rule used in the current study is based on the flow rule developed in Busso (1990), which has been originally developed to create a micromechanical model for cubic oriented NiAl crystals at high strain level (approximately between 30% to 40%) and high temperature (at 750 $^{\circ}$C and 850 $^{\circ}$C). This model has efficiently predicted the dependence of the flow stress on the temperature, the strain rate, and the resistance for dislocation motion and interactions. This flow rule has been used in several studies (D.-F. Li, 2016; D.-F. Li et al., 2017; Meade et al., 2021; Sun et al., 2019) to develop the crystal plasticity model for the microstructure evolution of tempered martensitic steel.

Several studies have been conducted to develop multiscale models for the deformation of martensitic steel P91. In Golden et al. (2016) the room temperature deformation of a miniature notched three-point test specimen, manufactured from P91 has been investigated. The deformation of this specimen has been investigated on two length scales, the specimen scale (mm length scale) to capture the global deformation, and the micro-level scale (μm length scale) to capture the microstructure evolution during the material deformation. A crystal plasticity model has been used to capture microstructure evolution for the representative volume element (RVE), which has been identified directly at the notch root. The boundary conditions applied on the RVE are the nodal displacements

obtained from the global length scale analysis. The plastic strain was not uniform in the RVE; it varied from more than 20% just above the root, to less than 2% away from the root. This model has been validated with the experimental results for the global deformation scale, in which the results for the notch opening and the force-displacement cure have been used. For the microstructure analysis, the crystal orientations based on the EBSD scan after deformation have been compared with simulation results for randomly selected regions in the RVE. Although good agreement has been obtained between the experimental results and the multiscale model, the plastic strain at the investigated blocks (for microstructure analysis) was not uniform, and it was difficult to validate. Following this methodology, in Meade et al. (2018b), a modified compact tension test specimen of P91 has been investigated. Similar to the previously described methodology, the deformation on two-length scales has been investigated. The RVE has been modelled using the crystal plasticity model, and the boundary conditions for the RVE have been applied from the global deformation scale to the RVE. The global scale deformation model has been based on isotropic elastic-plastic model, in which the material behaviour has been based on experimental stress-strain data. This study has been performed at 500 °C, which is representative temperature for in-service conditions. This model results have shown very good agreement compared with the experimental results for the global deformation. However, due to the low strain level the changes in crystal orientations were small so validation at the local level is difficult. A high strain level was not possible for this specimen, as at a high strain level high indexing for the EBSD scan was not possible (Meade, 2020). In Meade et al. (2021) a similar methodology has been used to model the deformation of a P91 tensile test specimen at high plastic strain. For the macroscopic (global) model, the von Mises plasticity model in conjunction with a Gurson-Tvergaard-Needleman damage model has been used to simulate the macroscale damage evolution. For the microscale model, a crystal plasticity model incorporating damage variables has been used. This model demonstrated that the initially randomly oriented crystals approach the stable [011] orientation under applied tensile load. It also showed that at large plastic deformation, the grains can be subjected to refinement and coalescence. The integration of crystal plasticity in an FE framework has been also used to model the fatigue of steel Grade 91. In D. F. Li et al. (2016) a micromechanical FE model has been developed to simulate the cyclic plasticity and fatigue crack initiation (FCI) behaviour of P91 under thermo-mechanical fatigue conditions. The EBSD data have been used to reflect the microstructure of the material; these data have been imported into the crystal plasticity model. This model has predicted well the cyclic thermo-mechanical response compared with the experimental results for in-phase (the sign of the mechanical cycle is the same as for the thermal cycle) and out-of-phase (the sign of the mechanical cycle is opposite to the thermal cycle) conditions. The out-of-phase thermo-mechanical response is identified as more dangerous than the in-

phase thermos-mechanical response for in fatigue crack initiation, this result is consistent with the experimental failure data. Also, this model has shown that it can effectively predict the behaviour of thermo-mechanical fatigue for P91 at the microstructural level. Arising from the importance of studying the role of microstructure evolution at the sub-grain level in terms of coarsening of laths and precipitates on crack initiation for understanding the cyclic failure response of P91, D. F. Li et al. (2017) have developed a multi-scale crystal plasticity model for P91 experiencing cyclic plasticity and low-cycle fatigue at elevated temperature. In this model, the geometry of grains, the sub-grains, and the $M_{23}C_6$ precipitates have been included in the microstructure model. The strain gradient effects and the kinematic hardening have been included in the crystal plasticity formulation. This model has shown good agreement with the experimental results for hysteresis stress-strain loops. Also, the $M_{23}C_6$ precipitates have shown to introduce kinematic hardening to P91 steels, as well as its coarsening at elevated temperature have a detrimental effect on the cyclic response and low cycle fatigue life of P91 steels. In this context, Sun et al. (2019) have developed a strain gradient crystal plasticity model integrated to FE framework to model the Inelastic deformation of (P91). Modelling hierarchical structure of P91 has been done using the Voronoi tessellation, in which the effect of prior austenite grain (PAG)/packet/block size on the macro- scale and micro-scale mechanical response has been simulated. This model has shown that the overall mechanical response is determined by the block size, which is consistent with the Hall-Petch relation. The microplastic strain distribution has been shown to be influenced by the packet and block diameters. Crystal plasticity modelling has also been used by e.g., (Dunne et al., 2007, 2012; T. Zhang et al., 2014) often in combination with EBSD, to examine deformation and crack initiation in polycrystalline metals. In Dunne et al., 2007, it was shown that the presence of a 'rogue grain' with a particular unfavourable orientation can lead crack nucleation in HCP Ti-alloys. In T. Zhang et al., 2014, high-resolution EBSD, was used to obtain the strains and rotations in a Ni-alloy and the information was used to predict fatigue nucleation for the alloy. In Chen et al. (2014) micropillars have been extracted from a dual-phase (ferrite-martensite) steel, each consisting of a single martensite or ferrite grain, have been tested under compression and compared to modelling predictions. The modelling results have been used to explain the deformation behaviour of two dual-phase steels with very different microstructures.

In this research, a similar methodology to that used in Meade et al. (2018b), for MRFE modelling has been used. The macroscale finite element model has been used to predict the force-displacement global deformation, as well as the strain deformation at the specimen gauge region. The displacement field for the 3D-FE model is delivered using the sub-modelling scheme in Abaqus to the area of interest

within the gauge region as a boundary condition. The crystal plasticity material model is integrated into Abaqus using a user material (UMAT) subroutine.
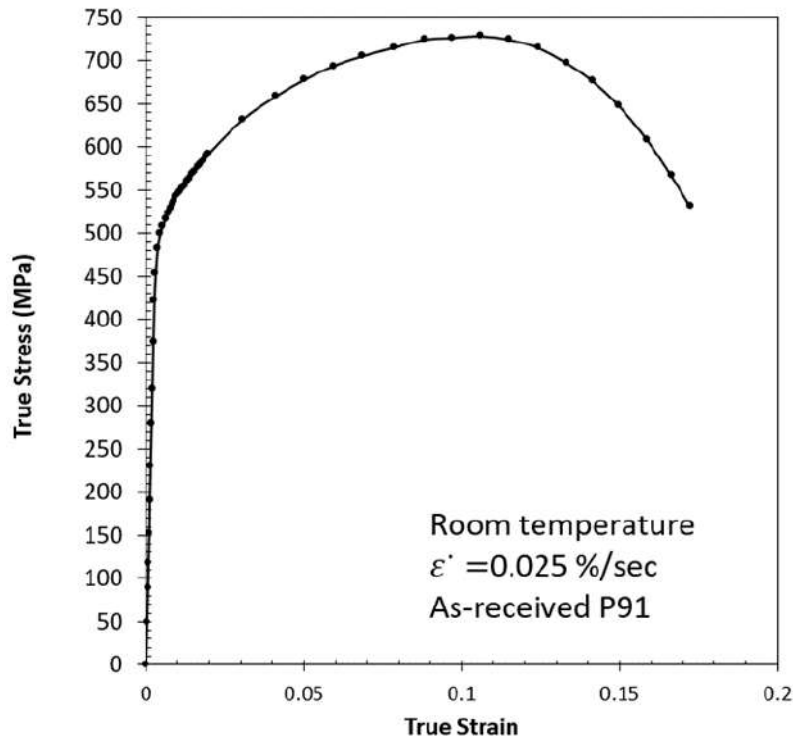
Figure 4.1: Experimental uniaxial stress-strain data for P91 at room temperature (Meade, 2020).

This chapter aims to describe the MRFE modelling of martensitic steel at high shear strain and validate the numerical results using experimental techniques. It is organized as follows, following the introduction, the second section discusses the macroscale finite element modelling, which includes the modelling of the shear specimen on the macroscale level and verifying the results using force-displacement experimental results. The second part of the second section is concerned with verifying the FE strain results at the gauge region, and the numerical results will be verified using the DIC experimental technique. The third section focuses on the crystal-plasticity modelling of the specimen at the gauge centre, where the crystal plasticity finite element (CPFE) results will be verified using the electron back scatter diffraction (EBSD) technique, which captures the crystal orientations pre- and post-deformation. The final section represents the conclusion and the summary of the key points of this chapter.

4.2 Macroscale Finite Element Modelling

A FE model based on isotropic von Mises plasticity in Abaqus has been used to simulate the global force-displacement for the shear specimen as well as simulating the shear strain at the gauge region. The stress-strain experimental data as shown in Figure 4.1, used for this model has been based on the work done by Meade et al. (2020). The P91 mechanical response is not sensitive to strain rate at room

temperature, as shown in Figure 4.2. Thus, although there is some difference in strain rate between the shear tests and the tensile test from Meade et al. (2020), which has been used to create the input material data for Abaqus, the effect is not expected to be significant.
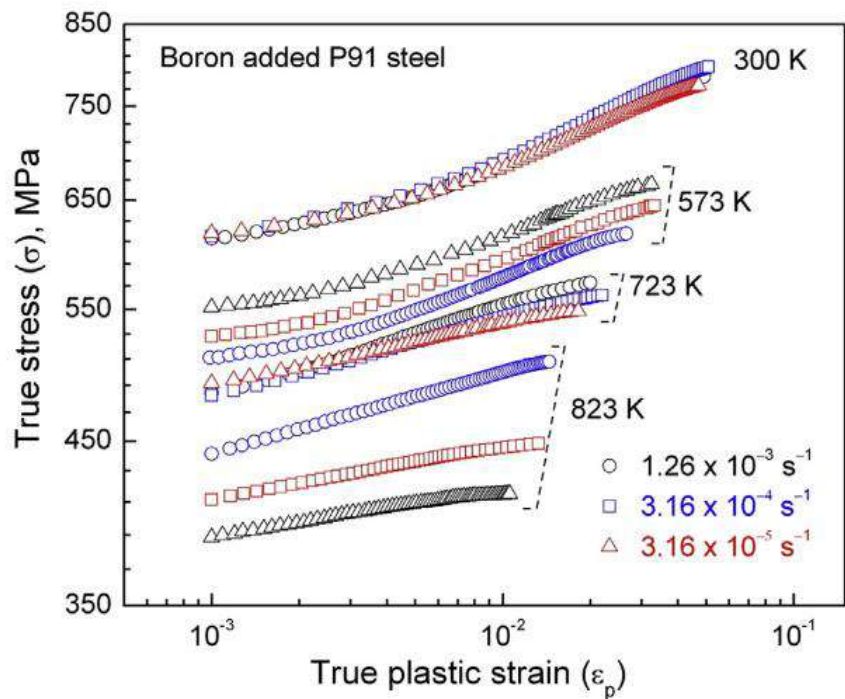
Figure 4.2: The effect of temperature and strain rate on the true stress and true plastic strain behaviour of Boron-added P91 steel (Choudhary & Christopher, 2019).
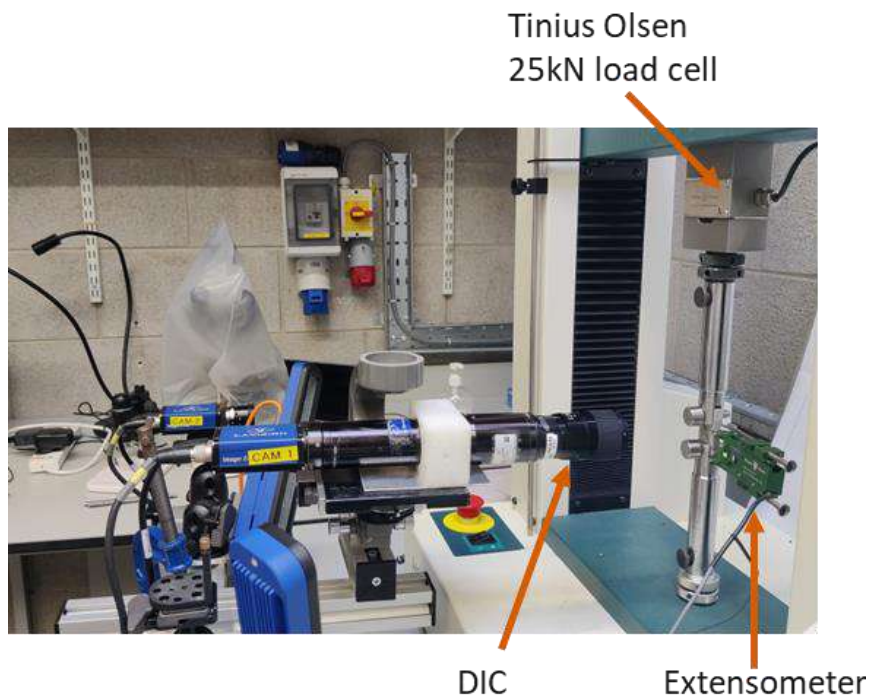
Figure 4.3: The shear test experimental setup, including the DIC camera and extensometer.

The experimental setup is shown in Figure 4.3, where the Tinius Olsen machine has been used to apply the load on the specimen and digital image correlation (DIC) has been used to capture the strain

deformation at the gauge region. The specimen has been prepared so both sides will be used for different measurements. As shown in Figure 4.4, one side will be used for the DIC shear strain measurement, which is recorded during the test, and the other side is prepared for the EBSD measurement, pre-deformation and post-deformation. The side for EBSD has been prepared with wet grinding, polishing, and broad ion beam milling, but the DIC side has been prepared with wet grinding, and a layer of speckles (the speckle diameter is approximately 0.1 mm) has been created on this side of the specimen. These speckles will be tracked by the DIC camera to calculate the shear strain at the notch region.

(a)

(b)
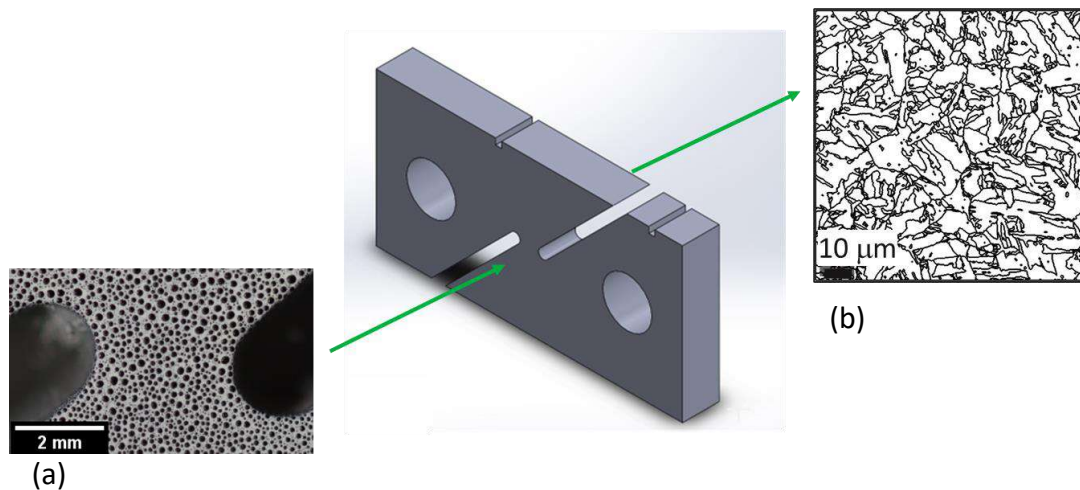
Figure 4.4: Surface preparation of the shear specimen on both sides, (a) For the side to be measured using DIC, and (b) For the side to be measured using EBSD.
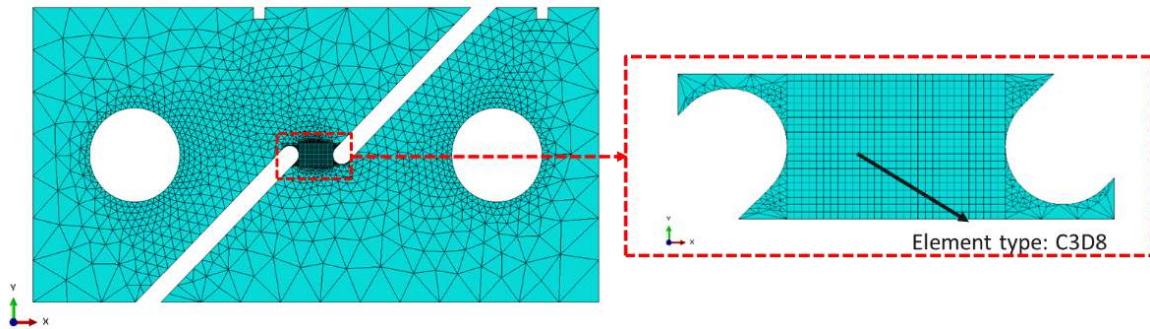
Figure 4.5: Finite Element Model.

4.2.1 Finite Element Mesh

The finite element model, as shown in Figure 4.5, is a 3D model in Abaqus. The number of elements at the gauge area is 19200 cubic-eight nodes brick element (C3D8), based on the convergence study done in Section 3.4. The use of linear C3D8 elements will also facilitate the transfer of the displacement field from the macroscopic FE simulation results to the crystal plasticity model, which has been constructed to create a realistic microstructure based on EBSD crystallographic orientation measurements. This is discussed in detail in section 4.3. The grooves at the top of the specimen (shown in Figure 4.4 and

Figure 4.5) are used to measure the displacement, whereas the extensometer will measure the displacement, as shown in the experimental setup in Figure 4.3.

4.2.2 Loading Conditions

The loading conditions are shown in Figure 4.6. The pins have been simulated as rigid bodies to reduce the computational cost, without affecting the global results for the force-displacement results. The boundary conditions have been applied at the pins' reference points, which constrains the motion and rotation for one of the pins in the X and the Y directions while allowing the motion of the other pin in the X-direction; these constraints correspond to that applied experimentally.
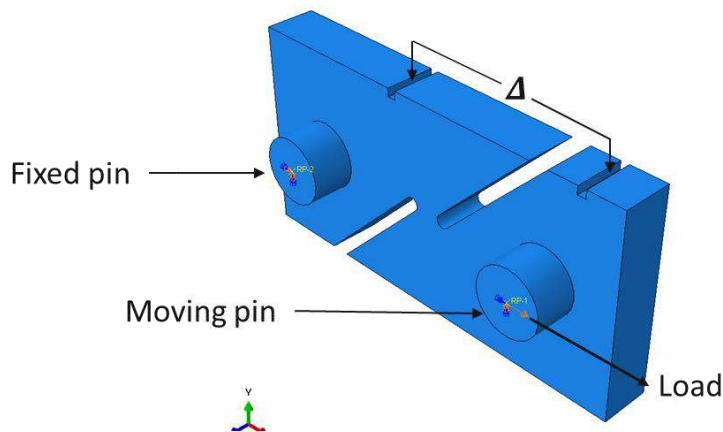
Figure 4.6: The boundary and loading conditions.
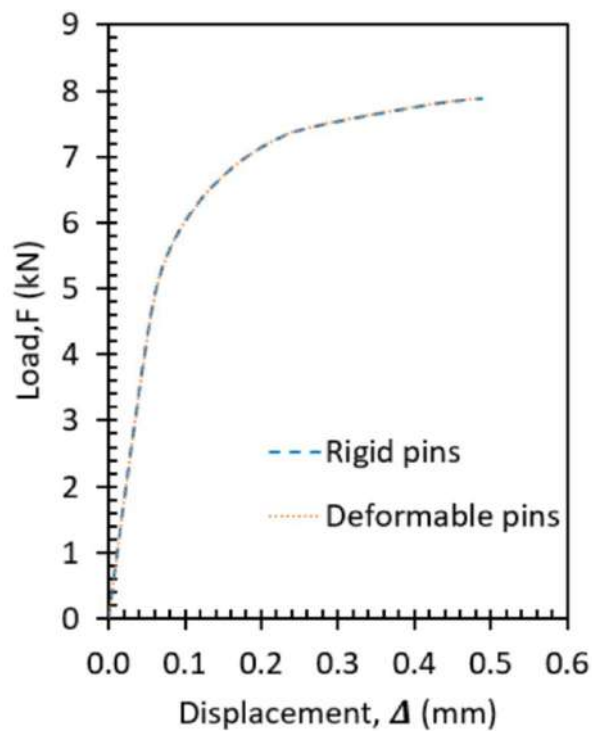
Figure 4.7: Study the effect of using deformable pins and rigid pins for the FE model.
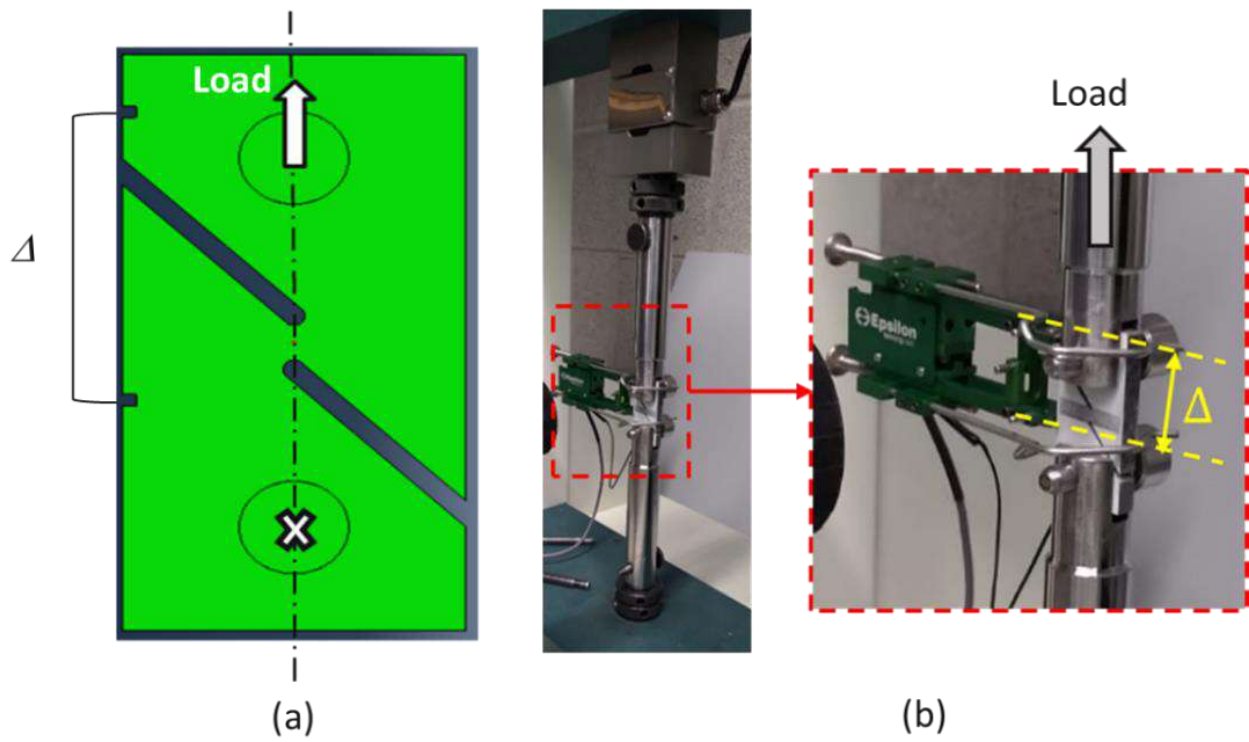
Figure 4.8: Measuring the load-displacement results for (a) FE model, and (b) experimental setup.
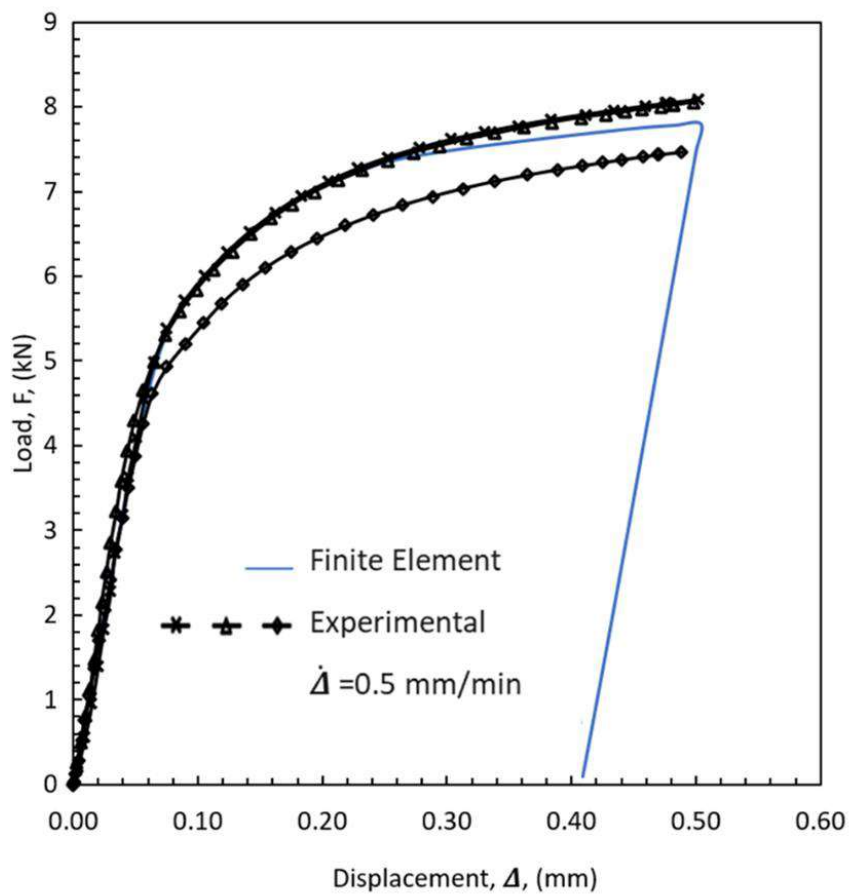
Figure 4.9: Comparison between load-displacement results for the FE and the experimental data for P91.

The predicted effect of the pins simulated as rigid body or deformable body, on the force-displacement results is shown in Figure 4.7. For simulating the pins as deformable bodies, the pins material is steel Uddeholm Impax Supreme, which modulus of elasticity is 205 GPa, the yield strength is 900 MPa, and the ultimate tensile strength is 1020 MPa. The results show that the pins could be simulated as a rigid body, which will reduce the computational cost.

4.2.3 Validating The Global Force-Displacement Results

The load-displacement results are obtained by measuring the displacement at the groves where the extensometer is placed, and the load is obtained from the load cell. The force and displacement results have been collected similarly for the FE simulation, as shown in Figure 4.8. The comparison between the experimental and the FE results for load displacement is shown in Figure 4.9.

These results show good agreement between the experimental and FE results, given that there is variability (scatter) in the experimental measurements and noting that the stress-strain data from a tensile test (Figure 4.1) has been used in the shear test Abaqus model. An unloading step has been applied in the FE simulation, as EBSD measurements will be done ex-situ, so the specimen is unloaded before the EBSD measurement.

4.2.4 Correlating Finite Element Strain to DIC Strain

As the FE and the DIC software use different algorithms to calculate shear strain, it is important to correlate the two ways of measurement, to be able to compare shear strain results from both to validate the FE results.

4.2.4.1 DIC Strain Measurement

Based on the DIC software DaVis 8.1 Software (LaVision, 2013), the grid to calculate the shear strain is presented schematically in Figure 4.10. Her (x, y) represents the coordinate of a node located at point (n, m) in the DIC grid, θ represents the induced shear angle after deformation, and 'vector grid' is the constant constructing the grid for shear strain calculations. The calculation of the shear strain at node (n, m) is as follows:

$$\varepsilon_{xy}(n, m) = \frac{U_x(n, m + 1) - U_x(n, m - 1)}{2.\,\text{Vector grid}} = \tan \theta_{n,m} \qquad 4.1$$

where U_x is the induced displacement along the X-direction. In the DIC software the average shear strain is the shear strain calculated as follows:

$$\text{Average shear strain} = \frac{1}{2} \times \left(\varepsilon_{xy} + \varepsilon_{yx}\right) = \frac{1}{2} \times \left(\frac{\partial U_x}{\partial y} + \frac{\partial U_y}{\partial x}\right) \qquad 4.2$$

Assuming simple shear, thus

$$\frac{\partial U_y}{\partial x} = 0 \qquad\qquad 4.3$$

Applying Equation 4.3 in Equation 4.2, the average shear strain is

$$\text{Average shear strain} = \frac{1}{2} \times \left(\varepsilon_{xy}\right) = \frac{1}{2} \times \left(\frac{\partial U_x}{\partial y}\right) \qquad\qquad 4.4$$

Finally, using Equation 4.1 and Equation 4.4, the shear strain angle could be calculated using the following:

$$2 \times \text{Average shear strain} = \varepsilon_{xy} = \tan \theta_{n,m} \qquad\qquad 4.5$$
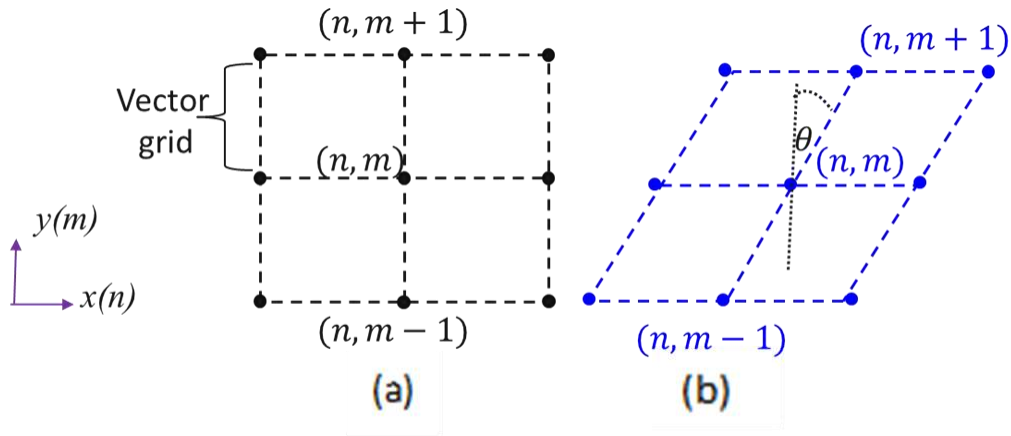
Figure 4.10: Schematic representation for the grid to calculate the shear strain, (a) initial configuration, (b) post-deformation.
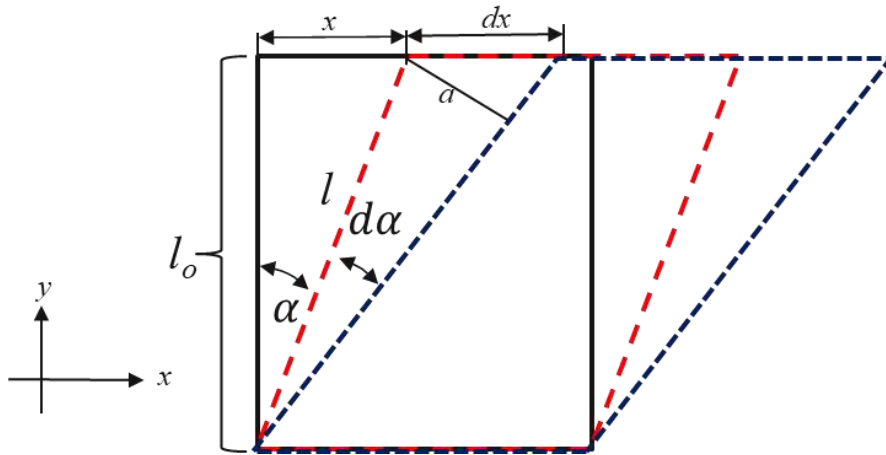
Figure 4.11: Illustrating the shear strain deformation.

4.2.4.2 *True strain and Engineering strain*

At this point a clarification between the engineering shear strain, which is $\tan(\theta)$, and the true shear strain (θ) is required.

As shown in Pardis et al.(2017), the true shear strain can be obtained as follows: assume the black box in Figure 4.11 has been deformed through simple shear to the red frame with shear angle, α, before it

experiences an infinitesimal shear angle deformation, $d\alpha$, which has transformed it to the dark blue frame, as shown in Figure 4.11. Based on this description, the engineering shear strain, γ, is:

$$\gamma = \tan(d\alpha) = \frac{a}{l} \cong \frac{dx\cos(\alpha)}{l} = \frac{l_o}{l_o^2 + x^2}dx \qquad 4.6$$

Mathematically, the true strain, γ_t, can be obtained through the integration of the engineering strain, so

$$\gamma_t = \int_0^x \frac{l_o}{l_o^2 + x^2}dx = \tan^{-1}\left(\frac{x}{l_o}\right) = \alpha \qquad 4.7$$

Based on Equations 4.6 and 4.7, the engineering shear strain, γ, has been identified as tan (shear angle) and the true shear strain, γ_t, is the shear angle.
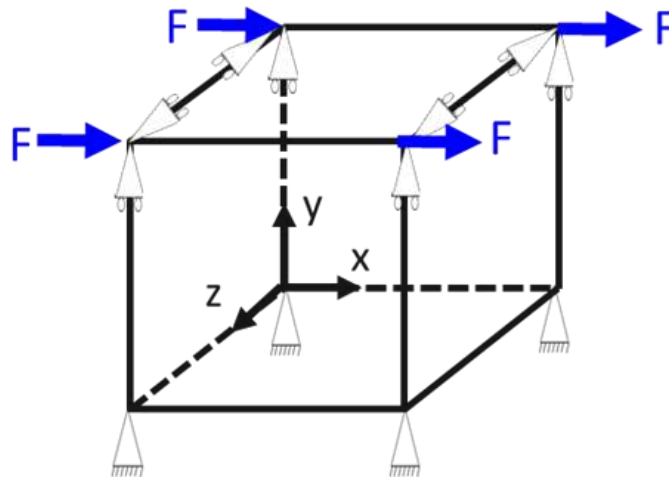
Figure 4.12: a 3D one-element model to study the simple shear calculations in Abaqus.

4.2.4.3 Finite Element Strain Measurement

The shear strain calculations from Abaqus in the XY plane are presented as NE12, which is the nominal shear, strain in the XY (1-2) plane, and LE12, the logarithmic shear strain in the XY (1-2) plane. For simple shear a one-element C3D8 model has been created in Abaqus, as shown in Figure 4.12, to study the strain for simple shear cases. Here, the bottom surface of the model in Figure 4.12 is constrained in all directions, and a displacement is applied on the upper surface in the positive X direction, while constrained in the Y and Z directions.

The results from this analysis are shown in Figure 4.13(a). Figure 4.13(b) is a 2D schematic diagram for the model. It is concluded that at ($\theta \leq 20°$), the values for θ, tan(θ), nominal strain (NE12) and log strain (LE12) are almost identical. However, as this research is carried out at $\theta > 30°$ (the aim of this research is to develop a FE model, which simulate the P91 at a high deformation level, at $\theta > 30°$), further study is required for the shear strain measures.
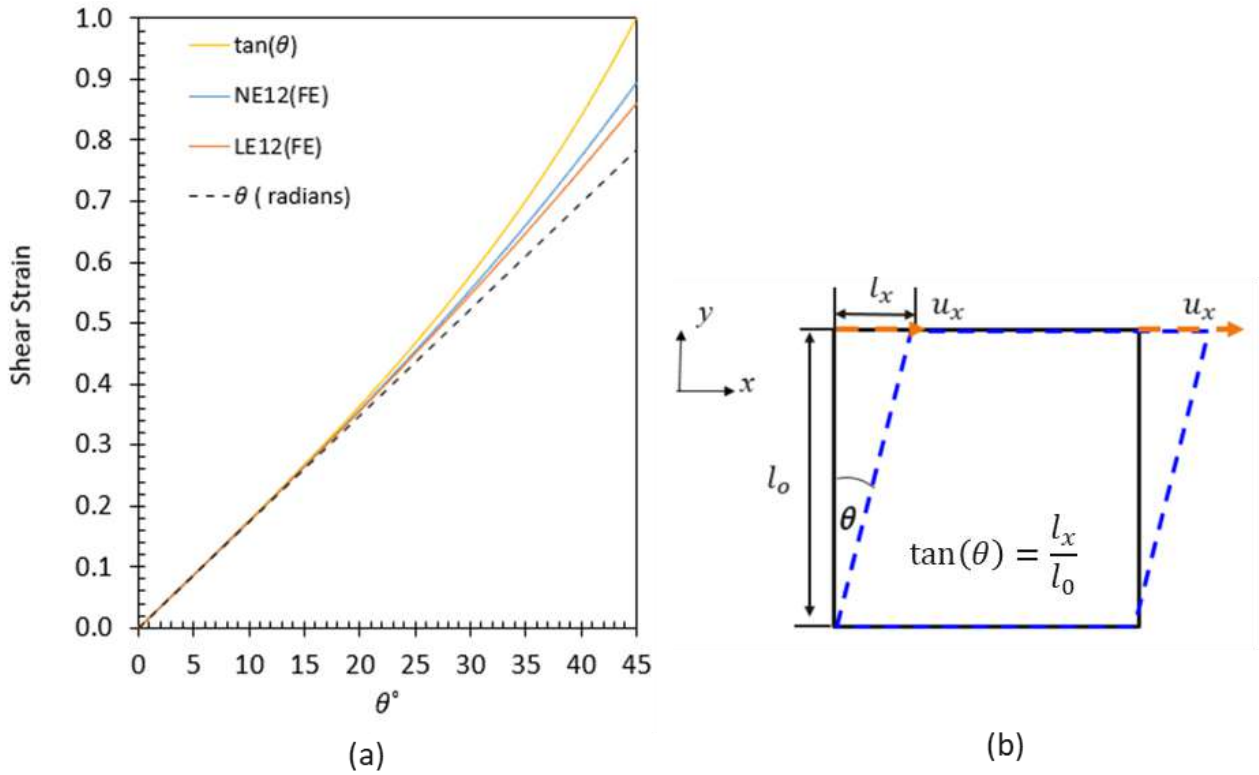
Figure 4.13: (a) Relation between different shear strain measures in Abaqus, and (b) representation of simple shear.
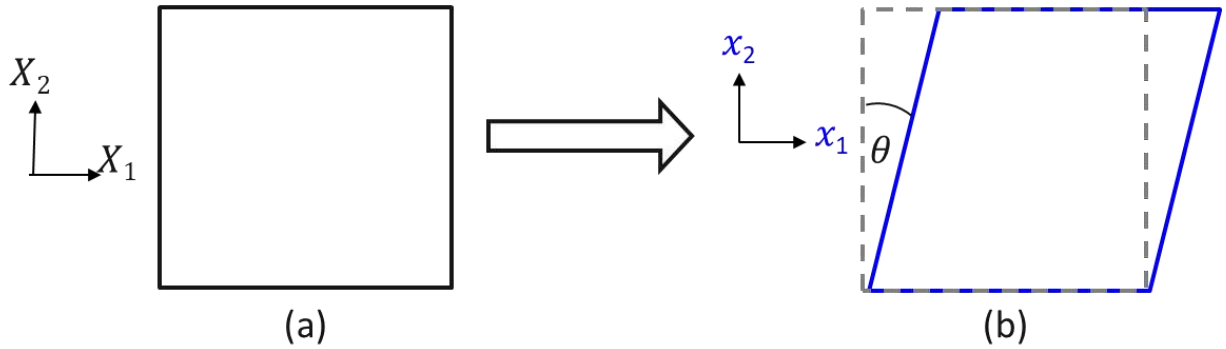
Figure 4.14: Simple shear deformation diagram, (a) initial reference configuration, defined in X_1, X_2 coordinates, and (b) current (deformed) configuration, defined in x_1, x_2 coordinates.

Based on the Abaqus theory manual (Simulia, 2013) the nominal strain tensor (Biot strain), $\boldsymbol{\varepsilon}^N$, is :

$$\boldsymbol{\varepsilon}^N = \sqrt{\mathbf{F} \cdot \mathbf{F}^T} - \mathbf{I} \tag{4.8}$$

Where $\mathbf{F}$ is the deformation gradient, $\mathbf{F}^T$ is the transpose of the deformation gradient, and $\mathbf{I}$ is the identity matrix. NE12 is the summation of the off-diagonal terms of the nominal strain matrix ($\boldsymbol{\varepsilon}^N$). The logarithmic shear strain tensor (Hencky strain), $\boldsymbol{\varepsilon}^L$, is:

$$\boldsymbol{\varepsilon}^L = \ln\sqrt{\mathbf{F} \cdot \mathbf{F}^T} \tag{4.9}$$

LE12 is the summation of the off-diagonal terms of the logarithmic shear strain tensor ($\boldsymbol{\varepsilon}^L$).

38

For simple shear, the initial and deformed configurations are shown in Figure 4.14. The deformed configuration coordinates can be related to the initial reference coordinates through:

$$x_1 = X_1 + X_2 \tan(\theta)$$
$$x_2 = X_2$$

4.10

Thus, under simple shear, the deformation gradient matrix $\mathbf{F}$ is:

$$\mathbf{F} = \begin{bmatrix} 1 & \tan(\theta) \\ 0 & 1 \end{bmatrix}$$

4.11

The left Cauchy-Green deformation tensor $\mathbf{B} = \mathbf{F}\mathbf{F}^{\mathrm{T}}$ is:

$$\mathbf{B} = \begin{bmatrix} 1 + \tan^2(\theta) & \tan(\theta) \\ \tan(\theta) & 1 \end{bmatrix}$$

4.12

By substituting Equation 4.12 into Equation 4.8, the nominal shear strain is:

$$\varepsilon^{\mathrm{N}} = \sqrt{\begin{bmatrix} 1 + \tan^2(\theta) & \tan(\theta) \\ \tan(\theta) & 1 \end{bmatrix}} - \mathbf{I}$$

4.13

To obtain the square root of a 2×2 matrix, the Cayley-Hamilton Theorem (Gordon, 2007) is used. If $\mathbf{X}$ is the square roots of matrix $\mathbf{A}$, as follows,

$$\mathbf{X}^2 = \mathbf{A}$$

4.14

Solving for $\mathbf{X}$,

$$\mathbf{X} = \frac{\zeta_2}{\sqrt{\mathrm{tr}(\mathbf{A}) + 2\zeta_1\sqrt{\det(\mathbf{A})}}} \left(\mathbf{A} + \zeta_1\sqrt{\det(\mathbf{A})}\mathbf{I} \right)$$

4.15

Where "det" is the determinant of the matrix, and "tr" is the trace. The constants $\zeta_1 = \pm 1$ and $\zeta_2 = \pm 1$, shows that solving for $\mathbf{X}$ leads to four solutions. The first and the second solution with $\zeta_1 = -1$ and $\zeta_2 = \pm 1$ are,

$$\sqrt{\mathbf{B}} = \pm \begin{bmatrix} 0 & 1 \\ 1 & \tan(\theta) \end{bmatrix}$$

4.16

The solutions for $\sqrt{\mathbf{B}}$ from Equation 4.16 are meaningless as the shear strain is constant (i.e., ± 2) regardless of the value θ. The third and fourth solutions where : $\zeta_1 = +1$ and $\zeta_2 = \pm 1$ is,

$$\sqrt{\mathbf{B}} = \pm \begin{bmatrix} \dfrac{2 + \tan^2\theta}{\sqrt{4 + \tan^2\theta}} & \dfrac{\tan\theta}{\sqrt{4 + \tan^2\theta}} \\ \dfrac{\tan\theta}{\sqrt{4 + \tan^2\theta}} & \dfrac{2}{\sqrt{4 + \tan^2\theta}} \end{bmatrix}$$

4.17

As displacement and shear angle are defined in the + X direction the positive square root of $\sqrt{B}$, so the positive solution of Equation 4.17 is the appropriate solution. Substituting Equation 4.17 into Equation 4.13, the nominal strain matrix is:

$$\boldsymbol{\varepsilon^N} = \sqrt{B} - I = \begin{bmatrix} \dfrac{2 + \tan^2 \theta}{\sqrt{4 + \tan^2 \theta}} - 1 & \dfrac{\tan \theta}{\sqrt{4 + \tan^2 \theta}} \\ \dfrac{\tan \theta}{\sqrt{4 + \tan^2 \theta}} & \dfrac{2}{\sqrt{4 + \tan^2 \theta}} - 1 \end{bmatrix} \qquad 4.18$$

The nominal shear strain ($NE12 = \varepsilon_{12}^N + \varepsilon_{21}^N$) is then:

$$NE12 = \frac{2 \tan \theta}{\sqrt{4 + \tan^2 \theta}} \qquad 4.19$$

Also, for known NE12, the shear angle can be calculated by inverting Eq. 4.19 as follows:

$$\theta = \tan^{-1} \sqrt{\frac{1}{\left(\frac{1}{NE12}\right)^2 - \left(\frac{1}{2}\right)^2}} \qquad 4.20$$

The derived solution for the nominal strain matrix ($\boldsymbol{\varepsilon^N}$) Equation 4.18, is verified through the
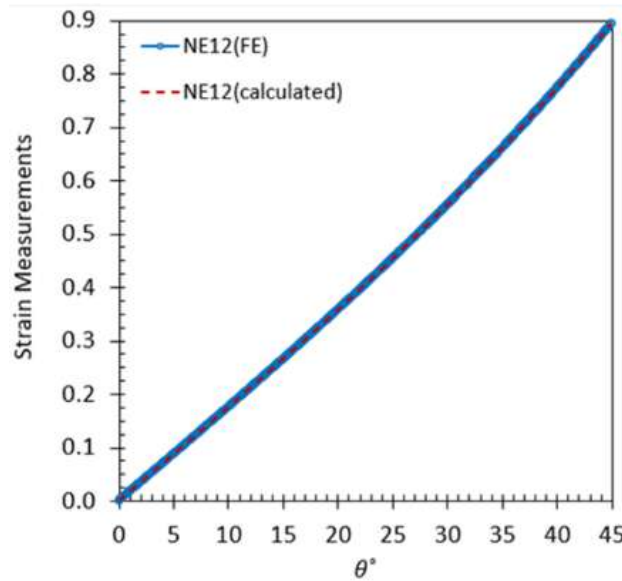
Figure 4.15: verifying the solution for the nominal strain ($\boldsymbol{\varepsilon^N}$) Equations 4.19.

Abaqus model for simple shear by plotting the results from Abaqus in comparison to the results from Equation 4.18. This verification is shown in Figure 4.15, which indicates identical values for the results reported by Abaqus and that calculated using Equation 4.18. As the shear angle can be determined from the nominal strain matrix ($\boldsymbol{\varepsilon^N}$), it is sufficient when correlating the FE results using Abaqus with the DIC calculations.

4.2.5 Validating the Strain Results at the Gauge Region

Based on the derivations in Section 4.2.4, the FE shear strain results and the experimental DIC results are compared in Figure 4.16, where the shear strain is $\gamma = \tan(\theta)$. These results show good agreement between FE and the experiment results with an average difference of approximately 12%.
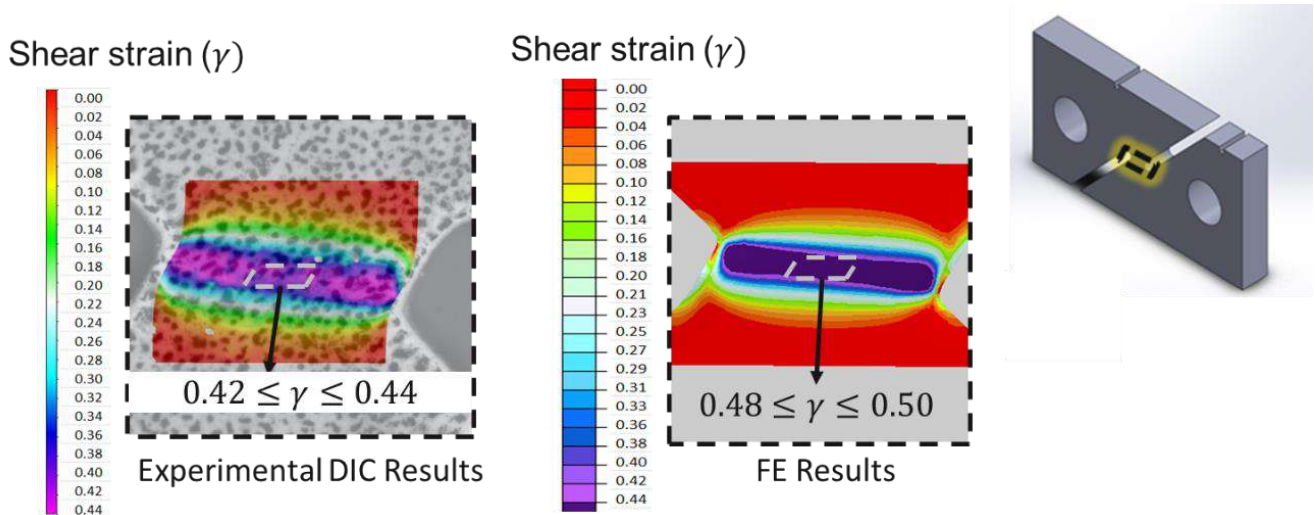
Figure 4.16: The comparison between FE shear strain results and Experimental shear strain results at the gauge region, this area is highlighted on the shear specimen on the right.
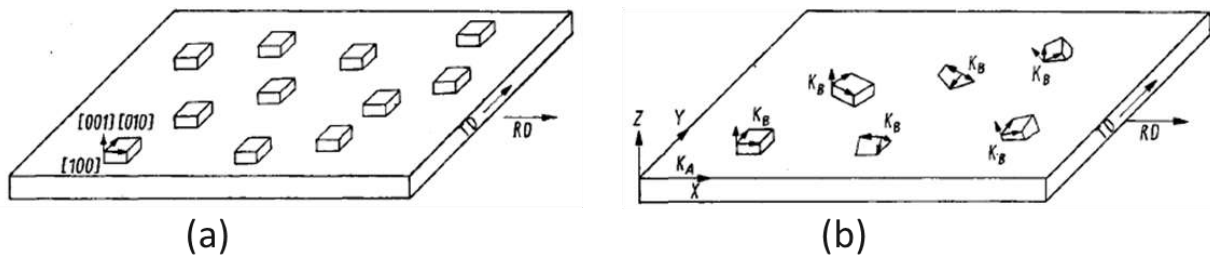
Figure 4.17: The Crystals' orientation with respect to the specimen, (a) the crystals have the same orientations as the specimen, (b) each crystal has a different orientation with respect to the specimen (H.-J. Bunge, 1982).
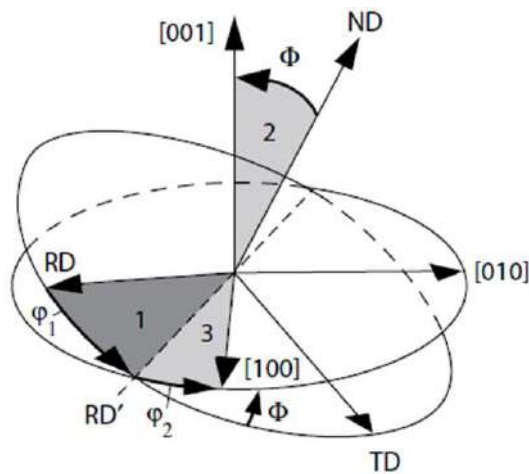
Figure 4.18: Diagram showing how rotation through the Euler angles φ_1, ϕ, φ_2, in order 1, 2, 3 as shown describes the rotation between the specimen and crystal axes (Engler & Randle, 2009).

4.3 Representation and Modelling of Crystallographic Orientation

The crystals' orientation, which refers to how the atomic planes in a volume of crystals are positioned with respect to the fixed coordinate system, as shown in Figure 4.17 (H.-J. Bunge, 1982), is crucial for studying the polycrystalline material properties as well as validating the CPFE models. As the focus of this research is modelling the P91 deformation at multiple length scales, the study of crystallographic orientation will be limited only to the validation of the CPFE results. Thus, this section is constructed as follows: the first sub-section discusses in detail the definition and representation of crystal orientations; the second sub-section focuses on the CPFE modelling, and the last sub-section shows the validation of the CPFE model based on comparing the numerical results with experimental (EBSD) scan results.

4.3.1 Representation of Crystallographic Orientation

4.3.1.1 Euler Angles

Euler angles describe the sequence of rotations which represent the orientation of the crystal with respect to a fixed coordinate system, or in other words, the Euler angles transform the specimen coordinates system to the crystal coordinates system (Engler & Randle, 2009). The terminology ND (normal direction), RD (rolling direction) and TD (transverse direction) see Figure 4.18, are used in the literature to identify the specimen axes. The three rotations, shown in Figure 4.18 (Engler & Randle, 2009), are described as follows:

i.   The rotation with angle φ_1 around the ND (normal direction), which transforms the RD (rolling direction) to RD' and TD (transverse direction) to TD', as shown in Figure 4.19 (a). ND and ND' are the same as the rotation is around this axis.

ii. The rotation with angle ϕ around the RD' (normal direction), which transforms the ND (normal direction) to ND'' and TD' to TD'', as shown in Figure 4.19 (b). RD' and RD'' are the same as the rotation is around this axis.

iii. The rotation with angle φ_2 around the ND'', which transforms the RD'' to RD''' and TD'' to TD''', as shown in Figure 4.19 (c). ND'' and ND''' are the same as the rotation is around this axis.

The crystal orientation can be defined based on these three rotations with respect to the specimen coordinate system using the rotation matrix ($\mathbf{R}$) as follows:

$$\mathbf{C_s} = \mathbf{R}\mathbf{C_c} \qquad 4.21$$

where $\mathbf{C_c}$ and $\mathbf{C_s}$ are the crystal coordinate system and specimen coordinate system, respectively.

The rotation matrix $\mathbf{R}$, is:

$$\begin{bmatrix} \cos\varphi_1 \cos\varphi_2 - \cos\phi \sin\varphi_1 \sin\varphi_2 & -\cos\varphi_1 \sin\varphi_2 - \cos\phi \cos\varphi_2 \sin\varphi_1 & \sin\varphi_1 \sin\phi \\ \cos\varphi_2 \sin\varphi_1 + \cos\varphi_1 \cos\phi \sin\varphi_2 & \cos\varphi_1 \cos\phi \cos\varphi_2 - \sin\varphi_1 \sin\varphi_2 & -\cos\varphi_1 \sin\phi \\ \sin\phi \sin\varphi_2 & \cos\varphi_2 \sin\phi & \cos\phi \end{bmatrix} \qquad 4.22$$
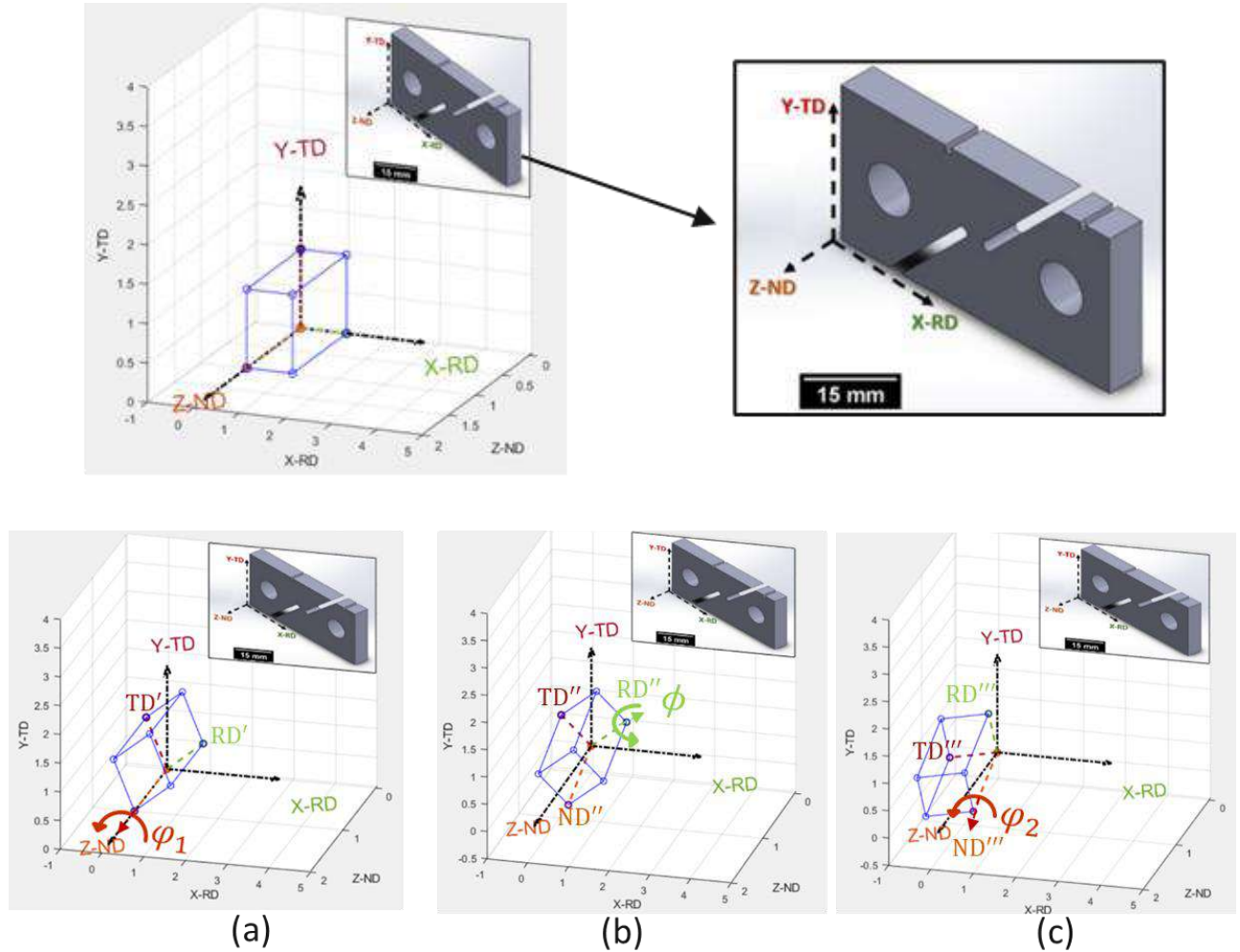
Figure 4.19: The sequence of rotations to describe the crystal's orientation using Euler angles, (a) is the first rotation, $\varphi_1 = 30$, around the crystal's Z-direction, (b) is the second rotation around the current crystal's X-direction, $\phi = 20$, and (c) is the third rotation, $\varphi_2 = 60$, around the current crystal's Z-direction.

An example of crystal rotation using the rotation matrix ($\mathbf{R}$) is shown in Figure 4.19. A random set of Euler angles $\varphi_1 = 30$, $\phi = 20$ and $\varphi_2 = 60$ have been used to illustrate the rotation of a crystal (with this orientation) into the specimen coordinate system. These plots have been created using MATLAB.

4.3.1.2 Misorientation Angle

It is useful to define a misorientation angle, ω, which is the change in orientation angle between two material points. The misorientation angle is defined as the smallest rotation angle among equivalent rotations relating two given orientations of the objects when the rotation is along a specified axis

(Engler & Randle, 2009), as shown in Figure 4.20. Thus, the rotation axis and the misorientation angle can be calculated based on Equation 4.22, as discussed in (Engler & Randle, 2009) Section 2.7. Thus, a misorientation angle can be used to assess quantitatively the change between the initial orientation and final orientation of individual blocks and will be used as a validation of the CPFE model by comparing initial and final EBSD scans with the results of the finite element model prediction.
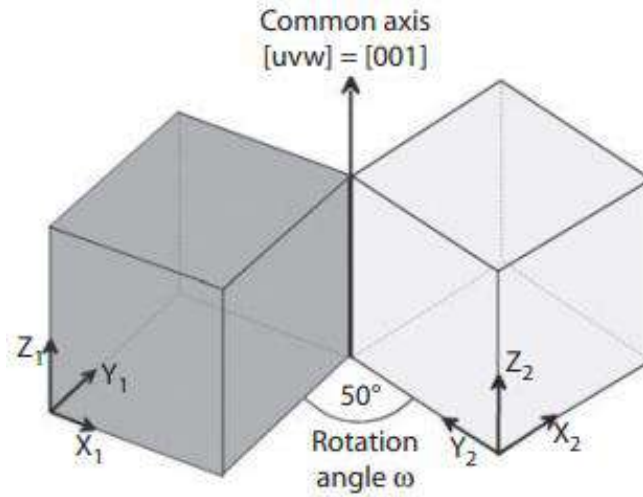
Figure 4.20: The misorientation angle between two crystals (Engler & Randle, 2009)*.*
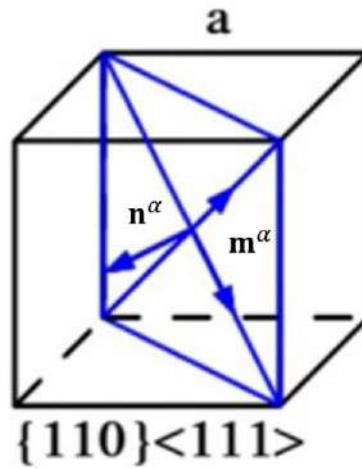
Figure 4.21: The BCC 12 {110}<111> slip systems (Phan, 2014). $\mathbf{m}^{\alpha}, \mathbf{n}^{\alpha}$ are the slip direction and the normal on slip plane for slip system (α), a is the length of the atomic BCC cube. These systems are described in Table 4.1*.*

4.3.2   Crystal Plasticity Finite Element Modelling

The CPFE model has been implemented as a UMAT subroutine in the finite element solver Abaqus and used to model the realistic three-dimensional shear deformation. This UMAT was originally developed in the work by Busso et al. (2000). The current model is based on the slip of the twelve BCC {110}<111> slip systems as shown in Table 4.1 and Figure 4.21. It is assumed that these 12 slip systems are sufficient to model the microstructure deformation of P91, as these are the dominant deformation mode at room temperature (M. Li et al., 2018; Meade, 2020), although the martensite P91 has also another two types

of slip systems, twelve of {112}<111> slip systems, and 24 of {123}<111> slip systems. The results of the orientation evolution will be examined in the next section in relation to the experimental EBSD data.

Table 4.1: The 12 BCC {110}<111> slip systems. $\mathbf{m}^{\alpha}$, $\mathbf{n}^{\alpha}$ are the slip direction and the normal on slip plane for the slip system (α). These systems are illustrated i in Figure 4.21.

$\alpha = 1$		$\alpha = 2$		$\alpha = 3$		$\alpha = 4$	
$\mathbf{n}^1\sqrt{2}$	(110)	$\mathbf{n}^2\sqrt{2}$	(110)	$\mathbf{n}^3\sqrt{2}$	(1-10)	$\mathbf{n}^4\sqrt{2}$	(1-10)
$\mathbf{m}^1\sqrt{3}$	[-111]	$\mathbf{m}^2\sqrt{3}$	[1-11]	$\mathbf{m}^3\sqrt{3}$	[111]	$\mathbf{m}^4\sqrt{3}$	[11-1]
$\alpha = 5$		$\alpha = 6$		$\alpha = 7$		$\alpha = 8$	
$\mathbf{n}^5\sqrt{2}$	(101)	$\mathbf{n}^6\sqrt{2}$	(101)	$\mathbf{n}^7\sqrt{2}$	(10-1)	$\mathbf{n}^8\sqrt{2}$	(10-1)
$\mathbf{m}^5\sqrt{3}$	[11-1]	$\mathbf{m}^6\sqrt{3}$	[-111]	$\mathbf{m}^7\sqrt{3}$	[111]	$\mathbf{m}^8\sqrt{3}$	[1-11]
$\alpha = 9$		$\alpha = 10$		$\alpha = 11$		$\alpha = 12$	
$\mathbf{n}^9\sqrt{2}$	(011)	$\mathbf{n}^{10}\sqrt{2}$	(011)	$\mathbf{n}^{11}\sqrt{2}$	(01-1)	$\mathbf{n}^{12}\sqrt{2}$	(01-1)
$\mathbf{m}^9\sqrt{3}$	[11-1]	$\mathbf{m}^{10}\sqrt{3}$	[1-11]	$\mathbf{m}^{11}\sqrt{3}$	[111]	$\mathbf{m}^{12}\sqrt{3}$	[-111]

The deformation of a crystal is modelled through the multiplicative decomposition of the deformation gradient $\mathbf{F} = \mathbf{F}^e . \mathbf{F}^p$. Here $\mathbf{F}^p$ represents the flow/slip of material through crystal lattice via dislocation motion, while $\mathbf{F}^e$ represents the elastic stretch and rotation of the material with the lattice (R. J. Asaro, 1983) with a description of this process shown in Figure 4.22. The slip system model for crystal plasticity, which describes the plastic slip as illustrated in Figure 4.22, is modelled based on the Asaro & Rice (1977) model for plastic slip. This model is based on assuming that the plastic velocity gradient $\mathbf{L}^p$ depends linearly on the crystallographic slip rate,

$$\mathbf{L}^p = \dot{\mathbf{F}}^p(\mathbf{F}^p)^{-1} = \sum_{\alpha=1}^{N} \dot{\gamma}^\alpha \, \mathbf{m}^\alpha \otimes \mathbf{n}^\alpha \qquad 4.23$$

where $\mathbf{F}^p$ represents the plastic deformation gradient, $\mathbf{m}^\alpha$, $\mathbf{n}^\alpha$ are the slip direction and normal on slip plane α, and $\dot{\gamma}^\alpha$ is the slip rate. This summation is over all the slip systems shown in Table 4.1. The accumulated equivalent plastic strain is defined as,

$$\varepsilon_{eq} = \int_0^t \left(\frac{2}{3}\mathbf{D}^p : \mathbf{D}^p\right)^{\frac{1}{2}} d\tau \qquad 4.24$$

where $\mathbf{D}^p$ is the plastic strain rate defined as,

$$\mathbf{D}^p = \frac{1}{2}\sum_{\alpha=1}^{N} \dot{\gamma}^\alpha \left[\mathbf{F}^e\mathbf{m}^\alpha \otimes \mathbf{n}^\alpha(\mathbf{F}^e)^{-1} + (\mathbf{F}^e)^{-\mathrm{T}}\mathbf{n}^\alpha \otimes \mathbf{m}^\alpha(\mathbf{F}^e)^{\mathrm{T}}\right] \qquad 4.25$$

Slip on these systems is modelled using the flow rule developed by Busso et al.(2000),

$$\dot{\gamma}^\alpha = \dot{\gamma}_o \exp\left\{-\frac{F_o}{kT}\left|1-\left\langle\left\langle\frac{|\tau^\alpha|-S^\alpha\frac{\mu}{\mu_o}}{\hat{\tau}_o\frac{\mu}{\mu_o}}\right\rangle\right\rangle^p\right|^q\right\}\mathrm{sgn}(\tau^\alpha), \qquad \langle x\rangle = \begin{cases}x & x>0 \\ 0 & x\leq 0\end{cases} \qquad 4.26$$

where for slip system α, S^α is the total slip resistance, τ^α is the resolved shear stress and $\frac{\mu}{\mu_o}$ is the ratio of the shear modulus at the study temperature to that at zero K to reduce all elastic interactions to zero K, T is the absolute temperature and k is the Boltzmann constant. The constants associated with the slip system family are F_o the total free energy required to overcome the lattice resistance, $\hat{\tau}_o$ the lattice friction stress at zero K, p, q and $\dot{\gamma}_o$ are the exponential constants and exponents.

The constitutive model is represented using the second Piola-Kirchoff stress, $\mathbf{S}$, and elastic Green tensor, $\mathbf{E}^e$;

$$\mathbf{S} = \mathbf{C}:\mathbf{E}^e \qquad\qquad 4.27$$

where $\mathbf{C}$ is the elastic stiffness, and

$$\mathbf{E}^e = \frac{1}{2}[\mathbf{F}^{e\mathrm{T}}\mathbf{F}^e - \mathbf{I}] \qquad\qquad 4.31$$

The second Piola-Kirchhoff stress tensor $\mathbf{S}$ is related to the Cauchy stress tensor, $\boldsymbol{\sigma}$, via

$$\mathbf{S} = \mathbf{F}^{e^{-\mathrm{T}}}[\det(\mathbf{F}^e)\boldsymbol{\sigma}\mathbf{F}^{e^{-\mathrm{T}}}] \qquad\qquad 4.28$$

4.3.3   Crystal Plasticity Finite Element Results

An isotropic model is used for the macroscopic FE-simulation using Abaqus (as in Section 4.2). The displacement field from one element of the macroscopic model has been transferred to the microscopic model using the sub-model method, as illustrated schematically in Figure 4.23. The microscopic model is based on the crystal plasticity model which has been implemented using UMAT in Abaqus. The pre-deformation experimental EBSD data was used to determine the crystal orientation of each microscale element. The microscale model consists of 1289 grains (crystals) with a total square area $\approx$ 100 μm $\times$ 100 μm with 250,498 C3D8 elements in Abaqus representing the same number of pixels as in the EBSD scan. The martensite grains have been identified from EBSD scans as those with boundaries having misorientations above 15 degrees (Dudko et al., 2013; Panait et al., 2010).

The microstructure study will be done using the MATLAB package MTEX (Bachmann et al., 2010) in three steps (see Figure 4.24). The first step is to study the whole RVE using an inverse pole figure (IPF) map. This step of the microstructure analysis aims at checking the quality of EBSD scans achieved using the shear specimen and getting an overall idea about the reorientation of the crystals through tracking individual grains. However, this step is of low accuracy, due to the difficulty in locating the individual

grains efficiently. Also, due to reorientation of the microstructure during deformation (see also the modelling work of Meade et al. (2021) the grain (block) boundaries in the deformed microstructure do not always align with those in the initial microstructure. That renders the tracking process difficult and not of significantly high accuracy.
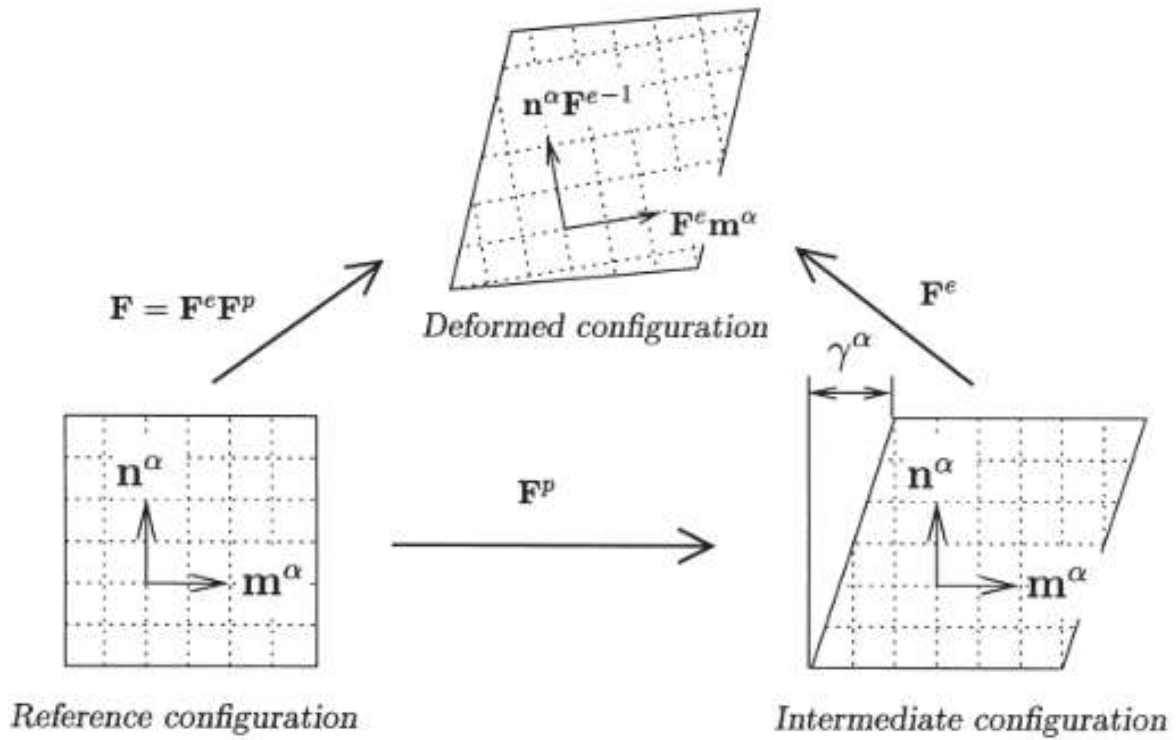
Figure 4.22: The kinematics of elastic-plastic deformation of slip system, α (Meissonnier et al., 2001)*.*
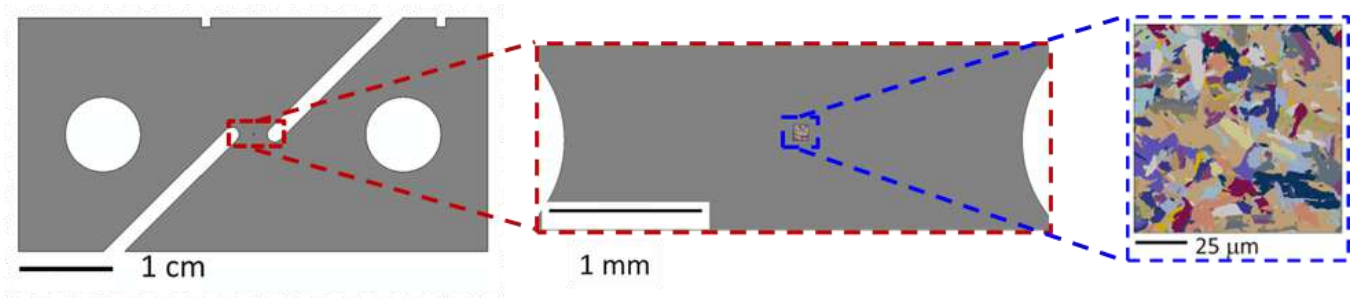
Figure 4.23: Multi-scale Finite Element Model.

The refinement mechanism for P91, which undergoes severe plastic deformation (during cold working), is difficult to confirm experimentally, due to its complex hierarchical microstructure (Song et al., 2019). In Song et al., 2013, it is stated that grain refinement for grade 91 steels is a dislocation-dominant process where, for example, misorientations increase steadily with increasing strain (as discussed in Hughes & Hansen, 1997, see Figure 4.25).

Whole Map ➡ Three Regions ➡ Multiple Grains
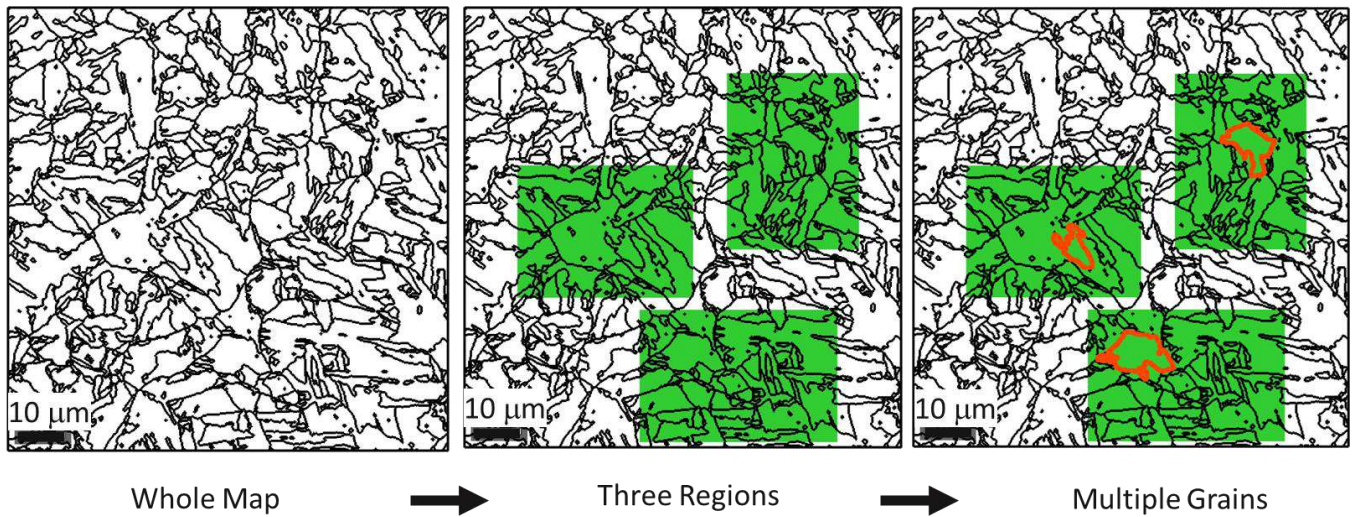
Figure 4.24: Microstructure study plan showing the three steps of the microstructure analysis.
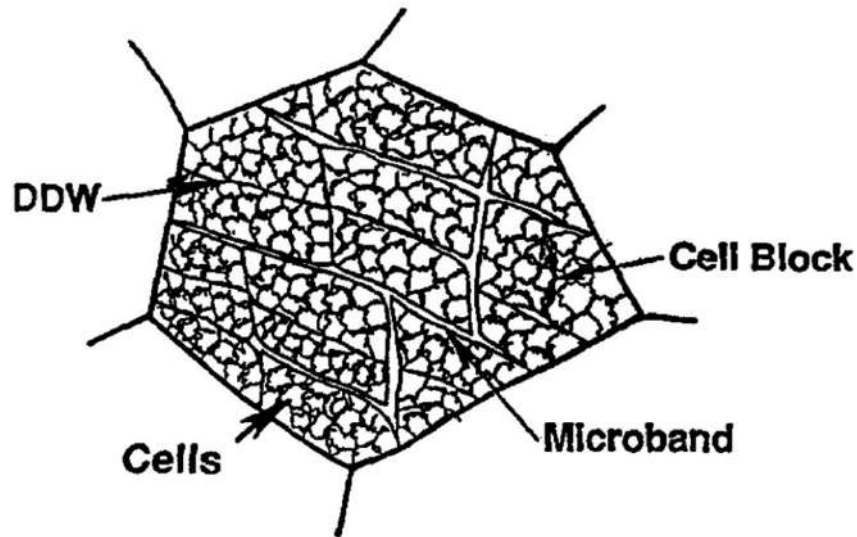
Figure 4.25: A representation of deformation microstructures and grain subdivision. Small to medium strain deformation, von Mises strain = 0.06-0.80 with long microbands and dense dislocation walls (DDW) surrounding groups of cells in cell blocks (Hughes & Hansen, 1997).

Therefore, a deeper means of analysis with higher accuracy is required, which will be achieved in the second step. This second step of the microstructure analysis aims to efficiently study the direction of a crystal's reorientation projected in two directions: the loading direction (LD)[3], and the transverse direction (TD), by studying three regions which account for almost 40% of the area of the whole map. Also, the analysis in this step provides a more quantitative comparison between the experimental results and the CPFE model. Finally, in step three the misorientation angle, ω, (see Section 4.3.1.2) has

---

[3] The loading direction (LD) in the current work is equivalent to the rolling direction (RD), commonly used in the literature, as the current deformation process is not driven by rolling but by applying load/displacement in the LD to induce shear deformation.

been used to assess quantitatively the change between the initial orientation and final orientation of randomly selected blocks in the three regions. This third step aims at a deeper numerical quantitative comparison between the experimental results and the CPFE results.

4.3.3.1   Microstructure Study Step 1

In this study, two IPF maps have been used to capture the change in crystal orientation. Figure 4.26 and Figure 4.27 provide the inverse pole figure (IPF) maps in the loading direction and transverse direction, respectively. In both figures, the initial measured EBSD scan is shown in the centre, the measured experimental EBSD scan is on the left and the predicted EBSD scan at the same level of shear strain is on the right. The large shear strain experienced in the region of interest, 40% is noted. As seen in Figure 4.26 and Figure 4.27, the study of the whole EBSD map has shown qualitatively similar results between the simulation and the experiments.

Figure 4.26 and Figure 4.27 are important to show that the experimental results are of high quality - high indexing of the EBSD scan (224885 indexed pixels of Fe-BCC (89%)) - for the current study, given the high deformation (shear strain approximately 40%). This proves that the designed specimen is suitable for microstructure studies where the EBSD scan is needed, that is because of the insignificant out-of-plane deformation at high strain levels. This out-of-plane deformation at high strains makes it almost impossible to achieve high indexing EBSD scans, (Meade, 2020). The out-of-plane deformation using a compact tension specimen is shown in Figure 4.28 compared to the current results. This is the main reason behind the development of the shear specimen for the current research study.

In step one, five blocks have been randomly identified (the blocks in black circles in Figure 4.26 and Figure 4.27) for further analysis. For the analysis in the loading direction, Figure 4.26, the blocks reoriented mainly towards either $[\bar{1}11]$ or $[001]$. For the analysis in the transverse direction, shown in Figure 4.27, which is perpendicular to the loading direction, the blocks reoriented mainly toward either $[011]$ or $[001]$. This analysis shows qualitative agreement between the experimental results and the CPFE.

4.3.3.2   Microstructure Study Step 2

As shown in Figure 4.29, three regions of the EBSD scan have been selected for further analysis. The IPF plots of these three regions are presented in Figure 4.30 in the loading direction. It may be noted that in step one, an inverse pole figure map has been used (Figure 4.26 and Figure 4.27), whereas in this step an inverse pole figure plot (Figure 4.30) has been used. In the former, the crystal orientation has been understood from its colour in the map and the corresponding colour shown in the inverse pole figure colour coding of the orientation map, while in the latter the inverse pole figure plot shows the

intensity of crystals projected in all directions, as the scale bar shown on the left side of Figure 4.30 represents the intensity of crystal orientations projected in all directions. The use of the inverse pole figure plot is important to provide a quantitative comparison between the experimental and simulation results.
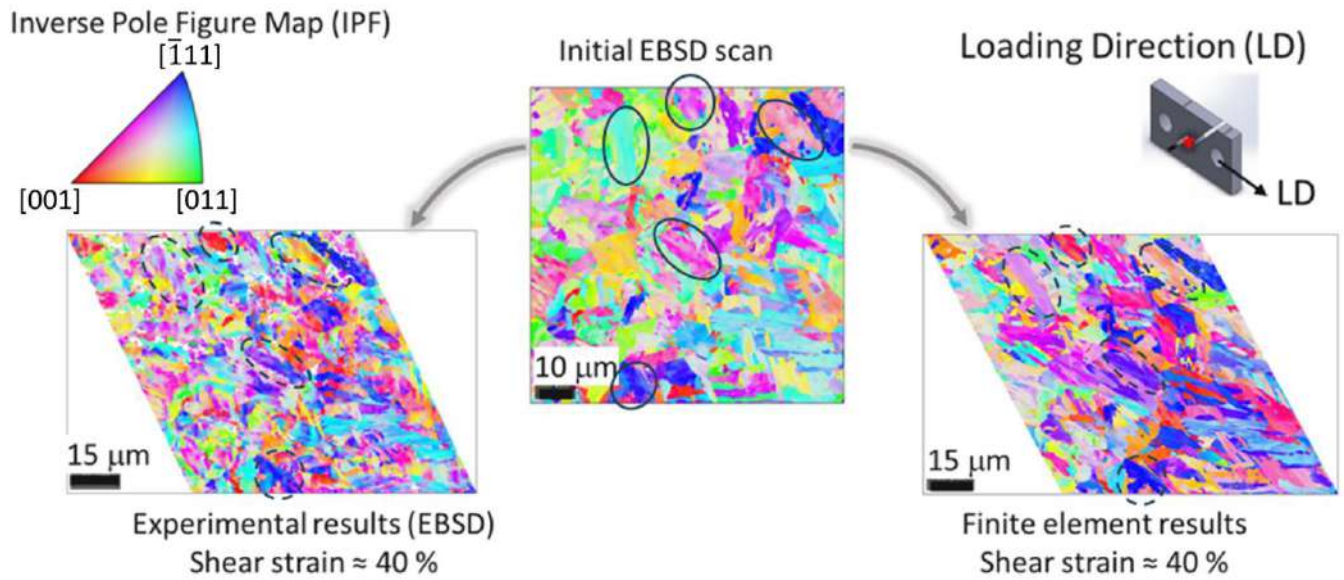
Figure 4.26: Analysis of the crystals reorientation post-deformation using IPF Map in Loading Direction (LD).
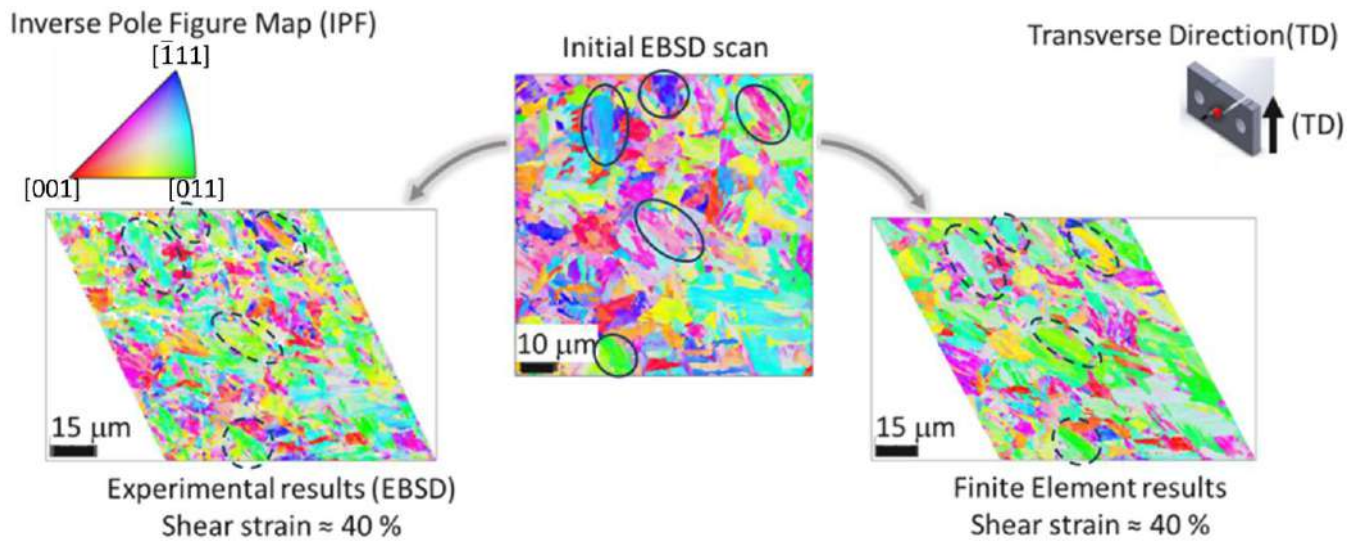
Figure 4.27: Analysis of the crystals reorientation post-deformation using IPF Map in transverse Direction (TD).

In this figure, the crystals have shown reorientation towards the [$\bar{1}$11], and [001] directions with a preference toward the [$\bar{1}$11] direction. A description of crystal re-orientation in this direction is presented in Appendix A.
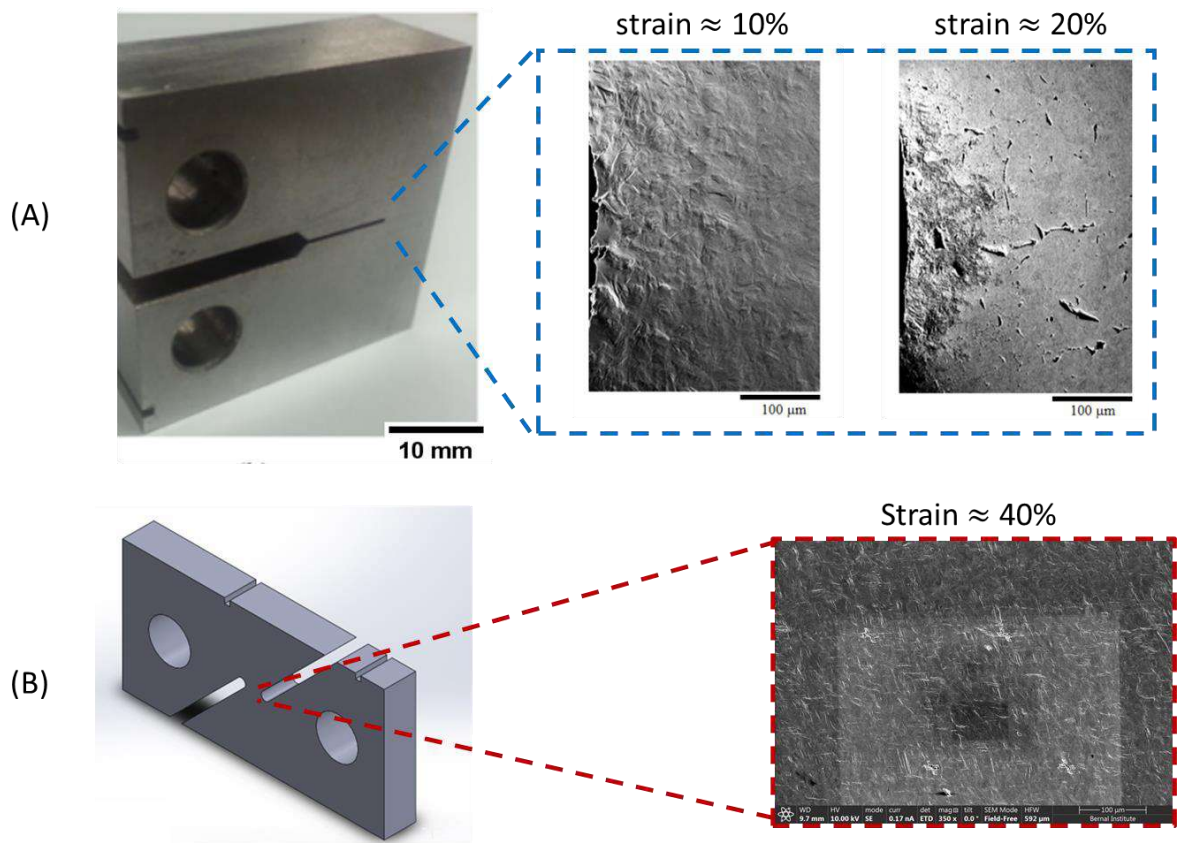
Figure 4.28: SEM images of the deformed surface of the post-test notch specimen adjacent to the notch root for compact tension test (A) (Meade, 2020), and (B) the deformation at gauge region for shear test.
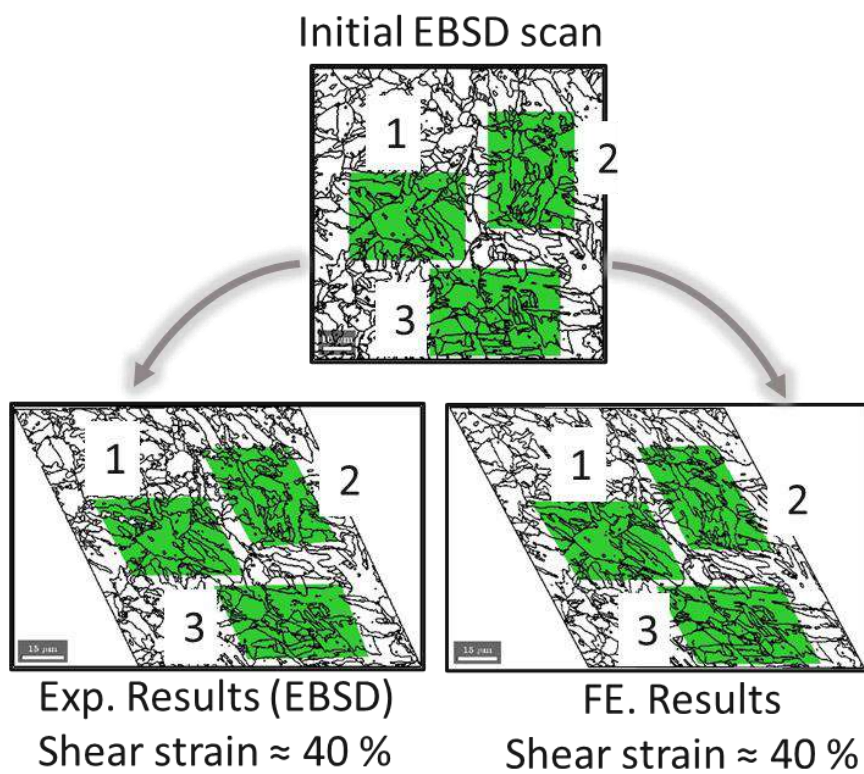
Figure 4.29: Three regions have been identified randomly for a detailed quantitative study using IPF plots, as shown in Figure 4.30 and Figure 4.31.
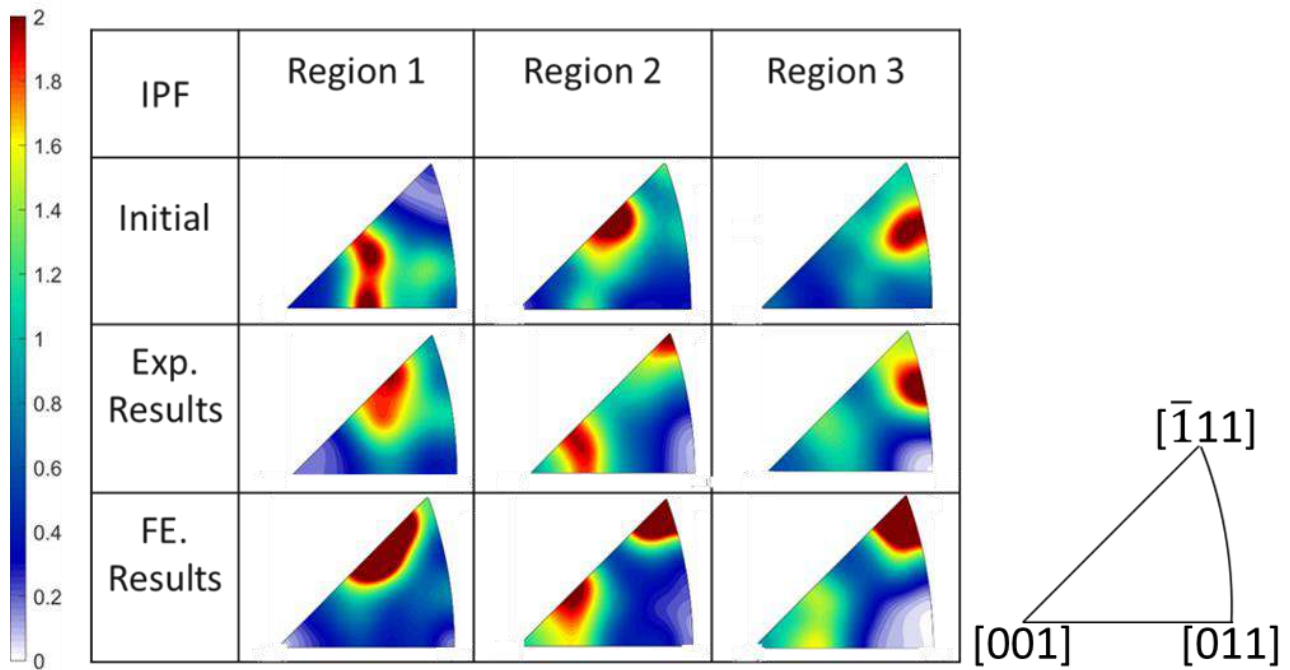
Figure 4.30: Study the reorientation of the crystals post-deformation using an IPF plot for the three randomly selected regions in Loading Direction (LD).

The analysis in the transverse direction is presented in **Figure 4.31**. In this figure, the crystals have shown reorientation towards the [011] and [001] directions with a preference toward the [011] direction.
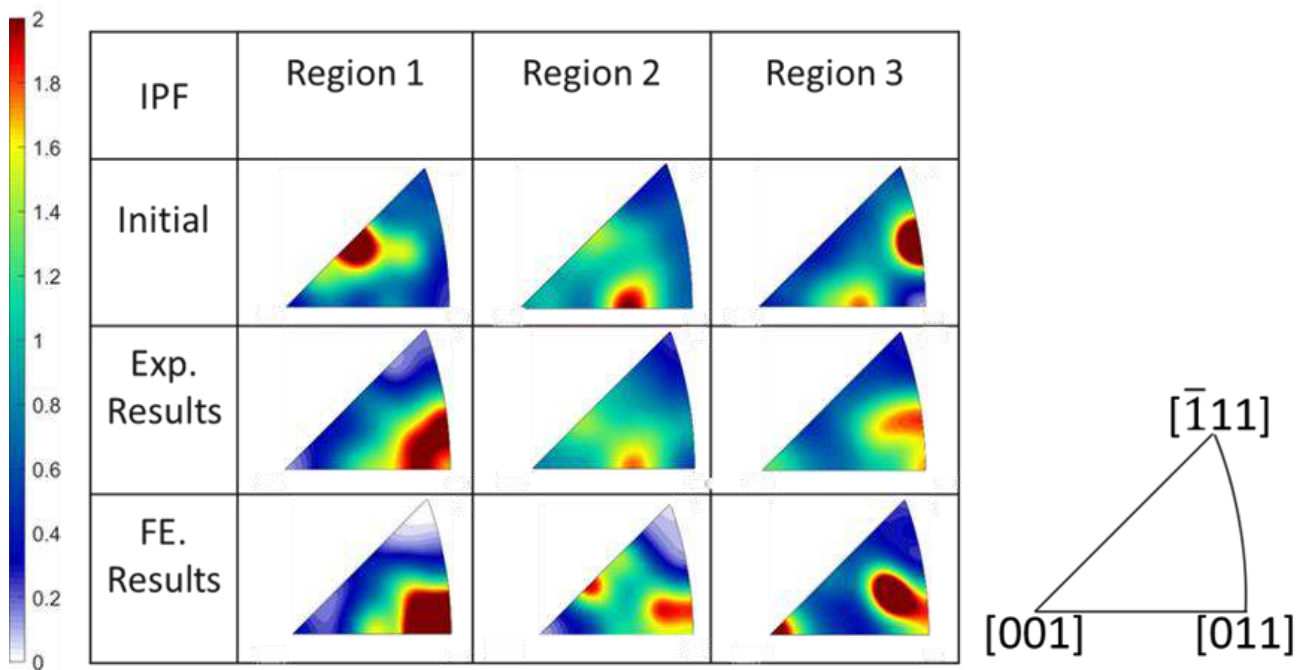
Figure 4.31: Study the reorientation of the crystals post-deformation using an IPF plot for the three randomly selected regions in the Transverse Direction (TD).

Both the CPFE and experimental results have shown the same trends in crystal reorientation. However, the CPFE results are overestimating the reorientation results. This agreement between the CPFE and the experimental results is higher in region one and region two than in region three. This point will be clarified in the third step of the study which is concerned with the misorientation angle.
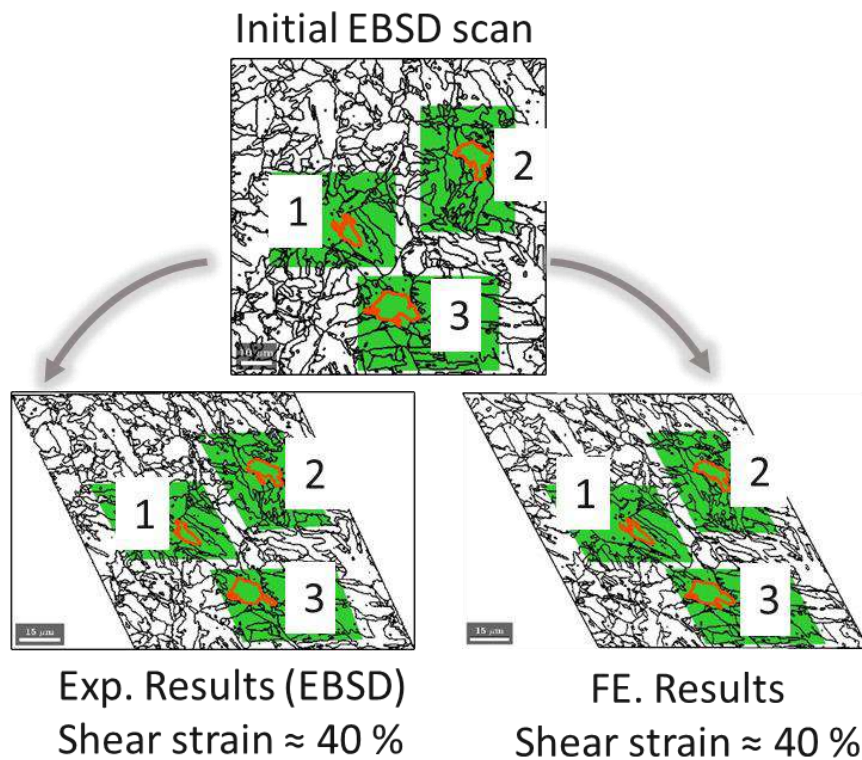
Figure 4.32: Three randomly selected grains for the quantitative study.

4.3.3.3   Microstructure study Step 3

In step 3 of the microstructure study, three blocks were randomly selected, one from each region, as shown in Figure 4.32, and the results for the misorientation angle between the initial orientation and final orientation for CPFE results and experimental results are shown in Table 4.2.

Table 4.2: The misorientation angle for three randomly selected grains between the initial orientation and final orientation.

Misorientation angle (°)	Grain 1	Grain 2	Grain 3
Experiment	10.5	12.0	2.35
FE. model	13.2	13.5	10.06
Difference	26%	12%	326%

From Table 4.2 the simulation results for crystals reorientation have shown poor agreement with the experimental results in grain 3 while showing good agreement in grain 1 and grain 2. The reason for the difference in agreement is difficult to determine. For example, it may be because the orientation of the material beneath the surface has been ignored. EBSD is a surface measurement and provides no information about orientations sub-surface. In our FE analysis, we have assumed that the orientation is uniform through the thickness of the submodel region (Meade et al., 2018b). Several researchers have worked on understanding and developing methodologies to address this issue. In Zhang et al. (2018) a double-layer CPFE model has been developed, where a randomly textured layer beneath the surface layer has been used. This has been found to have some effect on the texture evolution for the CPFE model. Another methodology to generate a realistic 3D microstructure based on 2D EBSD scans has been developed by St-Pierre et al. (2008). In this methodology, an experimental surface has been reproduced on the top of the 3D virtual microstructure, to respect the morphological and crystallographic textures obtained from an EBSD analysis. This methodology is suitable for simulating anisotropic microstructures and successfully reproduced twins; however, the calculations did not provide the exact locations of the slip bands. Thus, it has been proven that the grains beneath the surface have a strong influence on the strain field (St-Pierre et al., 2008). Another reason for the poor agreement between the FE results and the experimental results could be that only 12 slip systems have been considered during this study. Meade (2020) has concluded that the 12 slip systems {110} <111> are sufficient to model microscale deformation for P91. However, the study by Meade (2020) has been performed on low-strain deformation, without studying its applicability to high-strain deformation, as examined here. Recent work at the University of Limerick, using micropillar tests has indicated that additional slip system families may be active in Grade 91 steel (Rao, et al., 2023). Also, the effect of possible changes in the precipitate size due to coarsening ($M_{23}C_6$ carbides are the most important precipitates in tempered martensitic steel P91), during the deformation process, has not been considered. These precipitates are located at the lath boundaries, and precipitate coarsening during the deformation process may affect the strain hardening, (D. F. Li et al., 2014). If grain 3 had a higher concentration of $M_{23}C_6$ precipitates than grain 1 and grain 2, this may have had a greater effect on the deformation of grain 3, not accounted for in the model, and thus the model predictions for grain 3 would be less good than those for grain 1 and grain 2. These effects could be examined in future work.

4.4 Conclusion

A multiscale crystal plasticity-based finite element model to simulate P91 deformation has been developed. The model has been verified experimentally using multiple scales under large shear deformations.

The specimen used has been prepared from one side to be suitable for the EBSD scan, and from the other side to be suitable for the DIC measurements. Two notches at the top surface, and through the thickness of the specimen have been developed, to be suitable for the extensometer measurements. The FE model for the global scale deformation is based on the isotropic plasticity model while modelling the microstructure evolution is based on the crystal plasticity model. The FE model for the microstructure evolution is also based on the submodel technique in Abaqus, to deliver the displacement field from the global model to the submodel. Several assumptions have been made for this model, as the orientation of the crystals is uniform through the thickness, only the 12 slip systems {110} <111> are sufficient to model microscale deformation for P91, and the effect of the precipitates $M_{23}C_6$ have not been considered.

The result from the model shows relatively good agreement with the experimental results, where an extensometer is used to measure the global elongation (cm-scale), digital image correlation (DIC) is used to measure shear strains close to the notch (mm-scale) and EBSD is used to measure the deformation-induced crystal reorientation in the uniform strain region (μm-scale). However, studying the microstructure evolution using the current FE framework at high shear strain presented some drawbacks at some regions of the microstructure model, this will be investigated in future work.

Chapter 5: Life Prediction Tool for Grade 91 Steel

5.1 Introduction

Due to its excellent mechanical and thermal properties, steel P91 has been used in manufacturing of steam pipelines for thermal power generation plants. The creep life prediction of the key components is important for the long-term safe operation of the thermal power components (Wang et al., 2022). As a result, several studies have been conducted to study the life prediction of steel P91.

Creep is the tendency for a material to deform under constant stress at high temperatures over long times (Dieter, 1988). Creep is thus a temperature and time (rate) dependent phenomenon. The evolution of creep strain with time is represented by a creep curve, with creep at short times referred to as primary creep, with a varying strain rate, while secondary or steady-state creep has a constant strain rate at a particular stress (referred to as the steady state, or minimum creep rate). Creep is generally considered to be diffusion-controlled or dislocation-controlled and the relationship between creep strain rate and stress is often represented by a power law, with the power law exponent = 1 for diffusion-controlled creep and the exponent between 3 and 8 for dislocation-controlled creep. The temperature dependence of strain rate is generally represented through an Arrhenius-type rate equation of the form of Eq. 4.26.

Despite the superior creep resistance of steel Grade 91 at high temperatures, premature failures especially Type IV cracking, often occur in the heat affected zone (HAZ) of the welded components. This failure mode is preceded by strain localization in the HAZ (W. Zhang et al., 2020). For a given material, the failure under creep conditions, described as creep rupture, depends on time, stress, and temperature. Thus, correlation equations relating rupture time to stress, and temperature have been proposed, e.g., Oak Ridge National Laboratory (ORNL) model, Larson–Miller, Orr–Sherby–Dorn, Manson–Haferd, Monkman-Grant, Wilshire, and Wilshire-Cano-Stewart (WCS) (Abe, 2014; Cano & Stewart, 2021; Sundararajan, 1989; Wang et al., 2022). The models by Larson–Miller (LMP), Orr–Sherby–Dorn, and Manson–Haferd follow the master curve equation (Abe, 2014) of the form:

$$P = b_o + b_1(\log \sigma) + b_2(\log \sigma)^2 + \cdots + b_k(\log \sigma)^k + e_i \qquad 5.1$$

where σ is the stress, b_o, b_1, b_2, and b_k are the regression coefficients, k is the degree of the regression equation, and e_i is the error term. The parameter P depends on the model used. For the Larson–Miller model P is given by (Abe, 2014):

$$P_{LM} = (T + 273)(C_{LM} + \log t_r) \qquad 5.2$$

For the Orr–Sherby–Dorn model (Abe, 2014) P is given by:

$$P_{OSD} = \log t_r - (Q/2.3RT) \qquad 5.3$$

For the Manson–Haferd (Abe, 2014) P is given by:

$$P_{MH} = (\log t_r - \log t_a)/(T + 273 - T_a) \qquad 5.4$$

In Equations 5.2, 5.3 and 5.4, T is the temperature, t_r is time to rupture, t_a, C_{LM}, and T_a are constants, Q is the activation energy, and R is the gas constant. The ORNL model (Abe, 2014) which is similar to the LMP model is given by:

$$P_{LM} = (T + 273)(C_{LM} + \log t_r) = d_o + d_1 \log \sigma + d_2 \sigma \qquad 5.5$$

where d_o, d_1, and, d_2, are constants. This model could be combined with the LMP model (Abe, 2014), which gives:

$$P_{LM} = (T + 273)(C_{LM} + \log t_r) = a_o + a_1 \log \sigma + a_2 (\log \sigma)^2 + a_3 \sigma \qquad 5.6$$

where a_o, a_1, a_2, and a_3 are constants. The modified Monkman-Grant relationship (Sundararajan, 1989), relates the steady creep rate $\dot{e}_s$, time to fracture t_r, and the true strain at creep fracture e_f. It is given by:

$$\dot{e}_s t_f / e_f = C_{MMG} \qquad 5.7$$

where C_{MMG} is the modified Monkman-Grant constant. The Wilshire model is based on normalizing the applied stress by the ultimate tensile strength (UTS), σ_{TS}, value for each batch or heat treatment. This model is described by a sigmoidal relationship to correlate the normalized stress with the time to rupture, t_r, and it is given by (Cano & Stewart, 2021; Wang et al., 2022):

$$(\sigma/\sigma_{TS}) = \exp\{-k_1[t_r \exp(-Q_c^*/R(T + 273)]^u\} \qquad 5.8$$

This form can be transformed into a direct expression for t_r ;

$$t_r = [-\ln(\sigma/\sigma_{TS})/K_1]^{1/u}/[\exp(-Q_c^*/R(T + 273))] \qquad 5.9$$

For this model, the same description could be used to evaluate the minimum-creep-strain-rate, $\dot{\varepsilon}_{min}$, and it is given by (Cano & Stewart, 2021; Wang et al., 2022):

$$(\sigma/\sigma_{TS}) = \exp\{-k_1[\dot{\varepsilon}_{min} \exp(-Q_c^*/R(T + 273))]^v\} \qquad 5.10$$

Also, this form can be transformed into a direct expression for $\dot{\varepsilon}_{min}$;

$$\dot{\varepsilon}_{min} = [-\ln(\sigma/\sigma_{TS})/K_2]^{1/v}/[\exp(-Q_c^*/R(T + 273))] \qquad 5.11$$

where k_1, k_2, v and u are the Wilshire model material constants, and Q_c^* is the creep activation energy. Novel Wilshire-Cano-Stewart (WCS) relationships have been proposed by (Cano & Stewart, 2021; Wang et al., 2022) to predict the creep life of P91. This modified Wilshire model is a combination of the Wilshire model and Sinh model (based on the continuum damage mechanics (CDM) model) to predict

creep deformation, damage, and rupture of P91 steel under complex load. For the Sinh model the creep strain rate is given by (Cano & Stewart, 2021; Wang et al., 2022):

$$\dot{\varepsilon}_{cr} = A \, \sinh(\sigma/\sigma_{TS}) \times exp(\lambda\omega^{3/2}) \qquad\qquad 5.12$$

At minimum-creep-strain-rate, the damage parameter $\omega \approx 0$, thus Equations 5.11, and 5.12 could be combined to develop the WCS creep strain rate equation(Cano & Stewart, 2021; Wang et al., 2022);

$$\dot{\varepsilon}_{cr} = [-\ln(\sigma/\sigma_{TS})/K_2]^{1/v}/[exp(-Q_c^*/R(T+273))] \times exp(\lambda\omega) \qquad\qquad 5.13$$

The creep rupture time can be calculated from the integration of the damage evolution, which is given by (Cano & Stewart, 2021; Wang et al., 2022):

$$\dot{\omega} = [1 - exp(-\varphi)]/\varphi \times exp(-Q_c^*/R(T+273))/[-\ln(\sigma/\sigma_{TS})/K_1]^{1/u} \times exp(\varphi\omega) \qquad 5.14$$

where A, and σ_{TS}, are the minimum creep strain rate constants, ω is a dimensionless parameter to describe the damage, φ is the damage trajectory constant, and λ is a material constant. These relations are particularly important when extrapolating from short-term laboratory data (experimental duration is less than a year) to long-term plant conditions (more than 10 years).

Studying the residual stresses is also important for the life assessment of the welded sections in P91 pipes. In Yaghi et al. (2005) the residual stress modelling and the weld simulation have been examined using FE modelling. This study has shown that the peak tensile stress occurs at the inside surface of the pipe in the thin wall case and near the outside surface of the pipe in the thick wall case. Also, the results have clarified that for thick pipes the residual stress and hope stresses are generally independent of pipe diameter at the outside surface. Following the same approach of using the FE model to analyse and understand the creep evolution for Grade 91, W. Zhang et al. (2020) have developed a FE model to study the strain localization at the HAZ as a reason for premature failure of Grade 91 welded components. The effect of large grain size gradients has been considered by constructing a 2D digital microstructure based on actual microstructure using the Voronoi-tessellation method. The results successfully revealed the effect of pre-welding tempering on the evolution of strain localization in HAZ for creep resistance in steel weldments. Also, it is found that dislocation creep, diffusional creep and more importantly grain boundary sliding contribute synergistically to the creep strain accumulation in the HAZ.

Due to the start-up and shutdown cycles of power plants, the simultaneous damage arising from creep and fatigue should be considered. In Mroziński et al. (2022), samples manufactured from P91 steel have experienced conditions for creep and fatigue simultaneously at an elevated temperature of 600 °C. A linear approach has been used to combine the creep damage and fatigue damage through the

summation of both. In Harrison et al. (2016) a similar approach has been followed by creating a creep-fatigue damage calculation tool for welded P91. This tool has been created to monitor the damage induced in the power plant components to predict the component life. It is based on calculating the creep damage using Larson Miller equation and Robinson's rule. Fatigue damage fraction is evaluated using the rainflow cycle counting subroutine, the Smith-Watson-Topper fatigue parameter, and Miner's rule. The total damage has been calculated, and the results showed that an equal amount of damage for fatigue and creep has been generated in the plant component.

This chapter discusses the creation of a MATLAB app to serve as a computation life prediction tool for welded pipes manufactured from steel Grade 91. Life prediction is based on creep damage calculations, and this work is based on the Excel design tool developed by (Harrison et al., 2016a). This MATLAB app is developed to have a user-friendly GUI, higher feasibility to access operation data from external sources, and faster run time of more than 10 times faster than the Excel tool developed (Harrison et al., 2016a). That makes it useable for dynamic industrial applications, in which large data sets are being produced periodically and need to be imported as an external data source for the analysis tool. In this chapter, a description of the MATLAB app GUI is presented, followed by a description of the stress, and creep damage formulas used in creating this tool.
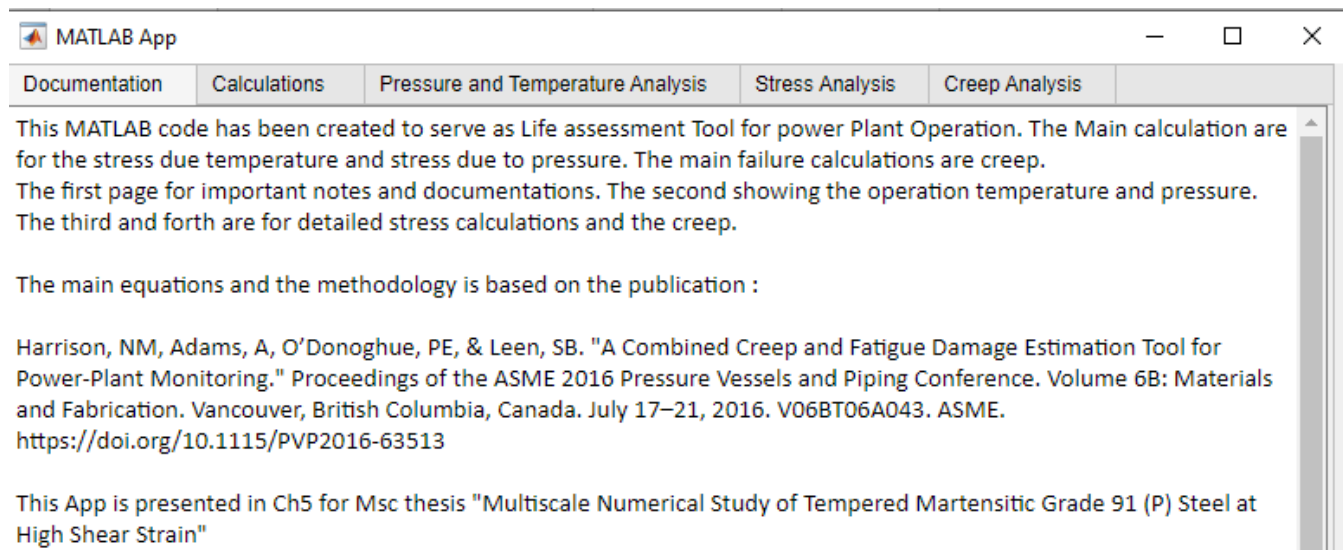
Figure 5.1: The MATLAB app GUI.

5.2   MATLAB app Graphical User Interface

This app, which follows the approach of Harrison et al. (2016b) consists of five main sections, as shown in Figure 5.1. The five sections are "Documentation," "Calculations," "Pressure and Temperature Analysis," "Stress Analysis "and "Creep Analysis." The inputs for this app are the operation pressure, temperature and corresponding time as shown in Figure 5.2. Also, the geometry and the material of the

pipe, are given in Table 5.1. These values for the material parameters are used at room temperature, as the stress calculations are based on the European Standard design code for shell and water-tube boilers, EN 12952-4-11 (Harrison et al., 2016b). These calculations aim to prevent unexpected early failure of the components, based on creep damage calculations. It may be noted that the material properties, such as Young's modulus, could vary significantly at high temperatures. For example, Young's modulus of P91 varies from 213 GPa at 20 °C to 141 GPa at 600 °C (Farragher et al., 2013). Based on EN 12952-1 (2001), Young's modulus should be used at the design temperature. In this study (as in Harrison et al. (2016b)) Young's modulus at room temperature will be used, as this is the maximum value, thus, the maximum possible thermal stress will be evaluated, and the predicted maximum damage will be calculated. Poisson's ratio can slightly increase from 0.29 to 0.32 at high temperature; however, it is commonly assumed to be constant at different temperatures (Batista Abreu et al., 2014).
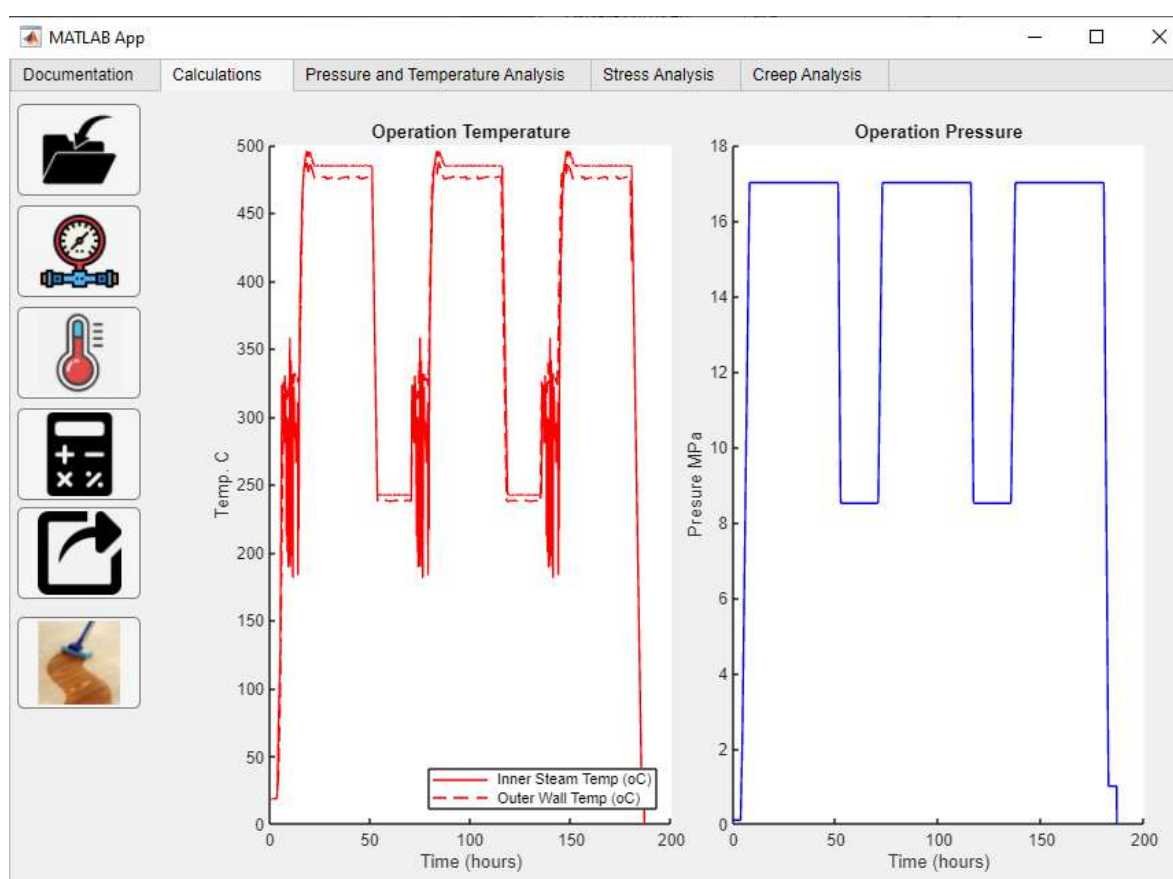
Figure 5.2: The section 'Calculation' is for Importing the data and performing the calculations. The plottings are for the operation temperature, where the steam temperature and wall temperature are plotted. Also, the operation pressure for the steam passing through the bore.

The first section "Documentation" Figure 5.1 contains the necessary information about this app, including the important references, equations, constants, all data required to be imported, results, etc. The second section is "Calculations", this section is mainly to plot the imported operating temperature and pressure, as shown in Figure 5.2, and to carry out all the calculations for stress and creep analysis. It

consists of six buttons. The description of the buttons is as follows, from top to bottom: the first is to import the text file containing operation pressure and temperature, the second is to plot the operating pressure, the third is to plot operating temperature, the fourth is to perform the calculations in terms of stress and creep analysis, the fifth is to export the analysis results to the MATLAB workspace, and the sixth button is to clear all plotting. The third section is "Pressure and Temperature Analysis," as shown in Figure 5.3. It is mainly to plot the wall temperature difference and the difference in pressure through the pipe wall. It consists of three buttons: the first button is for plotting the change in pressure, the second one is to plot the change in temperature, and the third one is to clear all plots.
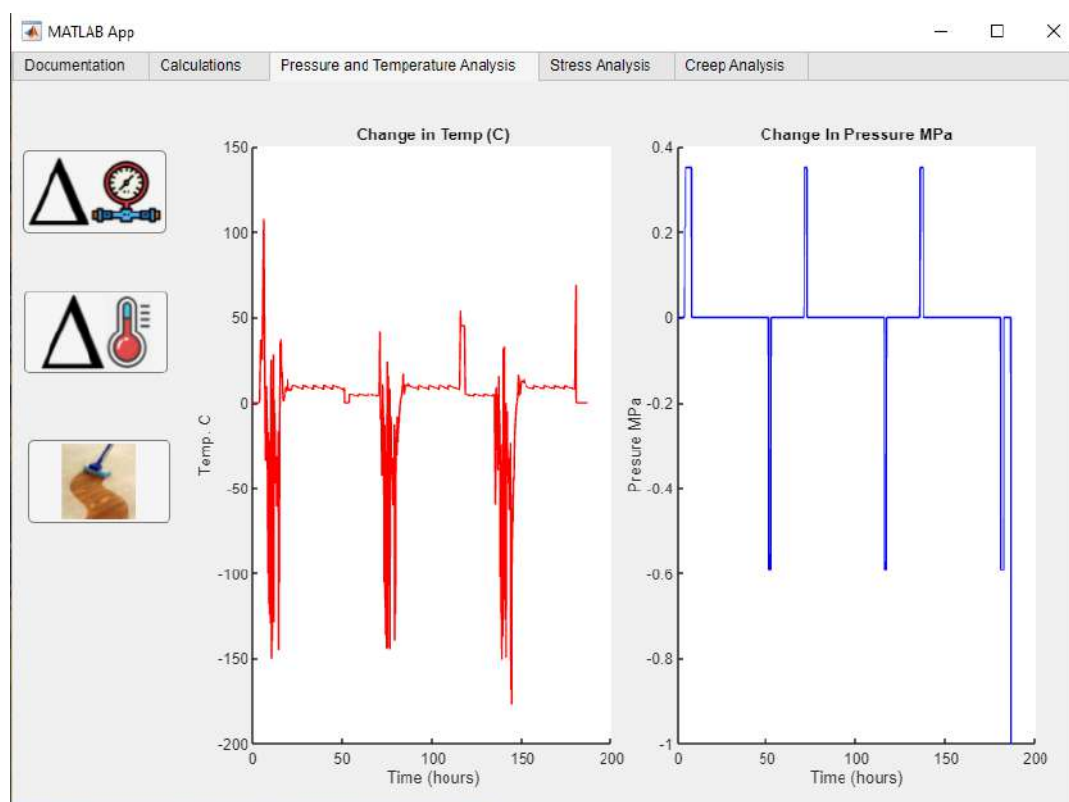
Figure 5.3: The section 'Pressure and Temperature Analysis' is for calculating the change in temperature, and the change in pressure. The change in temperature through the wall is the difference between the steam temperature and the wall temperature. The change in pressure is the change in steam pressure.

The fourth section "Stress Analysis ", is shown in Figure 5.4. It is to plot the stress due to pressure, the stress due to temperature and the total stress, which is the summation of both. This section consists of four buttons: the first button plots the stress due to pressure, the second button stress due to temperature, the third button total stress, and the fourth button clears all plots. The fifth section "Creep Analysis", Figure 5.5, is concerned with plotting total stress, sustained stress regions (where stress is constant), and accumulated creep damage fraction. It consists of four buttons: the first button is to plot total stress, the second button is to plot sustained stress regions, the third button is to plot the accumulated creep damage fraction, and the fourth button is to clear all plots.

5.3 Stress and Creep Damage Calculations

This section will discuss the calculation of total stress and accumulated creep damage fraction. The stress profile will be calculated based on the steam pressure and temperature; this stress will be used to calculate creep damage.
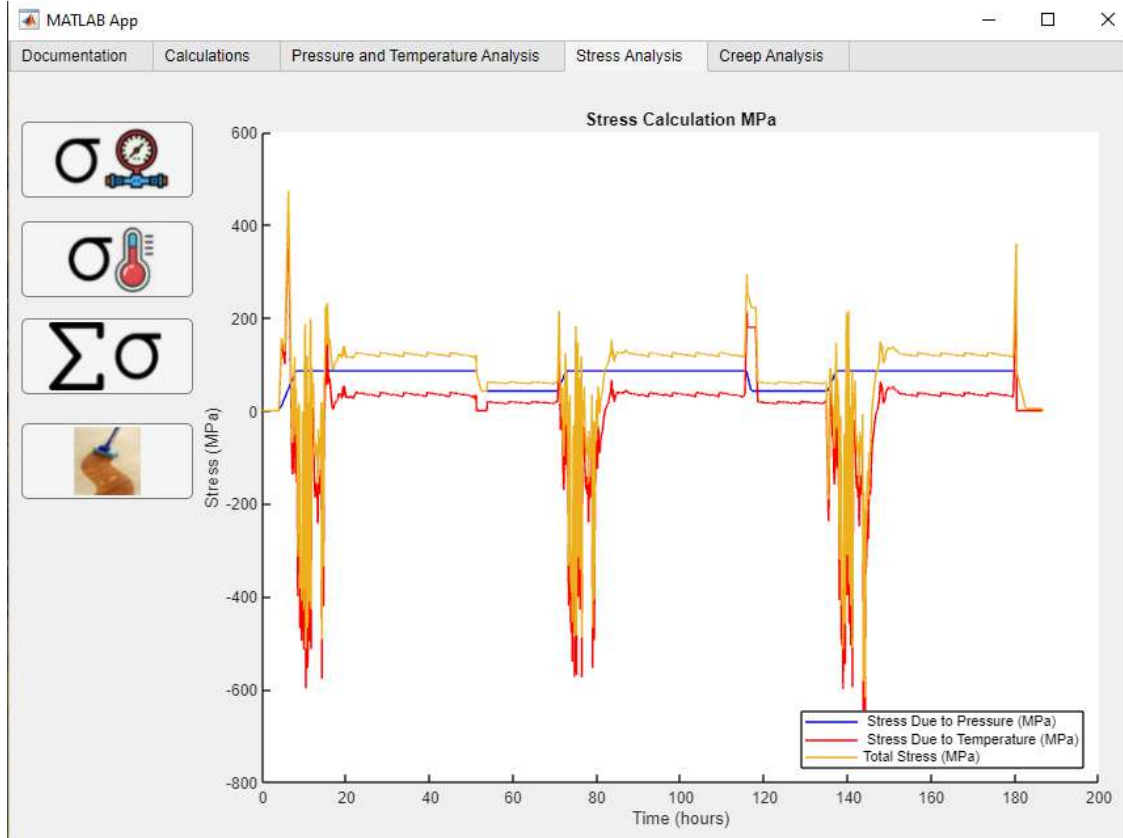
Figure 5.4: This section 'Stress Analysis', plots the stress due to temperature, pressure and the total stress. The stress due to pressure is based on Equation 5.1, the stress due to pressure is based on Equation 5.2, while the total stress is their sum, Equation 5.3.

5.3.1 Stress Calculation

The total stress calculation for a bore corner is based on calculating the thermal stress due to steam temperature (σ_T) and the mechanical stress due to steam pressure (σ_p). The thermal stress increment is calculated based on the changes in the wall temperature due to the change in the temperature of steam which flows through the bore, and it is calculated using Equation 5.15. The change in temperature through the wall is calculated based on the difference between the steam temperature and the outer wall temperature every five operation minutes. The temperature change, ΔT, used in Equation 5.16 is then the change in the 'through wall' temperature. The operation pressure and temperature have been obtained at five-minute intervals and the presented data and calculations are based on (Harrison et al., 2016b; EN 12952-4, 2011), where thermal shock events have not been taken into consideration. A different assessment method should be used for such abrupt changes in temperature, or accidents.

62

The mechanical stress increments due to the change in pressure (σ_p) is based on calculating the hoop mechanical stress Equation 5.17. The change in pressure is the change in steam pressure every five operating minutes. The total stress will be calculated from the summation of thermal stress and mechanical stress, Equation 5.18. The additional bending stress induced by the piping system is significant in calculating the total stress which leads to creep damage (Hald, 2017). This stress is related to the specific design of the power plant. In this case, FE simulation is required to estimate the value of this added system stress; for simplicity, this part will not be included in this work, and it could be suitable for future research.

The equation for calculating the thermal stress (Harrison et al., 2016b; EN 12952-4- 2011):

$$\sigma_T = \frac{\beta_{Lt} E}{1 - v} \Delta T \qquad\qquad 5.19$$

The equation for calculating the mechanical stress (Harrison et al., 2016b; EN 12952-4- 2011):

$$\sigma_p = \frac{\alpha_m D_{ms}}{2 E_{ms}} P \qquad\qquad 5.20$$

The equation for calculating the total stress:

$$\sigma = \sigma_T + \sigma_p \qquad\qquad 5.21$$

5.3.2 Creep Damage Fraction Calculation

The evaluation of creep damage rapture time is based on experimental data, where the specimen experiences constant stress at a specific temperature until rupture, where the creep rupture time (t_r) is the time to rupture, as shown in Figure 5.6. These experimental data are then fitted to mathematical formulas. Studies (Tabuchi & Takahashi, 2012a) have shown that the LMP model and ORNL model have insignificant differences in the creep rupture stresses at 100,000 hours. Also, the SEE (standard error of estimate) is nearly the same for both equations. Wang et al. (2022) have demonstrated that the WCS model has shown similar predictive capability as the LMP model for short-term creep behaviour, however, the advantage of the WCS model is its capability to be extrapolated to model long-term creep behaviour. Due to its wide application in industry and the simplicity of application (Abe, 2014), the second-order polynomial of the logarithmic stress for the LMP model will be used in this work to express the stress and temperature dependency of creep rupture time in this work (see also Tabuchi &

Takahashi, 2012). The second-order polynomial of the logarithmic stress for the LMP model following Equation 5.2 is given by:

$$(T + 273)(C + \log t_r) = a_o + a_1(\log \sigma) + a_2(\log \sigma)^2 \qquad \text{5.22}$$

The constants (C, a_o, a_1, a_2), (Tabuchi & Takahashi, 2012b) in Equation 5.23 have been calculated from the fitting of the experimental data as shown in Figure 5.6. Using the LMP is to estimate the time to rupture (t_r) for a pipe in a power plant, (σ) is total stress as given in Equation 5.24. Thus, if stress, σ, and temperature, T, are known, the time to rupture can be determined using Equation 5.25.
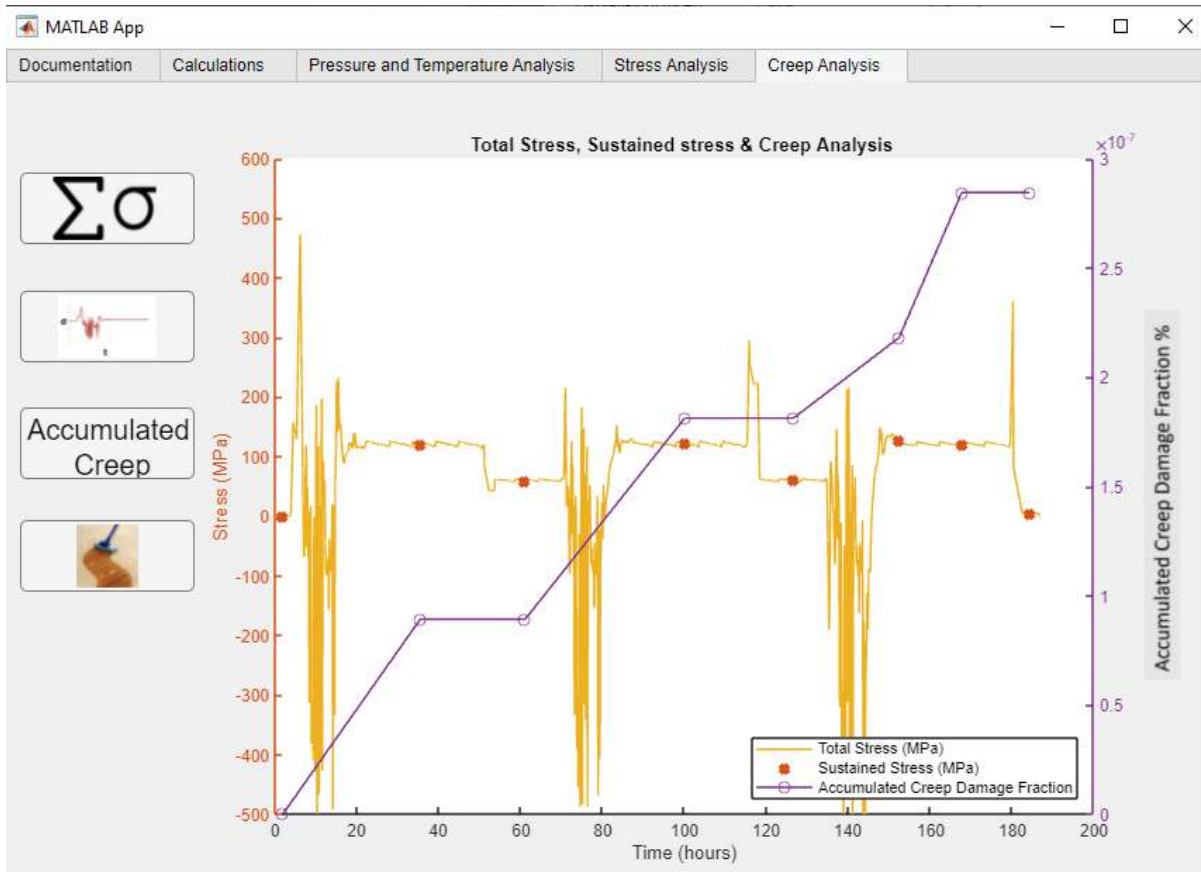
Figure 5.5: This section 'Creep Analysis', plots the total stress, the sustained stress region, and the accumulated creep damage fraction. The sustained stress regions are the regions where the stress fluctuation is 30 MPa, and the minimum limit for the time duration is 2 hr. The accumulated creep damage fraction is calculated based on Equations 5.4, and 5.6.

The stress calculated from operating power plant data has a variable profile as shown in Figure 5.4. For the LMP formula, the stress should be constant. Thus, sustained stress regions should be identified, as shown in Figure 5.5, where the fluctuation in stress in the specified sustained regions is 30 MPa, and the minimum limit for time duration for a sustained region is 2 hrs. These values have been chosen for this study to define the creep region, following the approach in Harrison et al. (2016). It should be mentioned, that for this case study, the sustained regions are all at temperatures below

500 °C. These sets of data are not included in the LMP experiments fitting Figure 5.6, and it is assumed that the fitting parameters are of good approximation for the current case study.

C=31.4, a_0=34154, a_1=3494, a_2=-2574, SEE=0.267
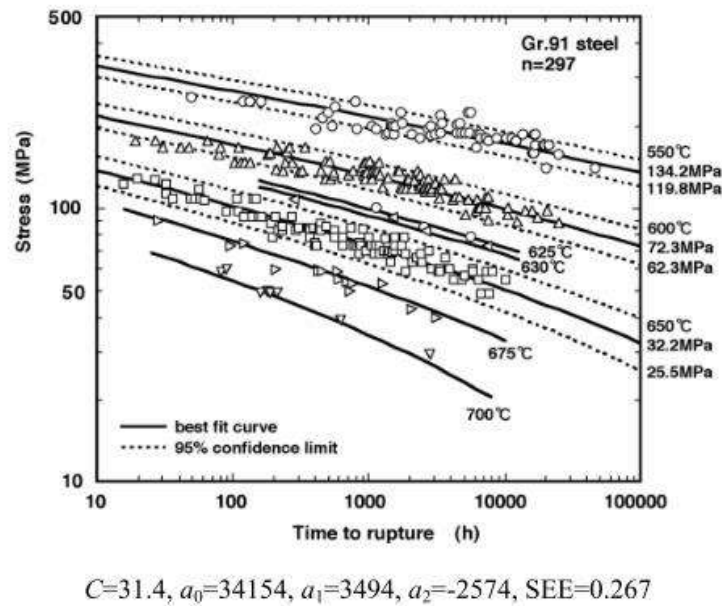
Figure 5.6: The fitting of creep rapture experiments for the welded joints steel grade 91 based on the LMP formula (Tabuchi & Takahashi, 2012).

Table 5.1: Material and Geometry constants for stress calculation[4]

Parameter	Definition	Value	Units
β_{Lt}	Coefficient of Linear Thermal Expansion	1.39E-05	K^{-1}
E	Elastic Modulus	200000	MPa
ν	Poisson's Ratio	0.3	-
α_m	Geometry-Based Stress Concentration Factor	1	-
D_{ms}	Internal Pipe Diameter	254	mm
E_{ms}	Wall Thickness	25	mm

The creep rupture time (t_r) calculated using the LMP formula is calculated at the stress and temperature points, which have been marked with a cross in Figure 5.5. Finally, the calculation of the accumulated

---

[4] These data have been provided by Dr Noel Harrison, Mechanical Engineering, University of Galway. These data have been used to develop the work in (Harrison et al., 2016b) and are included in the design tool developed in that work.

creep damage fraction is based on the Robinson linear creep damage rule (Šeruga et al., 2011), it also has been identified in (EN 12952-4-11) for calculating accumulated creep damage.

It is given by:

$$D_{\text{c}} = \sum_{i=0}^{n} \frac{\Delta t_{\text{i}}(\sigma_{\text{i}}, T_{\text{i}})}{t_{\text{ri}}(\sigma_{\text{i}}, T_{\text{i}})} \qquad 5.6$$

where n is the total number of sustained regions, (σ_i, T_i) are the median values of stress and temperature in the sustained region, i, Δt_{i}, is the duration of the sustained region in hours, t_{ri} is the rupture time in hours from the LMP formula for the corresponding values of (σ_i, T_i) in Equation 5.26, D_{c} is then the accumulated creep damage fraction so that when D_c = 1, creep rupture is predicted. As shown in Figure 5.5 the accumulated creep damage has been calculated at each sustained stress region and is summed to the values of the previous sustained regions.
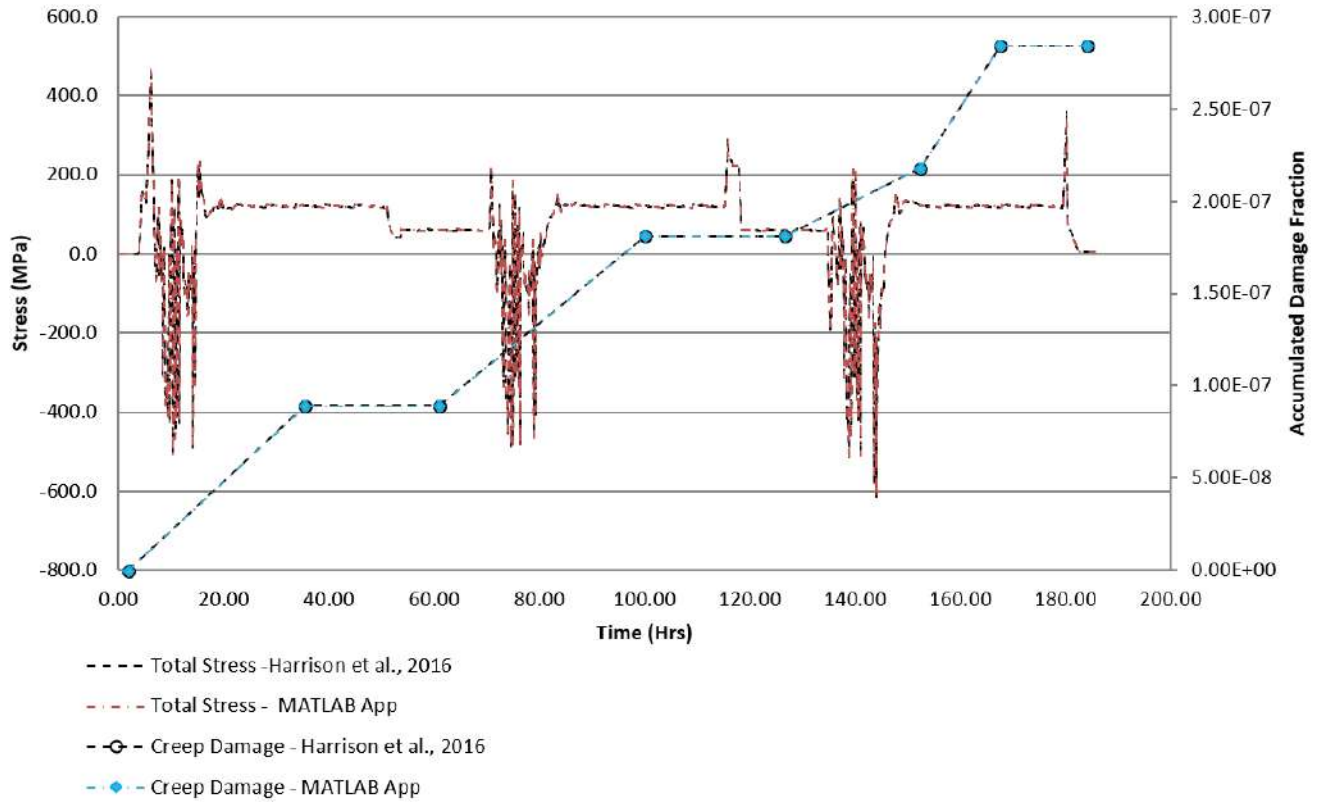
Figure 5.7: Comparing the calculation for total stress and creep damage done in Harrison et al. (2016) with the calculation done using the MATLAB app.

Finally, a comparison between the calculation using the MATLAB app and the work done by Harrison et al. (2016) is presented in Figure 5.7. The results by the MATLAB app show the same results as in Harrison et al. (2016).

5.4 Conclusion

In this chapter, a MATLAB app has been developed to study the creep damage for pipes at power plants under steam pressure and high temperatures. This tool serves as a life prediction tool considering creep damage only.

The importance of this tool is that:

a) This tool is user-friendly; it contains a simple GUI and documentation section, which describes all the sections of the app.

b) The code can be easily modified to include further calculations such as fatigue damage, as in Harrison et al. (2016), or to combine it with the FE tool for stress calculations.

c) The operation data of steam which passes through any steel Grade 91 pipe could be used and an analysis could be performed easily and quickly on different pipes of the power plant. If the pipes are of different materials and geometry, the materials and geometry constants should be obtained for each pipe.

d) Although using MATLAB could present a drawback as it is not an open-source programming tool, it could easily be used to deal with large operation data, which is a large data set collected over the operation years.

Chapter 6: Conclusions and Future Work

6.1 Conclusion

In this thesis three topics have been examined: the design and optimization of a shear specimen for high shear strain, the multiscale deformation modelling of steel P91 under high shear strain and a life prediction tool based on creep damage for steel P91.

The ASTM B831-05 design has been optimized to fulfil experimental criteria such as: optimizing the gauge width and the radius of circular notches to achieve local and uniform shear strain at the gauge region and having dimensions to fit the experimental setup. As a result, the dimensions of the ASTM B831-05 model have been modified to (50.00 mm x 25.00 mm x 6.00 mm), and the length between notches has been modified to 3.00 mm. These changes have been tested on P91 and X100 steels and have been shown to satisfy the design criteria as having uniform shear strain at the notch region at high shear strain, eliminating the out-of-plane deformation, and ensuring the suitability of the designed specimen dimensions for the experimental setup. This specimen has been manufactured and tested. The surface strain measurements using the DIC have shown that a uniform high shear strain has been developed at the notch region. Also, due to minimizing the out-of-plane deformation, good EBSD scans for the gauge region at high shear strain have been achieved at a high indexing rate (approximately 89%). These prove the suitability of the developed specimen for performing multiscale studies for P91 at high shear strain.

The designed specimen has been used to validate experimentally the computational model, where a multiscale crystal plasticity-based finite element model has been used to simulate P91 deformation at high shear strain. The experimental validation has been done using multiple scales under large shear deformations, an extensometer is used to measure the global elongation (cm-scale), digital image correlation (DIC) is used to measure shear strains close to the notch (mm-scale) and electron backscatter diffraction (EBSD) is used to measure the deformation-induced crystal reorientation in the uniform strain region (µm-scale). While qualitatively good agreement between the model and experiment has been obtained, the simulation results for crystal reorientation have shown differences between the experiment and the model. The reasons for the observed differences, which, as discussed, may be related to the variation of orientation through the thickness of the specimen should be examined in future work.

Finally, a MATLAB app has been developed to study the creep damage for pipes at power plants which face tough conditions of steam pressure and temperature. This tool serves as a life prediction tool, as the creep damage represents the main reason for the failure of welded Grade 91 steel, which

also has been developed for supercritical power plant operation conditions, and it is developed to have high creep resistance. This tool is user-friendly as it has a GUI, is open and can be easily modified to include fatigue or other failure models, also it can be applied to different materials as the power plant operation conditions can be constant over several pipes, and finally, it could analyse large data and use the Machine Learning (ML) package in MATLAB for advanced failure assessment.

6.2 Future Work

The multiscale modelling and the life prediction of P91 could be improved in several ways:

- A detailed study could be performed to study 3D effects on the crystals' reorientation at high shear strain. Several methodologies could be examined to achieve this study. For example, a layer beneath the surface could be assumed to have randomly oriented grains. Also, this layer could be constructed based on statistical data of crystal orientation for this material at the study conditions. Several EBSD scans could be done on different regions of the surface to construct data sets of the sizes and textures of the crystals. Furthermore, destructive testing could be performed through the thickness of the specimen to determine the 3D morphology, which is to be included in the FE model.

- In this study, only {110} <111> slip systems are used. However, the P91 has other slip systems: the 12 {112} <111> slip systems, and the 24 {123} <111> slip systems.

- Integrating the effect of possible changes in the precipitate (as $M_{23}C_6$ carbides) size diameter due to coarsening, during the deformation process, in the FE model may improve the predictability of this model.

- The MATLAB app developed in Chapter 5 can be used to predict the component lifetime. To achieve this goal, several modifications need to be applied. For instance, the effect of cyclic loading (fatigue) could be integrated into this app. Integrating residual stress into this app could also represent a significant improvement. For example, in Yaghi et al. (2005), the residual stresses for welded P91 have been calculated for a wide range of pipe dimensions, these results could be fitted to suitable mathematical formulas. These formulas could be integrated into the app, where the design dimensions represent the input and design-based residual stresses will be evaluated.

Appendix A: Plotting a Crystal Oriented in Direction $[\bar{1}11]$

In this Appendix a crystal oriented in direction $[\bar{1}11]$ with perpendicular in direction $[101]$ is examined. The analysis is done in three steps, as shown in the flowchart Figure A.0.1. First, calculate the third perpendicular vector using cross-product, then calculate the rotation matrix, and finally calculate the three Euler angles. Thus, in this Appendix, a description of the method to calculate the Euler angles based on two given vectors, which represent the orientation of the crystal, has been shown.
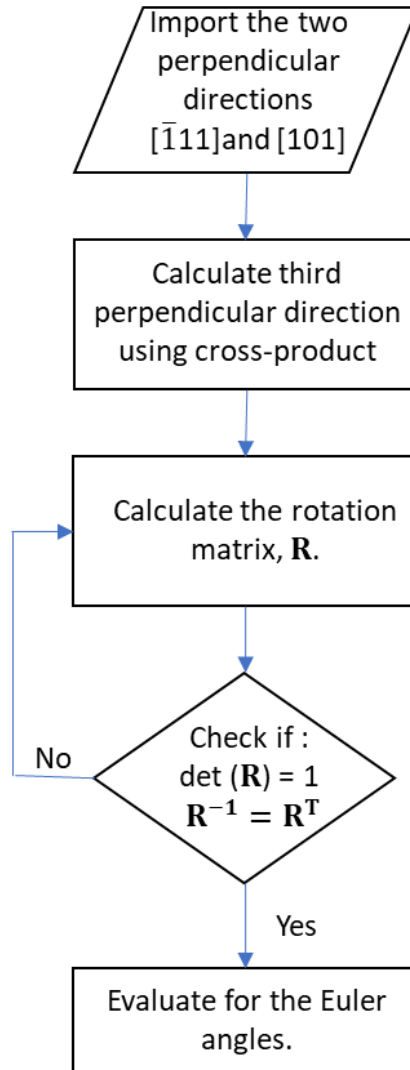
Figure A.0.1: The steps to calculate the Euler angles required for plotting the crystal orientation are based on two perpendicular vectors.

First Step:

$$x_1' = [\bar{1}11]$$
$$x_2' = [101]$$
$$x_3' = \begin{vmatrix} i & j & k \\ -1 & 1 & 1 \\ 1 & 0 & 1 \end{vmatrix} = \begin{vmatrix} 1 & 1 \\ 0 & 1 \end{vmatrix} i - \begin{vmatrix} -1 & 1 \\ 1 & 1 \end{vmatrix} j + \begin{vmatrix} -1 & 1 \\ 1 & 0 \end{vmatrix} k = [12\bar{1}]$$

These vectors should be normalized to give unit vectors,

$$x_1' = \frac{1}{\sqrt{3}}[\bar{1}11]$$

$$x_2' = \frac{1}{\sqrt{2}}[101]$$

$$x_3' = \frac{1}{\sqrt{6}}[12\bar{1}]$$

Second Step:

As the plotting of crystal orientation in a specific direction requires a reference state, thus, a crystal projected in [100] and perpendicular direction in [010] is selected as the reference. This is just the same as the cartesian coordinate system [100], [010], and [001].

$$\begin{bmatrix} -\dfrac{1}{\sqrt{3}} & \dfrac{1}{\sqrt{2}} & \dfrac{1}{\sqrt{6}} \\ \dfrac{1}{\sqrt{3}} & 0 & \dfrac{2}{\sqrt{6}} \\ \dfrac{1}{\sqrt{3}} & \dfrac{1}{\sqrt{2}} & \dfrac{-1}{\sqrt{6}} \end{bmatrix} = [R] \cdot \begin{bmatrix} 1 & 0 & 0 \\ 0 & 1 & 0 \\ 0 & 0 & 1 \end{bmatrix}$$

$$\mathbf{R} = \begin{bmatrix} -\dfrac{1}{\sqrt{3}} & \dfrac{1}{\sqrt{2}} & \dfrac{1}{\sqrt{6}} \\ \dfrac{1}{\sqrt{3}} & 0 & \dfrac{2}{\sqrt{6}} \\ \dfrac{1}{\sqrt{3}} & \dfrac{1}{\sqrt{2}} & \dfrac{-1}{\sqrt{6}} \end{bmatrix}$$

This **R** should have two properties: the det (**R**) = 1, $\mathbf{R}^{-1} = \mathbf{R}^T$. For checking both properties,

If $\mathbf{R}^T = \mathbf{R}^{-1}$, thus $\mathbf{R}^T\mathbf{R} = \mathbf{I}$

$$\mathbf{R}^T\mathbf{R} = \begin{bmatrix} -\dfrac{1}{\sqrt{3}} & \dfrac{1}{\sqrt{3}} & \dfrac{1}{\sqrt{3}} \\ \dfrac{1}{\sqrt{2}} & 0 & \dfrac{1}{\sqrt{2}} \\ \dfrac{1}{\sqrt{6}} & \dfrac{2}{\sqrt{6}} & \dfrac{-1}{\sqrt{6}} \end{bmatrix} \cdot \begin{bmatrix} -\dfrac{1}{\sqrt{3}} & \dfrac{1}{\sqrt{2}} & \dfrac{1}{\sqrt{6}} \\ \dfrac{1}{\sqrt{3}} & 0 & \dfrac{2}{\sqrt{6}} \\ \dfrac{1}{\sqrt{3}} & \dfrac{1}{\sqrt{2}} & \dfrac{-1}{\sqrt{6}} \end{bmatrix} = \begin{bmatrix} 1 & 0 & 0 \\ 0 & 1 & 0 \\ 0 & 0 & 1 \end{bmatrix}$$

Also, det (**R**)=1

71

Third Step:

Using Equation 4.22 to calculate the Euler angles $\varphi_1, \phi, \varphi_2$,

R =

$$\begin{bmatrix} \cos\varphi_1 \cos\varphi_2 - \cos\phi \sin\varphi_1 \sin\varphi_2 & -\cos\varphi_1 \sin\varphi_2 - \cos\phi \cos\varphi_2 \sin\varphi_1 & \sin\varphi_1 \sin\phi \\ \cos\varphi_2 \sin\varphi_1 + \cos\varphi_1 \cos\phi \sin\varphi_2 & \cos\varphi_1 \cos\phi \cos\varphi_2 - \sin\varphi_1 \sin\varphi_2 & -\cos\varphi_1 \sin\phi \\ \sin\phi \sin\varphi_2 & \cos\varphi_2 \sin\phi & \cos\phi \end{bmatrix} \quad \text{A.1}$$

$$\mathbf{R} = \begin{bmatrix} -\dfrac{1}{\sqrt{3}} & \dfrac{1}{\sqrt{2}} & \dfrac{1}{\sqrt{6}} \\ \dfrac{1}{\sqrt{3}} & 0 & \dfrac{2}{\sqrt{6}} \\ \dfrac{1}{\sqrt{3}} & \dfrac{1}{\sqrt{2}} & \dfrac{-1}{\sqrt{6}} \end{bmatrix}$$

To solve for the Euler angles $\varphi_1, \phi, \varphi_2$, the angle ϕ is calculated first, as $\cos(\phi) = \frac{-1}{\sqrt{6}}$, and the (ϕ) range is between $[0,180]$, $\phi = 114.1^{\circ}$. Then for φ_1, (R_{13}, R_{23}) will be used, thus φ_1 is in the second quadrant, it is equal to 153.4°. Then for φ_2, (R_{31}, R_{32}) will be used, thus φ_2 is in the first quadrant, it is equal to 39.23°.

As a check for correct calculation of the matrix **R** based on these Euler angles [153.43,114.1,39.23] using Equation A.1,

$$\mathbf{R}(153.43, 114.1, 39.23) = \begin{bmatrix} -0.5773 & 0.7071 & 0.4082 \\ 0.5774 & 0.0001 & 0.8165 \\ 0.5773 & 0.7071 & -0.4083 \end{bmatrix}$$

Thus, the angles have been correctly calculated. In this example, the set of Euler angles is unique; in other situations, several sets of Euler angles may lead to the same rotation matrix.

The orientation of the crystal projected in the [100] direction with perpendicular direction is [010] as shown in Figure A.0.2, this is presented as an initial orientation as a reference orientation. The plotting for it is shown on the inverse pole figure plot in Figure A.0.3.

The crystal projected in [$\bar{1}11$] direction and the perpendicular direction is [101] is plotted in Figure A.0.4, and the plotting for it is shown on inverse pole figure plot in Figure A.0.5. In this context, the results shown in Figure A.0.5 are very close to the FE and experimental results shown in Figure 4.30, and Figure 4.31.

Figure A.0.2: The crystal is projected in [100] and the perpendicular direction is [010].

Figure A.0.3: The inverse pole figure plot for a crystal projected in [100] and the perpendicular direction is [010]. This is plotted using MTEX.
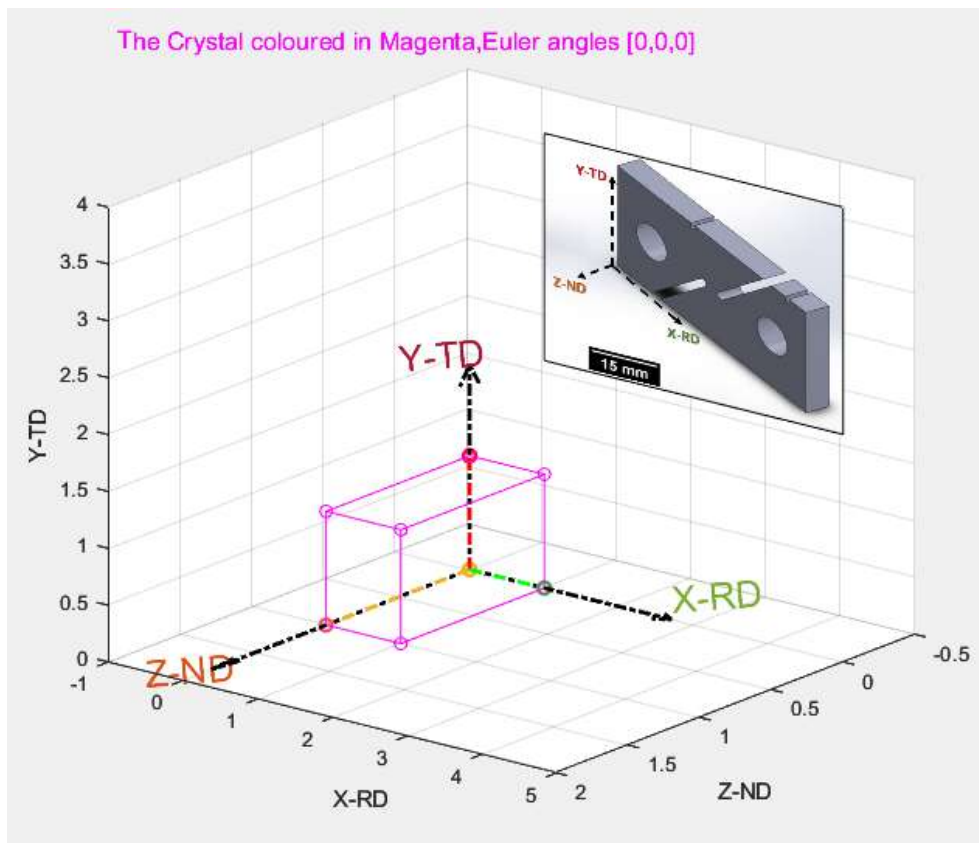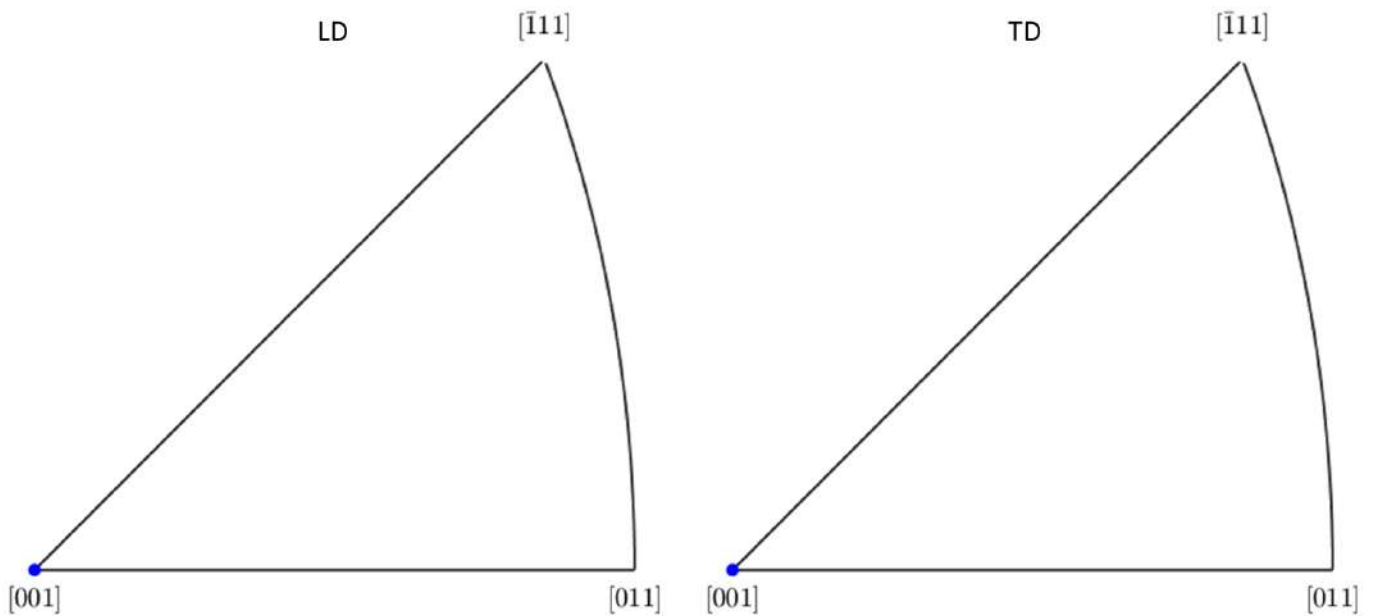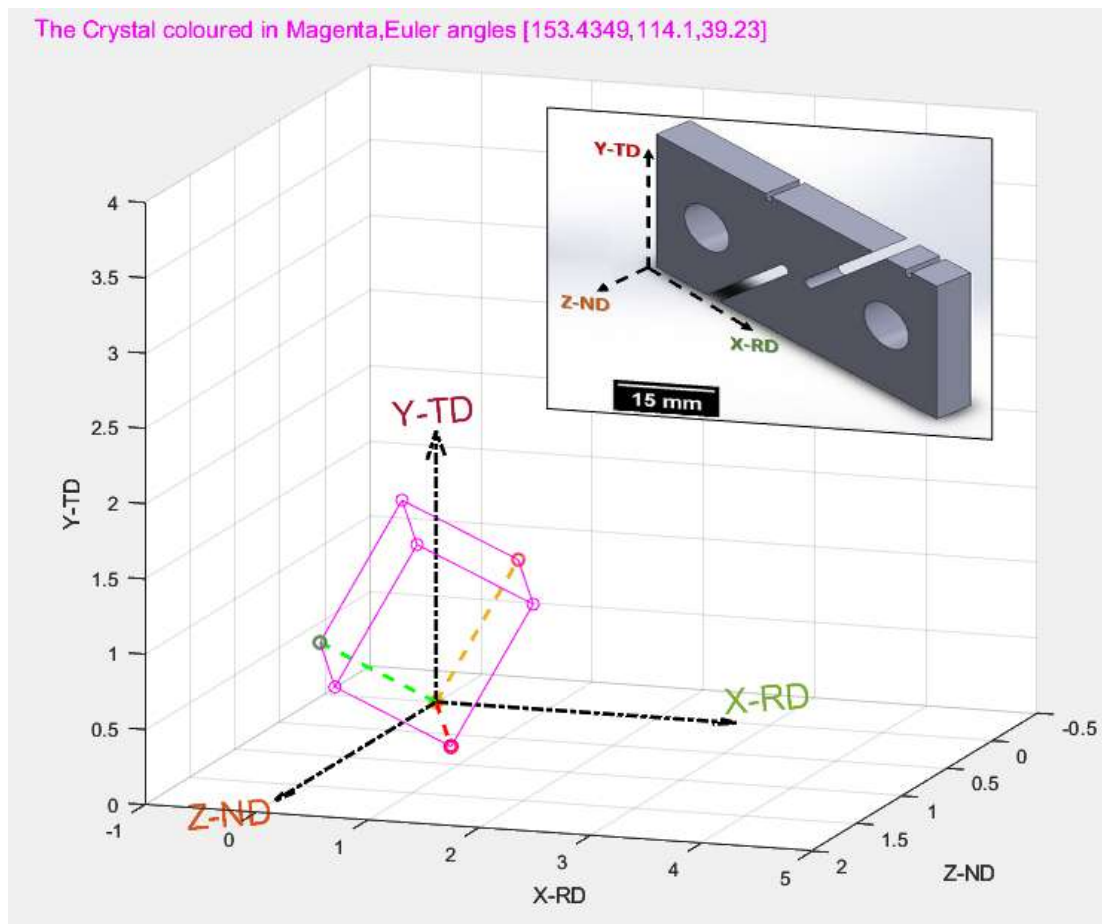
Figure A.0.4: The crystal projected in [$\bar{1}11$] and the perpendicular direction is [101].
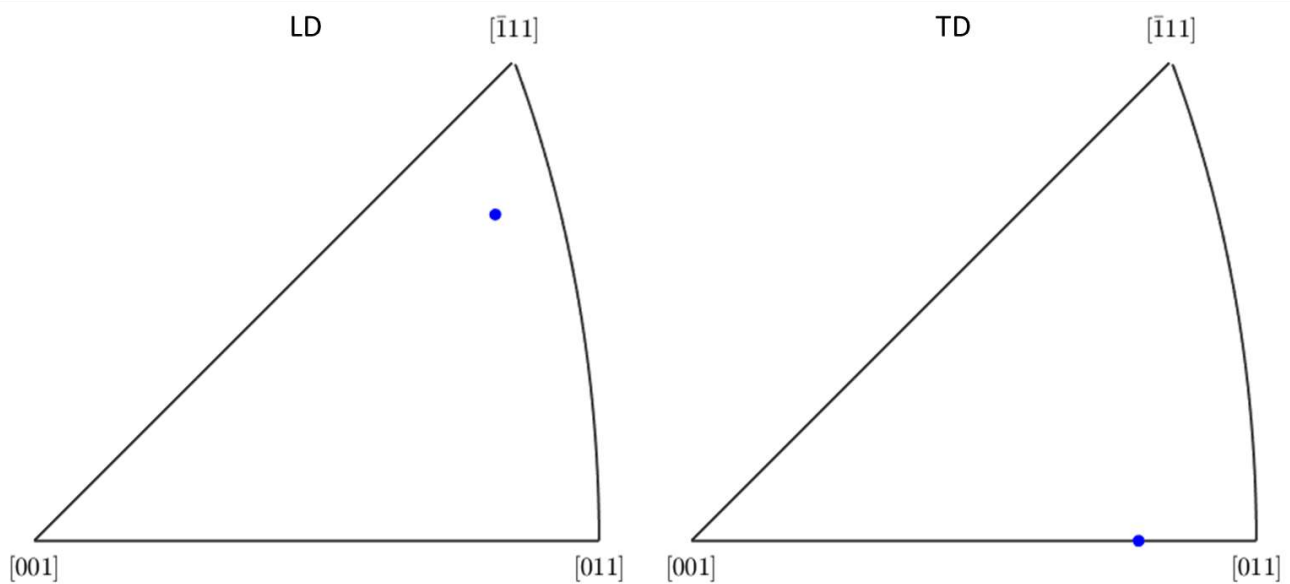

Figure A.0.5: The inverse pole figure plot for a crystal projected in [$\bar{1}11$] and the perpendicular direction is [101]. This is plotted using MTEX.

References

Abe, F. (2014). Grade 91 heat-resistant martensitic steel. In *Coal Power Plant Materials and Life Assessment: Developments and Applications* (Vol. 91). Woodhead Publishing Limited. https://doi.org/10.1533/9780857097323.1.3

Abson, D. J., & Rothwell, J. S. (2013). Review of type IV cracking of weldments in 9- 12%Cr creep strength enhanced ferritic steels. *International Materials Reviews*, *58*(8), 437–473. https://doi.org/10.1179/1743280412Y.0000000016

Adams, D. F., & Walrath, D. E. (1987). Further development of the losipescu shear test method. *Experimental Mechanics*, *27*(2), 113–119. https://doi.org/10.1007/BF02319461

Adams, D. O., Moriarty, J. M., Gallegos, A. M., & Adams, D. F. (2007). The V-Notched Rail Shear Test. *Journal of Composite Materials*, *41*(3), 281–297. https://doi.org/10.1177/0021998306063369

Asaro, R. J. (1983). Crystal Plasticity. *Journal of Applied Mechanics*, *50*(4b), 921–934. https://doi.org/10.1115/1.3167205

Asaro, R. J., & Rice, J. R. (1977). Strain localization in ductile single crystals. *Journal of the Mechanics and Physics of Solids*, *25*(5), 309–338. https://doi.org/10.1016/0022-5096(77)90001-1

ASTM B831–05. (2005). Standard Test Method for Shear Testing of Aluminum Alloys. *ASTM Standards*, *94*(Reapproved 2016), 1–4. https://doi.org/10.1520/B0831-05.2

Bachmann, F., Hielscher, R., & Schaeben, H. (2010). Texture Analysis with MTEX – Free and Open Source Software Toolbox. *Solid State Phenomena*, *160*, 63–68. https://doi.org/10.4028/WWW.SCIENTIFIC.NET/SSP.160.63

Bao, Y., & Wierzbicki, T. (2004). On fracture locus in the equivalent strain and stress triaxiality space. *International Journal of Mechanical Sciences*, *46*(1), 81–98. https://doi.org/10.1016/j.ijmecsci.2004.02.006

Batista Abreu, J. C., Vieira, L. M. C., Abu-Hamd, M. H., & Schafer, B. W. (2014). Review: development of performance-based fire design for cold-formed steel. *Fire Science Reviews*, *3*(1), 1–15. https://doi.org/10.1186/s40038-014-0001-3

Belytschko, T., Kam, W. K., Moran, B., & Elkhodary, K. I. (2014). Nonlinear Finite Elements for Continua and Structures, 2nd Edition. *Nonlinear Finite Elements For Continua and Structures*, 535–596. https://www.wiley.com/en-

ie/Nonlinear+Finite+Elements+for+Continua+and+Structures%2C+2nd+Edition-p-9781118632703

Busso, E. P. (1990). *Cyclic deformation of monocrystalline nickel aluminide and high temperature coatings* [Massachusetts Institute of Technology]. http://hdl.handle.net/1721.1/13973

Busso, E. P., Meissonnier, F. T., & O'Dowd, N. P. (2000). Gradient-dependent deformation of two-phase single crystals. *Journal of the Mechanics and Physics of Solids*, *48*(11), 2333–2361. https://doi.org/10.1016/S0022-5096(00)00006-5

Cabet, C., Dalle, F., Gaganidze, E., Henry, J., & Tanigawa, H. (2019). Ferritic-martensitic steels for fission and fusion applications. *Journal of Nuclear Materials*, *523*, 510–537. https://doi.org/10.1016/j.jnucmat.2019.05.058

Cano, J. A., & Stewart, C. M. (2021). A continuum damage mechanics (CDM) based Wilshire model for creep deformation, damage, and rupture prediction. *Materials Science and Engineering: A*, *799*(September 2020), 140231. https://doi.org/10.1016/j.msea.2020.140231

Chen, P., Ghassemi-Armaki, H., Kumar, S., Bower, A., Bhat, S., & Sadagopan, S. (2014). Microscale-calibrated modeling of the deformation response of dual-phase steels. *Acta Materialia*, *65*, 133–149. https://doi.org/10.1016/j.actamat.2013.11.036

Cheng, C. Der, Chen, P. Y., Tu, C. S., Chen, C. S., Feng, K. C., Yu, H. Y., Lee, Y. T., Chien, R. R., & Anthoniappen, J. (2020). Phase transformation and mechanism on enhanced creep-life in P9 Cr–Mo heat-resistant steel. *Journal of Materials Research and Technology*, *9*(3), 4617–4630. https://doi.org/10.1016/j.jmrt.2020.02.089

Dadras, P., & McDowell, J. S. (1990). Analytical and experimental evaluation of double-notch shear specimens of orthotropic materials. *Experimental Mechanics*, *30*(2), 184–189. https://doi.org/10.1007/BF02410246

Das, C. R., Albert, S. K., Bhaduri, A. K., Srinivasan, G., & Murty, B. S. (2008). Effect of prior microstructure on microstructure and mechanical properties of modified 9Cr-1Mo steel weld joints. *Materials Science and Engineering A*, *477*(1–2), 185–192. https://doi.org/10.1016/j.msea.2007.05.017

Dieter, G. E. (1988). *Mechanical Metallurgy*. McGraw-Hill.

Dudko, V., Belyakov, A., Molodov, D., & Kaibyshev, R. (2013). Microstructure evolution and pinning of boundaries by precipitates in a 9 pct Cr heat resistant steel during creep. *Metallurgical and Materials Transactions A: Physical Metallurgy and Materials Science*, *44*(SUPPL. 1).

https://doi.org/10.1007/s11661-011-0899-1

Dunne, F. P. E., Kiwanuka, R., & Wilkinson, A. J. (2012). Crystal plasticity analysis of micro-deformation, lattice rotation and geometrically necessary dislocation density. *Proceedings of the Royal Society A: Mathematical, Physical and Engineering Sciences*, *468*(2145), 2509–2531. https://doi.org/10.1098/rspa.2012.0050

Dunne, F. P. E., Rugg, D., & Walker, A. (2007). Lengthscale-dependent, elastically anisotropic, physically-based hcp crystal plasticity: Application to cold-dwell fatigue in Ti alloys. *International Journal of Plasticity*, *23*(6), 1061–1083. https://doi.org/10.1016/j.ijplas.2006.10.013

Ehlers, J., Young, D. J., Smaardijk, E. J., Tyagi, A. K., Penkalla, H. J., Singheiser, L., & Quadakkers, W. J. (2006). Enhanced oxidation of the 9%Cr steel P91 in water vapour containing environments. *Corrosion Science*, *48*(11), 3428–3454. https://doi.org/10.1016/j.corsci.2006.02.002

El-Hajjar, R., & Haj-Ali, R. (2004). In-plane shear testing of thick-section pultruded FRP composites using a modified Arcan fixture. *Composites Part B: Engineering*, *35*(5), 421–428. https://doi.org/10.1016/j.compositesb.2003.12.004

EN 12952-1. (2001). *Water-tube boilers and auxiliary installations- Part 1: General*. European Committee For Standardization.

EN 12952-4. (2011). *Water-tube boilers and auxiliary installations - Part 4: In-service boiler life expectancy calculations*. European Committee For Standardization.

Engler, O., & Randle, V. (2009). Introduction to Texture Analysis. In *Handbook of Texture Analysis*. CRC Press. https://doi.org/10.1201/9781420063660

Gao, F., Gui, L., & Fan, Z. (2011). Experimental and Numerical Analysis of an In-Plane Shear Specimen Designed for Ductile Fracture Studies. *Experimental Mechanics*, *51*(6), 891–901. https://doi.org/10.1007/s11340-010-9385-8

Gardner, K. A. (2013). *Experimental Techniques for Shear Testing of Thin Sheet Metals and Compression Testing at Intermediate Strain Rates*. Undefined. file:///paper/Experimental-Techniques-for-Shear-Testing-of-Thin-Gardner/f73b9e4aaefa9c27d2ce1bab41f727566bd91d8f

Golden, B. J., Li, D. F., Guo, Y., Tiernan, P., Leen, S. B., & O'Dowd, N. P. (2016). Microscale deformation of a tempered martensite ferritic steel: Modelling and experimental study of grain and sub-grain interactions. *Journal of the Mechanics and Physics of Solids*, *86*, 42–52.

https://doi.org/10.1016/j.jmps.2015.09.015

Gordon, C. M. (2007). *The Square Root Function of a Matrix*.

H.-J. Bunge. (1982). *Texture Analysis in Materials Science*. Elsevier. https://doi.org/10.1016/C2013-0-11769-2

Hald, J. (2017). High-alloyed martensitic steel grades for boilers in ultra-supercritical power plants. In *Materials for Ultra-Supercritical and Advanced Ultra-Supercritical Power Plants*. Elsevier Ltd. https://doi.org/10.1016/B978-0-08-100552-1.00003-8

Harrison, N. M., Adams, A., O'Donoghue, P. E., & Leen, S. B. (2016a). A combined creep and fatigue damage estimation tool for power-plant monitoring. *American Society of Mechanical Engineers, Pressure Vessels and Piping Division (Publication) PVP*, *6B*-*2016*, 1–7. https://doi.org/10.1115/PVP2016-63513

Harrison, N. M., Adams, A., O'Donoghue, P. E., & Leen, S. B. (2016b). A combined creep and fatigue damage estimation tool for power-plant monitoring. In *American Society of Mechanical Engineers, Pressure Vessels and Piping Division (Publication) PVP* (Vols. 6B-2016). https://doi.org/10.1115/PVP2016-63513

Hughes, D. A., & Hansen, N. (1997). High angle boundaries formed by grain subdivision mechanisms. *Acta Materialia*, *45*(9), 3871–3886. https://doi.org/10.1016/S1359-6454(97)00027-X

Hußnätter, W., & Merklein, M. (2008). Characterization of material behavior under pure shear condition. *International Journal of Material Forming*, *1*(S1), 233–236. https://doi.org/10.1007/s12289-008-0359-7

Klueh, R. L. (2004). *Elevated-temperature ferritic and martensitic steels and their application to future nuclear reactors, Oakridge National Laboratory //ORNL/TM-2004/176. November*.

LaVision. (2013). Davis 8.1 Software. *Product Manual 1003001*.

Li, D.-F. (2016). Micromechanical finite element modelling of thermo-mechanical fatigue for P91 steels. *International Journal of Fatigue*, 11.

Li, D.-F., Barrett, R. A., O'Donoghue, P. E., O'Dowd, N. P., & Leen, S. B. (2017). A multi-scale crystal plasticity model for cyclic plasticity and low-cycle fatigue in a precipitate-strengthened steel at elevated temperature. *Journal of the Mechanics and Physics of Solids*, *101*, 44–62. https://doi.org/10.1016/j.jmps.2016.12.010

Li, D. F., Barrett, R. A., O'Donoghue, P. E., Hyde, C. J., O'Dowd, N. P., & Leen, S. B. (2016). Micromechanical finite element modelling of thermo-mechanical fatigue for P91 steels. *International Journal of Fatigue*, *87*, 192–202. https://doi.org/10.1016/j.ijfatigue.2015.11.025

Li, D. F., Barrett, R. A., O'Donoghue, P. E., O'Dowd, N. P., & Leen, S. B. (2017). A multi-scale crystal plasticity model for cyclic plasticity and low-cycle fatigue in a precipitate-strengthened steel at elevated temperature. *Journal of the Mechanics and Physics of Solids*, *101*, 44–62. https://doi.org/10.1016/j.jmps.2016.12.010

Li, D. F., Golden, B. J., & O'Dowd, N. P. (2014). Multiscale modelling of mechanical response in a martensitic steel: A micromechanical and length-scale-dependent framework for precipitate hardening. *Acta Materialia*, *80*, 445–456. https://doi.org/10.1016/j.actamat.2014.08.012

Li, M., Sun, F., Li, D. F., O'Donoghue, P. E., Leen, S. B., & O'Dowd, N. P. (2018). The effect of ferrite phases on the micromechanical response and crack initiation in the intercritical heat-affected zone of a welded 9Cr martensitic steel. *Fatigue & Fracture of Engineering Materials & Structures*, *41*(6), 1245–1259. https://doi.org/10.1111/ffe.12768

Liu, J. Y. (2000). Shear test fixture design for orthotropic materials. *Seventh International Conference on Composites Engineering, July 2-8, 2000, Denver, Colorado. [New Orleans? : International Community for Composites Engineering? ; University of New Orleans, College of Engineering?, 2000].:P. 553-554 : Ill.* https://www.fs.usda.gov/research/treesearch/5838

Liu, J. Y., Ross, R. J., & Rammer, D. R. (1997). *Improved Arcan Shear Test for Wood*. 6.

Meade, E. D. (2020). Experimental Study & Multiscale Modelling of the High Temperature Deformation of P91 under Multiaxial Loading. In *Faculty of Science and Engineering: Vol. Philosophi* (Issue March). https://ulir.ul.ie/handle/10344/9303

Meade, E. D., O'Dowd, N., & Tiernan, P. (2020). Experimental Study & Multiscale Modelling of the High Temperature Deformation of P91 under Multiaxial Loading. *Faculty of Science and Engineering*, *Philosophi*(March), 256. https://ulir.ul.ie/handle/10344/9303

Meade, E. D., Sun, F., Tiernan, P., & O'Dowd, N. P. (2018a). Experimental study and multiscale modelling of the high temperature deformation of tempered martensite under multiaxial loading. *Materials Science and Engineering A, 737*(July), 383–392. https://doi.org/10.1016/j.msea.2018.09.040

Meade, E. D., Sun, F., Tiernan, P., & O'Dowd, N. P. (2018b). Experimental study and multiscale modelling of the high temperature deformation of tempered martensite under multiaxial loading. *Materials*

Science and Engineering: A, *737*, 383–392. https://doi.org/10.1016/j.msea.2018.09.040

Meade, E. D., Sun, F., Tiernan, P., & O'Dowd, N. P. (2021). A multiscale experimentally-based finite element model to predict microstructure and damage evolution in martensitic steels. *International Journal of Plasticity*, *139*(February), 102966. https://doi.org/10.1016/j.ijplas.2021.102966

Meissonnier, F. T., Busso, E. P., & O'Dowd, N. P. (2001). Finite element implementation of a generalised non-local rate-dependent crystallographic formulation for finite strains. *International Journal of Plasticity*, *17*(4), 601–640. https://doi.org/10.1016/S0749-6419(00)00064-4

Mroziński, S., Lis, Z., & Egner, H. (2022). Influence of Creep Damage on the Fatigue Life of P91 Steel. *Materials*, *15*(14). https://doi.org/10.3390/ma15144917

Office of Fossil Energy and Carbon Management. (2021). *Transformative Power Systems*. https://www.energy.gov/fecm/science-innovation/office-clean-coal-and-carbon-management/advanced-energy-systems/transformative#:~:text=The average coal-fired power,States operates near 33%25 efficiency.

Panait, C. G., Zielińska-Lipiec, A., Koziel, T., Czyrska-Filemonowicz, A., Gourgues-Lorenzon, A. F., & Bendick, W. (2010). Evolution of dislocation density, size of subgrains and MX-type precipitates in a P91 steel during creep and during thermal ageing at 600°C for more than 100,000h. *Materials Science and Engineering: A*, *527*(16–17), 4062–4069. https://doi.org/10.1016/j.msea.2010.03.010

Pardis, N., Ebrahimi, R., & Kim, H. S. (2017). Equivalent strain at large shear deformation: Theoretical, numerical and finite element analysis. *Journal of Applied Research and Technology*, *15*(5), 442–448. https://doi.org/10.1016/J.JART.2017.05.002

Peirs, J., Verleysen, P., & Degrieck, J. (2012a). Novel Technique for Static and Dynamic Shear Testing of Ti6Al4V Sheet. *Exp Mech*, 13.

Peirs, J., Verleysen, P., & Degrieck, J. (2012b). Novel Technique for Static and Dynamic Shear Testing of Ti6Al4V Sheet. *Experimental Mechanics*, *52*(7), 729–741. https://doi.org/10.1007/s11340-011-9541-9

Phan, T. Van. (2014). *Grain scale simulation of local deformation behavior*. 1–24.

Qadr, H. M., & Hamad, A. M. (2019). Mechanical Properties of Ferritic Martenstic Steels: A Review. *Scientific Bulletin of Valahia University - Materials and Mechanics*, *17*(16), 18–27. https://doi.org/10.2478/bsmm-2019-0003

R. J. Asaro. (1983). Crystal plasticity. *Crystals*, *11*(1), 1–3. https://doi.org/10.3390/cryst11010044

Reyes, A., & Eriksson, M. (2009). Assessment of yield and fracture criteria using shear and bending tests. *Materials and Design*, 13.

Rusinek, A., & Klepaczko, J. R. (2001). Shear testing of a sheet steel at wide range of strain rates and a constitutive relation with strain-rate and temperature dependence of the ¯ow stress. *International Journal of Plasticity*, 29.

Šeruga, D., Fajdiga, M., & Nagode, M. (2011). Creep damage calculation for thermo mechanical fatigue. *Strojniski Vestnik/Journal of Mechanical Engineering*, *57*(5), 371–378. https://doi.org/10.5545/sv-jme.2010.108

Shokrieh, M. M., & Lessard, L. B. (1998). An Assessment of the Double-Notch Shear Test for Interlaminar Shear Characterization of a Unidirectional Graphite/Epoxy under Static and Fatigue Loading. *Applied Composite Materials*, *5*(5), 289–304. https://doi.org/10.1023/A:1008816122371

Simulia. (2013). *Abaqus 6.11 Theory Manual*. 11.

Song, M., Sun, C., Chen, Y., Shang, Z., Li, J., Fan, Z., Hartwig, K. T., & Zhang, X. (2019). Grain refinement mechanisms and strength-hardness correlation of ultra-fine grained grade 91 steel processed by equal channel angular extrusion. *International Journal of Pressure Vessels and Piping*, *172*(February), 212–219. https://doi.org/10.1016/j.ijpvp.2019.03.025

St-Pierre, L., Héripré, E., Dexet, M., Crépin, J., Bertolino, G., & Bilger, N. (2008). 3D simulations of microstructure and comparison with experimental microstructure coming from O.I.M analysis. *International Journal of Plasticity*, *24*(9), 1516–1532. https://doi.org/10.1016/j.ijplas.2007.10.004

Stamopoulos, A., Di Genova, L. G., & Ilio, A. (2020). Assessment of the shear properties of thermoplastic composites using the ±45° tension and the V-notched rail shear methods. *Manufacturing Review*, *7*, 10. https://doi.org/10.1051/mfreview/2020007

Stojcevski, F., Hilditch, T., & Henderson, L. C. (2018). A modern account of Iosipescu testing. *Composites Part A: Applied Science and Manufacturing*, *107*, 545–554. https://doi.org/10.1016/j.compositesa.2018.02.011

Sun, F., Meade, E. D., & O'Dowd, N. P. (2019). Strain gradient crystal plasticity modelling of size effects in a hierarchical martensitic steel using the Voronoi tessellation method. *International Journal of Plasticity*, *119*, 215–229. https://doi.org/10.1016/j.ijplas.2019.03.009

Sundararajan, G. (1989). The Monkman-Grant Relationship. *Materials Science and Engineering A*, *Volume 112*, 205–214. https://doi.org/https://doi.org/10.1016/0921-5093(89)90360-2

Tabuchi, M., & Takahashi, Y. (2012a). Evaluation of creep strength reduction factors for welded joints of modified 9Cr-1Mo steel. *Journal of Pressure Vessel Technology, Transactions of the ASME*, *134*(3), 1–6. https://doi.org/10.1115/1.4006131

Tabuchi, M., & Takahashi, Y. (2012b). Evaluation of creep strength reduction factors for welded joints of modified 9Cr-1Mo steel. *Journal of Pressure Vessel Technology, Transactions of the ASME*, *134*(3), 1–2. https://doi.org/10.1115/1.4006131

Taheri-Behrooz, F., & Moghaddam, H. S. (2018a). Nonlinear numerical analysis of the V-notched rail shear test specimen. *Polymer Testing*, *65*, 44–53. https://doi.org/10.1016/j.polymertesting.2017.11.008

Taheri-Behrooz, F., & Moghaddam, H. S. (2018b). Nonlinear numerical analysis of the V-notched rail shear test specimen. *Polymer Testing*, *65*, 44–53. https://doi.org/10.1016/j.polymertesting.2017.11.008

Tarigopula, V., Hopperstad, O. S., Langseth, M., Clausen, A. H., Hild, F., Lademo, O.-G., & Eriksson, M. (2008). A Study of Large Plastic Deformations in Dual Phase Steel Using Digital Image Correlation and FE Analysis. *Experimental Mechanics*, *48*(2), 181–196. https://doi.org/10.1007/s11340-007-9066-4

Tarnopol'skii, Y. M., & Kintsis, T. Y. (1981). Methods for testing composites in shear (review). *Mechanics of Composite Materials*, *17*(3), 364–376. https://doi.org/10.1007/BF00605081

Tekkaya, A. E., Pöhlandt, K., & Lange, K. (1982). Determining Stress-Strain Curves of Sheet Metal in the Plane Torsion Test. *CIRP Annals*, *31*(1), 171–174. https://doi.org/10.1016/S0007-8506(07)63291-0

Turner, C. H., & Burr, D. B. (1993). Basic biomechanical measurements of bone: A tutorial. *Bone*, *14*(4), 595–608. https://doi.org/10.1016/8756-3282(93)90081-K

Ud Din, I., Hao, P., Panier, S., Khan, K. A., Aamir, M., Franz, G., & Akhtar, K. (2020a). Design of a New Arcan Fixture for In-plane Pure Shear and Combined Normal/Shear Stress Characterization of Fiber Reinforced Polymer Composites. *Experimental Techniques*, *44*(2), 231–240. https://doi.org/10.1007/s40799-019-00353-9

Ud Din, I., Hao, P., Panier, S., Khan, K. A., Aamir, M., Franz, G., & Akhtar, K. (2020b). Design of a New

Arcan Fixture for In-plane Pure Shear and Combined Normal/Shear Stress Characterization of Fiber Reinforced Polymer Composites. *Experimental Techniques*, *44*(2), 231–240. https://doi.org/10.1007/s40799-019-00353-9

Wang, K., Liu, X., Fan, P., Zhu, L., Zhang, K., Hou, W., & Wang, L. (2022). Creep behavior and life prediction of P91 heat-resistant steel using modified Wilshire model. *International Journal of Pressure Vessels and Piping*, *199*(October 2021), 104726. https://doi.org/10.1016/j.ijpvp.2022.104726

Yaghi, A. H., Hyde, T. H., Becker, A. A., Williams, J. A., & Sun, W. (2005). Residual stress simulation in welded sections of P91 pipes. *Journal of Materials Processing Technology*, *167*(2–3), 480–487. https://doi.org/10.1016/j.jmatprotec.2005.05.036

Yin, Q., Soyarslan, C., Güner, A., Brosius, A., & Tekkaya, A. E. (2012). A cyclic twin bridge shear test for the identification of kinematic hardening parameters. *International Journal of Mechanical Sciences*, *59*(1), 31–43. https://doi.org/10.1016/j.ijmecsci.2012.02.008

Yin, Q., Soyarslan, C., Isik, K., & Tekkaya, A. E. (2015). A grooved in-plane torsion test for the investigation of shear fracture in sheet materials. *International Journal of Solids and Structures*, *66*, 121–132. https://doi.org/10.1016/j.ijsolstr.2015.03.032

Yin, Q., Zillmann, B., Suttner, S., Gerstein, G., Biasutti, M., Tekkaya, A. E., Wagner, M. F.-X., Merklein, M., Schaper, M., Halle, T., & Brosius, A. (2014a). An experimental and numerical investigation of different shear test configurations for sheet metal characterization. *International Journal of Solids and Structures*, *51*(5), 1066–1074. https://doi.org/10.1016/j.ijsolstr.2013.12.006

Yin, Q., Zillmann, B., Suttner, S., Gerstein, G., Biasutti, M., Tekkaya, A. E., Wagner, M. F. X., Merklein, M., Schaper, M., Halle, T., & Brosius, A. (2014b). An experimental and numerical investigation of different shear test configurations for sheet metal characterization. *International Journal of Solids and Structures*, *51*(5), 1066–1074. https://doi.org/10.1016/j.ijsolstr.2013.12.006

Yoshihara, H., & Matsumoto, A. (2005). Measurement of the shearing properties of wood by in-plane shear test using a thin specimen. *Wood Science and Technology*, *39*(2), 141–152. https://doi.org/10.1007/s00226-004-0283-z

Zhang, T., Collins, D. M., Dunne, F. P. E., & Shollock, B. A. (2014). Crystal plasticity and high-resolution electron backscatter diffraction analysis of full-field polycrystal Ni superalloy strains and rotations under thermal loading. *Acta Materialia*, *80*, 25–38. https://doi.org/10.1016/j.actamat.2014.07.036

Zhang, W., Wang, X., Wang, Y., Yu, X., Gao, Y., & Feng, Z. (2020). Type IV failure in weldment of creep resistant ferritic alloys: I. Micromechanical origin of creep strain localization in the heat affected zone. *Journal of the Mechanics and Physics of Solids*, *134*. https://doi.org/10.1016/j.jmps.2019.103774

Zhang, Z., Lunt, D., Abdolvand, H., Wilkinson, A. J., Preuss, M., & Dunne, F. P. E. (2018). Quantitative investigation of micro slip and localization in polycrystalline materials under uniaxial tension. *International Journal of Plasticity*, *108*(April), 88–106. https://doi.org/10.1016/j.ijplas.2018.04.014

P. Rao, S. Isavand, A. Bondarev, 2023, Micropillar testing of P91, work in preparation.